DISTRIBUTION AND PHYSICAL PROPERTIES OF ARM AND INTERARM MOLECULAR CLOUDS IN THE OUTER GALAXY

By

Sean J. Carey

A Project Submitted to the Graduate
Faculty of Rensselaer Polytechnic Institute
in Partial Fulfillment of the
Requirements for the Degree of
DOCTOR OF PHILOSOPHY
Major Subject: Physics

Approved by the
Examining Committee:

Dr. Marc L. Kutner, Thesis Adviser

Dr. Wayne G. Roberge, Member

Dr. Toh-Ming Lu, Member

Dr. Nimai C. Mukhopadhyay, Member

Dr. Deborah A. Lawrence, Member

Rensselaer Polytechnic Institute
Troy, New York

May 1995
(For Graduation August 1995)

DISTRIBUTION AND PHYSICAL PROPERTIES OF ARM AND INTERARM MOLECULAR CLOUDS IN THE OUTER GALAXY

By

Sean J. Carey

An Abstract of a Thesis Submitted to the Graduate
Faculty of Rensselaer Polytechnic Institute
in Partial Fulfillment of the
Requirements for the Degree of
DOCTOR OF PHILOSOPHY
Major Subject: Physics

The original of the complete thesis is on file
in the Rensselaer Polytechnic Institute Library

Approved by the
Examining Committee:

Dr. Marc L. Kutner, Thesis Adviser

Dr. Wayne G. Roberge, Member

Dr. Toh-Ming Lu, Member

Nimai C.
Dr. Nimai C. Mukhopadhyay, Member

Deborah A. Law
Dr. Deborah A. Lawrence, Member

Rensselaer Polytechnic Institute
Troy, New York

May 1995
(For Graduation August 1995)

CONTENTS

LIST OF TABLES

LIST OF FIGURES

ACKNOWLEDGMENT

The work described in this thesis has been the better part of my existence for the last few (okay 6) years. In this endeavor, I have relied on the support, advice and wisdom of many people. I would like to most sincerely thank everyone mentioned below (hopefully, I didn't forget anyone).

I have been lucky to have two advisors on this project. Marc Kutner has been a good friend and mentor. He has given me limitless freedom in my research but has always provided excellent and timely advice. Marc, I hope that I attain your sense of the big picture some day. My other advisor, Kathryn Mead, has challenged me to defend my ideas intellectually. Thanks Kathy, for always being willing to listen to a crazy idea or my griping about the system. Many thanks to the other astrophysics faculty at RPI. C.M. Leung, Wayne Roberge and Doug Whittet have all had a hand in my career here. I know that I am a better scientist and person as a result of their instruction and counsel.

Many thanks to Donald Mizuno, for his fantastic data reduction system, REDUCE, the many fruitful scientific conversations we have had, and most importantly his friendship. Chris Cook and Mike Egan deserve special recognition for their friendship and motivational skills. Thanks Chris and Mike for helping me keep a good attitude and put things in perspective.

I had the extraordinary opportunity to work in a very special environment, the StarLab. I would like to thank the current and past inhabitants: Doug Caldwell, Jean Chiar, Steve Doty, Fred Gellert, Lida He, Dave Joiner, Andy Kalukin, Monika Kress, Dave Messinger, Mark Rawlings and Jeff Shykula for their support, wit and enthusiasm for the discipline. Thanks for all the discussions and the many pints shared.

On the scientific side, I must thank Jean Chiar for the multi-variate fitting

program, Don Mizuno for providing the beam convolution data, Doug Caldwell for enlightening conversations about mass estimates and the Magellanic Clouds and Seth Digel for a description of his mass determination method. The staff of the NRAO 12 meter telescope has provided excellent support during my observing runs for this project. I sincerely thank Andy Kalukin and Staycee Sciranka for their careful proofreading of this document. Without their help, this thesis would not be as readable as it is. Thanks to Kathryn Mead for permission to reproduce a figure from her thesis. I would like to thank my committee for their comments and careful consideration. Dr. Deborah Lawrence was especially helpful by providing a mathematican's perspective.

I thank the following organizations for their generous travel support: the National Radio Astronomical Observatory (NRAO) and the Astronomical Society of New York. I was also aided by a Grant-in-Aid of Research from the National Academy of Sciences, through Sigma Xi, The Scientific Research Society.

Without my parents, Ralph and Sandy, and my two brothers, Pat and Mugsy, this work would never have been completed. I can never thank them adequately for all they have done. A final acknowledgment to Staycee Sue Sciranka, who entered my life when I was at a crossroads. Thanks for helping me rediscover the 'joy of life' that I had lost for a while, without your support this page would have never been written.

ABSTRACT

Understanding the nature of the distribution of molecular material as a function of interstellar environment is an important step in understanding cloud formation and evolution. I have conducted an unbiased, high sensitivity, 60" sampled survey of the outer Galaxy in the ^{12}CO ($J = 1 \rightarrow 0$) transition. Two different cloud populations, arm and interarm, have been identified. The arm population coincides with the 13 kpc arm identified by Mead & Kutner (1988) and is dominated by massive clouds. The interarm population consists almost entirely of small clouds which are scattered throughout the survey volume. The small ($10^3 - 10^4 M_\odot$) clouds are more underluminous in CO than previously investigated clouds by a factor of four or more. The kinetic temperatures of the clouds are not a strong function of cloud environment and range between 5-12 K. The size-linewidth relationship is examined for this sample of clouds, and no correlation is found between cloud size and the observed linewidth of the ^{12}CO ($J = 1 \rightarrow 0$) transition.

A major implication of this measured cloud distribution is that a significant portion ($\sim 30\%$) of the molecular mass of the outer Galaxy is contained in small cold clouds. As small clouds in the outer Galaxy appear to be underluminous when compared to their larger inner Galaxy counterparts, virial mass estimates are preferred over estimating cloud masses using the empirical relationship between H_2 column density and the integrated intensity of the ^{12}CO ($J = 1 \rightarrow 0$) line. Estimates of the total molecular mass are interpreted using the observed small cloud distribution and inadequacy of the $N(H_2)$ to I_{CO} relationship to determine cloud masses for clouds in the outer Galaxy. Previous total mass estimates [Wouterloot *et al.* (1990) and Digel (1991)] of the outer Galaxy should be scaled upward by a factor 2-3. My best estimate of the total molecular mass of the outer Galaxy is between 1 and $2 \times 10^9 M_\odot$. Cold molecular material in the outer Galaxy is searched for, but not found.

CHAPTER 1
INTRODUCTION AND HISTORICAL REVIEW

People have pondered the nature of the Heavens ever since someone first looked at night time sky. In its most basic form, the science of astronomy has changed little from the goals of the first astronomers, who tried to explain what the spots of light they saw at night were. As time has passed and our understanding of the Universe has increased, we have been able to better define the question of what is in the sky, and more clearly explain why we see what we do. This work concentrates on a specific aspect, what is the distribution and physical properties of molecular clouds in the outer Galaxy, of the general question, what do we see when we look at the night sky?

Most of our information about the nature of the Universe has been obtained by observations of starlight. Stars comprise the majority of visible mass in the Universe, and are the source of metals (elements heavier than helium) through the process of nucleosynthesis. The importance of studying stars cannot be questioned. To further our understanding of stars, how they form and how they are distributed in the Galaxy, it is vitally important to study the birthplaces of stars, molecular clouds. By investigating the physical conditions of molecular clouds, information needed to explain the specifics of the star formation process can be obtained. Molecular clouds are composed primarily of molecular hydrogen with trace abundances of carbon monoxide (CO), carbon sulfide (CS) and other molecules. Molecular clouds span a wide range of sizes, masses and temperatures. A more detailed discussion is given in Section 2.6.

In addition, molecular clouds comprise a large fraction of the mass between the stars, which is called the interstellar medium (ISM). The study of the distribution of molecular clouds, as a function of the clouds' environment, will provide information useful in determining the formation and destruction mechanisms of the birthplaces of stars. A cloud's environment is characterized by many physical quantities. The most important are the external pressure of the medium surrounding the cloud, the ambient radiation field (usually called the interstellar radiation field or ISRF), the fraction of elements heavier than helium in the gas (also called the metallicity) and the gravitational potential that the cloud is in.

Molecular clouds were first identified by Barnard (1919) as patches of high optical extinction. Further optical identification of these dark clouds was done by many authors including Lynds (1962). The first identification of carbon monoxide in molecular clouds (the Orion nebula) was by Wilson *et al.* (1970). With the advent of good millimeter wave receivers, many investigations of molecular material (both Galactic and extragalactic) were conducted in the 1980's. The large scale surveys, of the Columbia [Cohen *et al.* (1980)] and UMASS-Stonybrook [Sanders *et al.* (1986)] groups, mapped the Galactic plane in the ^{12}CO ($J = 1 \rightarrow 0$) transition. In general, millimeter wave observations of rotational transitions by molecules are the preferred tracers of molecular clouds: as they unambiguously identify molecular material, foreground material does not obscure millimeter observations of clouds, and the distance to the cloud can be obtained by the Doppler shift of the line and some assumptions on how material moves around the center of the Galaxy. Distances calculated in this fashion are called kinematic distances and are discussed in Section 2.4.

The ^{12}CO ($J = 1 \rightarrow 0$) spectral line is the best tracer of molecular clouds, as CO is the second most abundant molecule in the interstellar medium (ISM) and is easily excited due to its low electric dipole moment. Details of the ^{12}CO ($J = 1 \rightarrow 0$) transition are given in Section 1.3. H_2, the most abundant molecule in the ISM, has no dipole rotational transitions, as it is a symmetric molecule and has no permanent electric dipole moment. Vibrational transitions of H_2 have been observed; however, these transitions are only observed in shock heated gas [Scoville & Sanders (1987)], which is uncommon in the ISM. Electronic transitions of H_2 have also been observed in absorption by molecular clouds in front of UV bright stars. Unfortunately, very few lines of sight through the ISM can be probed using this type of observation. In general, the physical properties of molecular clouds are determined by observing rotational transitions of trace molecules. Each transition is a sensitive probe of different ranges of cloud kinetic temperature and density. The range of physical conditions that can be probed with a particular transition depend on the details of the excitation of that particular spectral line.

In discussing the distribution of material in the Galaxy, astronomers often divide the Galaxy into two different regions, inner and outer. The inner Galaxy consists of that portion of the Galaxy which is closer to the center than the radius of the Sun's orbit about the center, $R_0 = 8.5$ kiloparsecs (kpc, 1 parsec is 3×10^{18} cm). The outer Galaxy is that part of the Galaxy at Galactocentric radii (R) greater than 8.5 kpc. The most useful coordinate system for describing the distribution of material in the Galaxy is Galactic longitude, l, and Galactic latitude, b. Figure 1.1 shows how Galactic longitude is measured. Galactic latitude is measured from the Galactic plane ($b = 0°$). The region observed in this work is centered on $l = 76.37°$, $b = 1.45°$, and covers Galactocentric radii between 9 and 16 kpc. As the survey region is on the other side of the Galaxy, corresponding optical and infrared studies of the region cannot be undertaken due to extinction by intervening material.

Most work on molecular clouds has concentrated on nearby clouds such as the Orion and Taurus molecular clouds or large scale surveys of inner Galaxy clouds. The Columbia and UMASS-Stonybrook surveys measured the properties of molecular clouds in the inner Galaxy and found that most of the molecular mass is contained in giant molecular clouds (GMCs) with masses of $10^5 - 10^6$ $M_\odot$ ($1M_\odot$ or solar mass

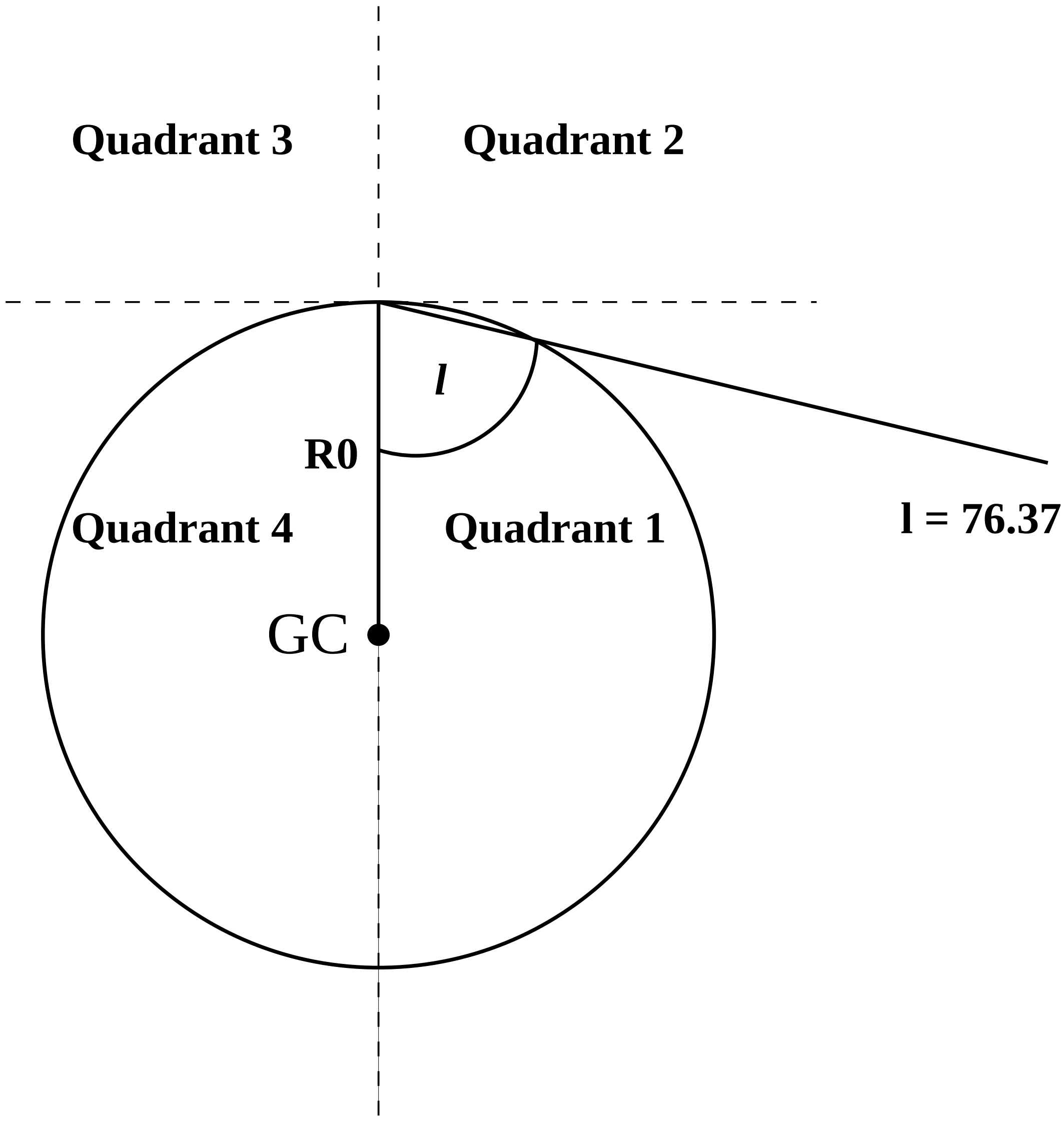

Figure 1.1: Schematic of location of survey region in Galactic plane. GC is the Galactic center. The Sun is located at the center of the dashed cross, and the line at $l = 76.37°$ is the line of sight observed.

is 2×10^{33} g) [*e.g.* Solomon & Sanders (1985)]. These clouds have kinetic temperatures around 10 K. In addition to GMCs, smaller clouds often called dark clouds or globules exist. They have masses between 5 and 300 $\mathrm{M}_\odot$ and temperatures similar to GMCs [Leung (1985)]. Interpreting inner Galaxy observations is difficult due to blending of emission features, and the distance ambiguity inherent in calculating distances to inner Galaxy clouds kinematically. In the inner Galaxy, the emission from molecular clouds tends to overlap making determinations of the properties of individual clouds difficult. The distance ambiguity is the result of clouds at two different heliocentric distances having the same velocity projection along the line of sight (v_{LSR}).

In the last ten years, the focus of molecular investigations has switched to the outer Galaxy. As there is no distance ambiguity for kinematic distances in the outer Galaxy and the number density of clouds is lower, assignment of individual cloud properties is more straightforward. However, the signals from outer Galaxy clouds are weaker due to somewhat lower cloud kinetic temperatures and beam dilution effects making the observations more difficult to conduct.

1.1 Historical Review of Molecular Studies of the Outer Galaxy

The first published maps of molecular clouds in the outer Galaxy were by Kutner & Mead (1981a) using the NRAO[1] 12 meter telescope. Their results were questioned by Solomon *et al.* (1983), who surveyed the same region of the outer Galaxy, but with a negative result. Further observations have validated the results of Mead and Kutner. The differences between the authors can be attributed to the sensitivity and resolution of the instruments used.

The work of Mead and Kutner continued with a larger survey of molecular clouds in the outer Galaxy. In a series of papers, Mead *et al.* (1987), Mead (1988),

---

[1] The National Radio Astronomy Observatory is operated by Associated Universities, Inc., under cooperative agreement with the National Science Foundation.

Mead *et al.* (1988) and Mead *et al.* (1990), the physical properties and star forming characteristics of molecular clouds in the outer Galaxy are measured. Summarizing some of their more important results: Outer Galaxy GMCs clouds have masses, ranging from 10^3 to 10^5 $M_\odot$, that are comparable to but slightly less than inner Galaxy GMC masses. The average kinetic temperature of outer Galaxy clouds is 7 K. In the first quadrant, there exists a strong molecular arm at R = 13 kpc. The ratio of the molecular hydrogen column density to integrated ^{12}CO ($J = 1 \rightarrow 0$) intensity (X factor) is a factor of two higher than the inner Galaxy X factor. On average, the star formation efficiency of outer Galaxy clouds is the same as the star formation efficiency of inner Galaxy clouds. In both regions, star formation efficiency is independent of cloud mass between 10^3 and 10^6 $M_\odot$. Their best estimate of the total molecular mass is 5×10^8 $M_\odot$ [Kutner & Mead (1981b)].

Instead of conducting a complete survey of a limited region of the sky as done by Mead's group, another group headed by J. Wouterloot used the IRAS (Infrared Astronomical Satellite) point source catalog to identify infrared objects associated with star formation. These objects were then observed in ^{12}CO ($J = 1 \rightarrow 0$) (as well as the ^{13}CO ($J = 1 \rightarrow 0$) and ^{12}CO ($J = 3 \rightarrow 2$) transitions) [Wouterloot & Brand (1989)]. In subsequent papers [Wouterloot *et al.* (1990), Wouterloot *et al.* (1993) and Brand & Wouterloot (1994)], they determine the following properties of the distribution of molecular material in the outer Galaxy. The distribution of molecular material follows the warp observed in the HI (atomic hydrogen) distribution, and the molecular distribution is flared with the scale height of the material increasing as a function of R. Their estimate of the total molecular mass of the outer Galaxy is 6×10^8 $M_\odot$. Recently, CO maps of some of the IRAS positions have been made; they find that the X factor for their sample of clouds is the same as the inner Galaxy value.

Another large scale survey for molecular material in the outer Galaxy was conducted by a group led by S. Digel using the Columbia (later CfA) 1 m telescope. The major results of this work [Digel *et al.* (1990), Digel (1991)] are : the X factor in the outer Galaxy is a factor of 4 higher than that used in the inner Galaxy, and their best estimate of the total molecular mass of the outer Galaxy is 6×10^8 $M_\odot$ [see Dame (1993)]. More recently, Digel *et al.* (1994) [also de Geus *et al.* (1993)] have observed 11 molecular clouds at large Galactocentric radii ranging from 18 to 28 kpc. These clouds have kinetic temperatures similar to other clouds in the outer Galaxy.

The three major molecular studies of outer Galaxy are biased towards large (or star-forming) clouds. Due to the large solid angle that the outer Galaxy fills, it is impractical at the current time to conduct a complete, well-sampled, sensitive survey, which would provide a truly unbiased measurement of the distribution of molecular material in the outer Galaxy. In the case of Mead's survey, the sample is biased towards large, bright clouds as they mapped individual clouds, instead of making a sensitive map of a particular region. Digel's survey used a large beam (8.7'); therefore, it is unlikely that small clouds would be detected, as the line temperatures would be significantly reduced by beam dilution. Lastly, the Wouterloot's survey is inherently biased towards star-forming clouds as they selected their sample using IRAS point sources which are probably young embedded objects.

Terebey *et al.* (1986) determined the size spectrum of outer Galaxy clouds using a sample set of 16 molecular clouds. Their results will be discussed in Section 4.2.1. Carpenter *et al.* (1993) determined the star formation properties of molecular clouds in the outer Galaxy. Their conclusions agree with the previous results of Mead *et al.* (1990). Leung & Thaddeus (1992) have recently conducted a survey in ^{12}CO ($J = 1 \rightarrow 0$) of the Cygnus X region. They find a wealth of emission in the ranges of galactic latitude and longitude covered but do not provide any interpretation of their observations.

Observations of molecular clouds and HII (ionized hydrogen) regions at large R have been used by Blitz and Brand [*e.g.* Blitz (1979) and Brand & Blitz (1993)] to determine the rotation curve of the outer Galaxy. As they are primarily interested in the rotation curve and not the physical properties of the molecular clouds, their work will not be discussed in this thesis.

Current and very provocative work has been done by Lequeux *et al.* (1993). They have observed ^{12}CO ($J = 1 \rightarrow 0$) in absorption along 2 lines of sight in the outer Galaxy containing strong millimeter wave continuum sources. Their results imply the presence of some cold molecular gas. The amount of cold molecular material in the outer Galaxy is currently unknown at this point; however, Lequeux *et al.* have suggested that cold molecular material may be a gravitationally significant component of the outer Galaxy; that is, cold molecular clouds may be a viable dark matter candidate. Subsequent interpretation by the authors [Lequeux (1995)] does not support this suggestion; however, cold molecular clouds as a dark matter candidate is an interesting possibility. This question of cold clouds as dark matter will be discussed in Chapter 5.

1.2 Spiral Structure of the Milky Way

The Milky Way is a spiral galaxy; however due to our vantage point (being inside the galaxy), we are not able to distinguish the spiral nature of our Galaxy by observing a clearly defined spiral pattern (such as that observed for M51, the Whirlpool galaxy). In fact, the exact number and extent of spiral arms in the Galaxy is not known. Spiral arms are best traced by OB (O and B stars are hot, very massive stars) associations [Vogel *et al.* (1990)]. However, in our Galaxy, spiral structure is best revealed by radio wavelength tracers, particularly the millimeter wave rotational transitions of CO, due to high optical extinction. [however, see Combes (1991)]. A major problem in using millimeter wave observations to determine the spiral structure of the Milky Way is the large uncertainty in the kinematic distances derived. This is particularly significant in the inner Galaxy ($\mathrm{R} < \mathrm{R}_0$), where the Galactocentric radii derived from kinematic information is doubly valued. Chapter 3 of this thesis is devoted to measurements of the molecular properties of the spiral arm at R = 13 kpc, first observed in molecular tracers by Mead (1986).

1.3 Details of the $^{12}\mathrm{CO}\ (\mathrm{J} = 1 \rightarrow 0)$ Transition

The $^{12}\mathrm{CO}\ (\mathrm{J} = 1 \rightarrow 0)$ is the rotational transition from the first excited rotational energy level to the ground state. For a diatomic molecule, the rotational energy levels are given by the expression

$$E_{rot} = hBJ(J+1) \tag{1.1}$$

where h is Planck's constant, $B = h/8\pi^2 I$, I is the moment of inertia of the molecule, and J is the rotational quantum number. For CO, $B = 57.6\,\mathrm{GHz}$ or $2hB/k = 5.5\,\mathrm{K}$, where k is Boltzmann's constant. A plot of energy levels is shown in Figure 1.2. The spontaneous emission coefficient for the $J = 1 \rightarrow 0$ transition, A_{10}, is $1 \times 10^{-7}\ \mathrm{s}^{-1}$. As explained in Chapter 2, observations of $^{12}\mathrm{CO}\ (\mathrm{J} = 1 \rightarrow 0)$ trace the extent of a molecular cloud and are a measure of the kinetic temperature of the cloud.

1.4 Current Unanswered Questions

In this work, I hope to address some of the current unsolved problems pertaining to molecular clouds. Some of these issues pertain to all molecular clouds, not just clouds in the outer Galaxy. It is my hope that this and future investigations of molecular clouds will provide insights into the following problems: determination of cloud masses, importance of the size-linewidth relation, existence of cold molecular clouds and cloud formation.

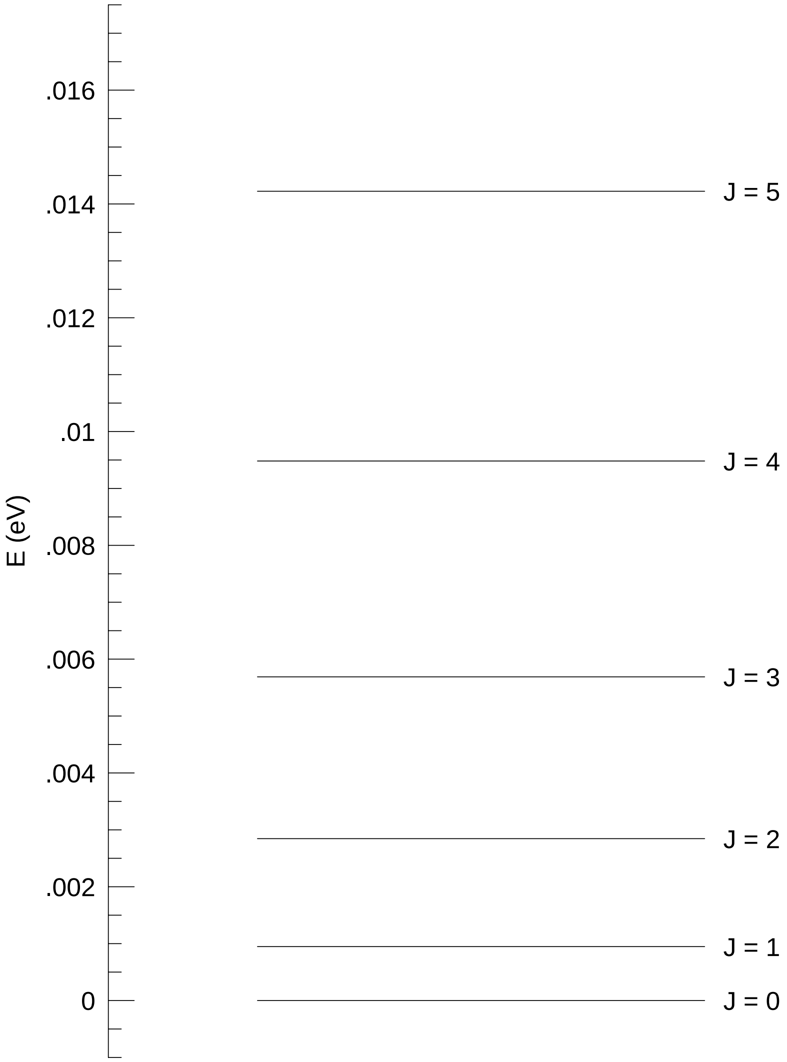

Figure 1.2: Rotational energy levels for ^{12}CO

1.4.1 Determination of Cloud Mass

At the present time, two methods are predominantly used (although others exist) to calculate the mass of a molecular cloud, the virial approximation and direct conversion of CO line luminosity to cloud mass (which I will call the X factor method). Both methods have potential flaws. For the virial approximation, the clouds must be gravitationally bound and have enough time to reach equilibrium. The X factor mass estimate has no sound theoretical basis and appears to be strongly dependent on cloud environment. In Section 2.6.5, I discuss which mass estimate is most appropriate. The results of this discussion will be used to determine corrections to previous total molecular mass estimates of the outer Galaxy.

1.4.2 Importance of the Size-Linewidth Relation

The size-linewidth relation is an empirical correlation between the physical size of a molecular cloud and the observed linewidth (usually of the ^{12}CO ($J = 1 \rightarrow 0$) transition). It has been used to support a variety of conclusions including virial equilibrium, pressure bounding of molecular clouds and the constancy of column density for molecular clouds [Lequeux *et al.* (1993)]. This correlation is statistical in nature only. In Section 4.5, I will explore this correlation in some detail and outline possible problems with using this relation to make determinations about cloud properties.

1.4.3 Importance/Existence of Cold Molecular Clouds

The suggestion of Lequeux *et al.* (1993) that cold molecular material could be a possible component of dark matter is very interesting. Two questions to address if this hypothesis is true are : why are molecular clouds in the outer Galaxy very cold, and what are the implications of this cold cloud component on the molecular mass of the inner Galaxy; that is, does this population of clouds extend into the inner Galaxy. I will explore the possibility of very cold molecular clouds in Chapter 5.

1.4.4 Cloud Formation

Currently, there are two competing theories of cloud formation: ‘top-down’ and ‘bottom-up’. The ‘top-down’ theory [Elmegreen (1993b)] considers the formation of molecular clouds from larger HI super-clouds through various types of instabilities (gravitational, Parker, magnetosonic). The ‘bottom-up’ theory [Kwan & Valdes (1987)] is that giant molecular clouds form through aggregation of smaller clouds by collisions.

Both types of theories use the gravitational potential of spiral arms to facilitate cloud formation. The ‘top-down’ theory needs spiral arms to provide triggering mechanisms for the collapse of the HI super-clouds from which molecular clouds condense. The ‘bottom-up’ theory uses the gravitational potential of the spiral arm to increase the number density of small clouds and the likelihood of a collision between them. Studies of cloud distributions in spiral arm and interarm environments may provide information, which can help distinguish between these theories. As both theories predict that giant molecular clouds will form predominantly in spiral arms, it is difficult to distinguish between these theories using observations of GMCs only. By examining the distribution of small clouds, which are the building blocks of the ‘bottom-up’ theories and the end result of the ‘top-down’ theories after GMC destruction and fragmentation, it might be possible to distinguish between these two types of theories. One of the goals of this thesis will be to provide a set of data with which to test these theories.

1.4.5 Cloud Destruction

Studies of the cloud formation process are further complicated because little is known about the opposite process, cloud destruction. It is current wisdom that GMCs are disrupted by the massive stars that they form. The details of the destruction process have not been well studied. Leisawitz (1985) studied molecular emission around young stellar clusters and determined that clouds are not simply vaporized by star formation. Instead, the clouds fragment and drift away from the stellar cluster. Observations of small clouds in interarm environments may provide information on what happens to the remnants of a GMC after the star formation process.

1.5 Thesis Goals

The main objective of this thesis is to gain a better understanding of how the physical properties of molecular clouds vary based on the environment, spiral arm or interarm, in which the clouds exist. In particular, cloud masses, sizes and kinetic temperatures will be analyzed as a function of cloud environment. Also, the cloud size spectrum as a function of environment will be calculated. In addition, the contribution of small clouds to the total molecular mass of the outer Galaxy will be examined using the unbiased set of observations which comprise the data used in this work.

1.6 Thesis Organization

This thesis is divided into seven chapters. Chapter 2 details the observations conducted and the data reduction necessary to derive physical properties for the clouds identified. Chapter 3 discusses the molecular nature of the 13 kpc spiral arm. Chapter 4 is an investigation of the physical properties of clouds as a function of cloud environment. In Chapter 5, I discuss the implications of this work on estimates of the total molecular mass in the outer Galaxy. A discussion of results is provided in Chapter 6. Chapter 7 summarizes the main results of this work and suggests some future directions of investigation.

CHAPTER 2

OBSERVATIONS AND GENERAL DATA REDUCTION

The observations comprising the data used in this thesis are from a sensitive survey of ^{12}CO ($J = 1 \rightarrow 0$) (rest frequency, $\nu_0 = 115.271$ GHz) emission in a 0.8 square degree region of the outer Galaxy. I intended to observe a full square degree for the survey; however, due to scheduling and weather constraints only 80% of the planned data was taken. This survey was designed to provide an unbiased sample of the distribution of molecular clouds in the region. Earlier surveys of molecular material in the outer Galaxy preferentially identified large and/or star forming clouds due to instrumentation effects (large beam size) [Digel *et al.* (1990)], lack of coverage [Mead & Kutner (1988)] and source selection effects [Wouterloot & Brand (1989)]. The current survey has sufficient sensitivity and resolution to identify small ($d \leq 5$ pc) and/or cold ($T_K \sim 5$ K) clouds which were undersampled in previous work.

The region is centered on $l = 76.37°$, $b = 1.5°$. This region was chosen because it contains a strong HI feature at $R \approx 13$ kpc [Henderson *et al.* (1982)] and follows the warp of the Galactic plane [Wouterloot *et al.* (1990)]. In addition, the Galactic longitude of the region is such that a wide range of Galactocentric radii can be observed in the bandpass permitted by the instrumentation.

2.1 Observing Program and Strategy

The observations were conducted using the NRAO 12m telescope on seven different observing runs between May 1991 and December 1993 (see Table 2.1). The observations were conducted in collaboration with Dr. Marc Kutner, my thesis advisor, and Dr. Kathryn Mead. Modifications to the sub-reflector (secondary mirror) between the 1992 and 1993 observing runs markedly improved the telescope's

Table 2.1: List of Project Observing Dates

Run Number	Dates Observed	Comments
Run 1	06/3/91-06/10/91	
Run 2	12/15/91-12/19/91	
Run 3	06/18/92-06/25/92	
Run 4	11/19/92-11/24/92	
Run 5	02/21/93	Sub-reflector spillover guard installed
Run 6	05/21/93	Clean up observations
Run 7	12/15/93	Clean up observations

system temperatures, by reducing the amount of stray ground radiation transmitted into the telescope feed, but did not otherwise change the efficiency of the instrument.

The observations were made in absolute position switched mode using a reference position at $l = 76.5°$ and $b = 2.5°$. In absolute position switched mode, each individual observation of a position by the telescope is compared with an observation of the reference position. Both the position of interest and the reference position are observed for the same amount of time. The resultant spectrum is the ratio of the difference between the total power per channel for the source and reference positions to the total power per channel of the reference position. Position switching is done to remove the effects of atmospheric emission, the optics of the telescope and the electronics of the receiver. As one of the goals of this project was to identify weak emission from small clouds, special care was taken to make sure that the off position was free of emission throughout the bandpass. The reference position was differenced with several other potential references and was found to be emission free at a level of .05 K (see Figure 2.1).

The positions observed are shown in Figure 2.2. The spacing between adjacent positions is 60", approximately one beamwidth (full width at half maximum or FWHM) of the 12m at 115 GHz. Figure 2.3 is a schematic of the spacing between

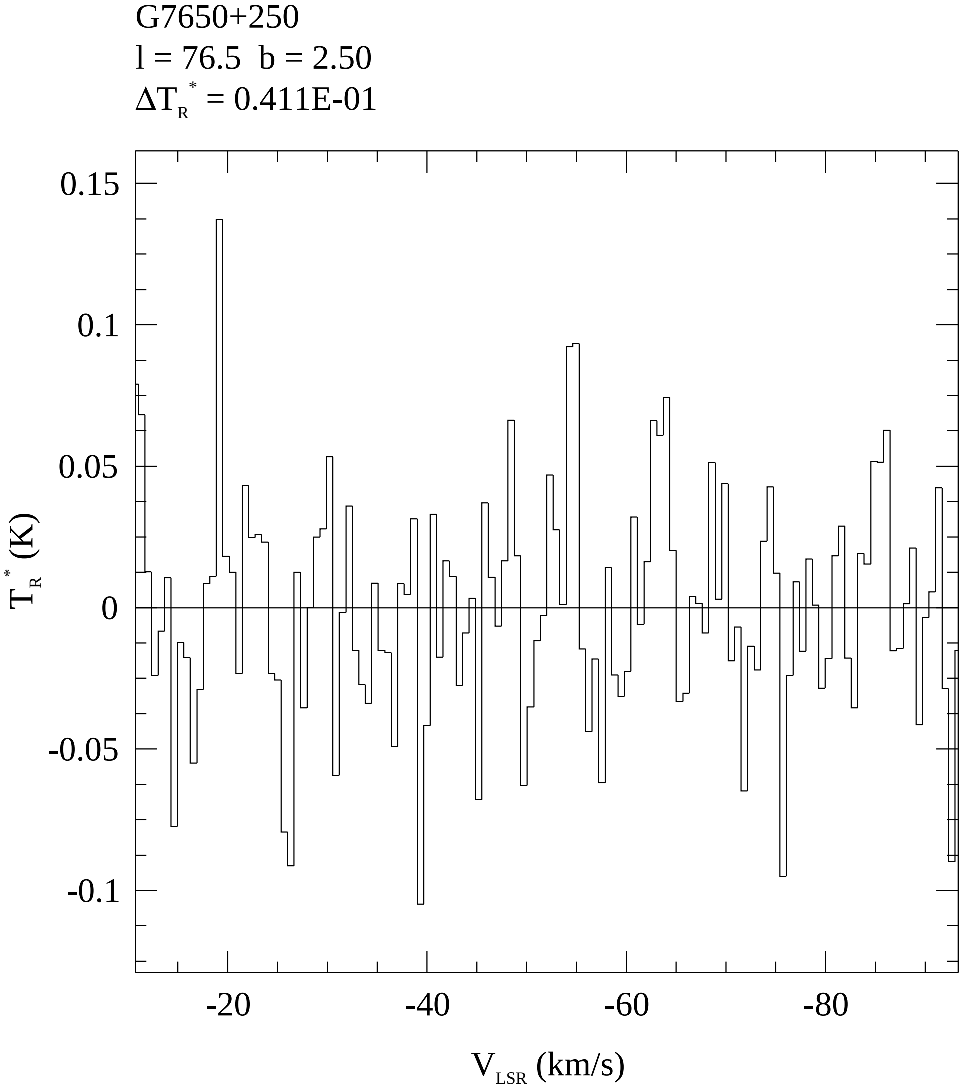

Figure 2.1: Spectrum of reference position, G7650+250

adjacent positions and the solid angle filled by the main beam for each pointing. Sixty-three percent of the solid angle for each position is filled by the main beam of the telescope. Each position was simultaneously observed using the two orthogonal linear polarizations provided by the telescope. Three different digital backends were used: a 250 kHz filterbank, a 500 kHz filterbank and a hybrid correlator set to a bandwidth of 195 kHz/channel. The filterbanks have 256 channels each, which were divided into 2 blocks of 128 channels. One block was used for each polarization observed. The hybrid correlator consists of 2048 channels with a number of redundant channels which are necessary to perform autocorrelation on the signal. As a result, there are 1536 channels available with possible resolutions varying between 24 and 781 kHz.

For many of the scans, the hybrid correlator data is corrupted by a large scale ripple. For this reason, I will primarily use the 250 kHz and 500 kHz data in the following analysis. For ^{12}CO ($J = 1 \rightarrow 0$), the 250 kHz filterbank provides a spectral resolution corresponding to $\Delta v = 0.65\ \mathrm{kms}^{-1}$, allowing identification of narrow lines. As the spectral resolution of the 500 kHz data is too low to resolve narrow lines, it is used primarily to confirm bad channels in the 250 kHz data and the integrity of the baselines.

Two representations of the entire data set are shown in Figures 2.4 and 2.5. Figure 2.4 is a grayscale image of the integrated intensity of the ^{12}CO ($J = 1 \rightarrow 0$) line in this area of the sky. Figure 2.5 is a grayscale map of the peak line temperature. Both figures have been smoothed using the REDUCE software [Mizuno (1994)]. The largest structures in each figure consist of one or more giant molecular clouds.

2.1.1 Telescope Parameters

The NRAO 12 m radio telescope consists of a 12 meter primary with a surface accuracy of 77 μm ($= \lambda/34$ for 2.6mm), an adjustable sub-reflector and two

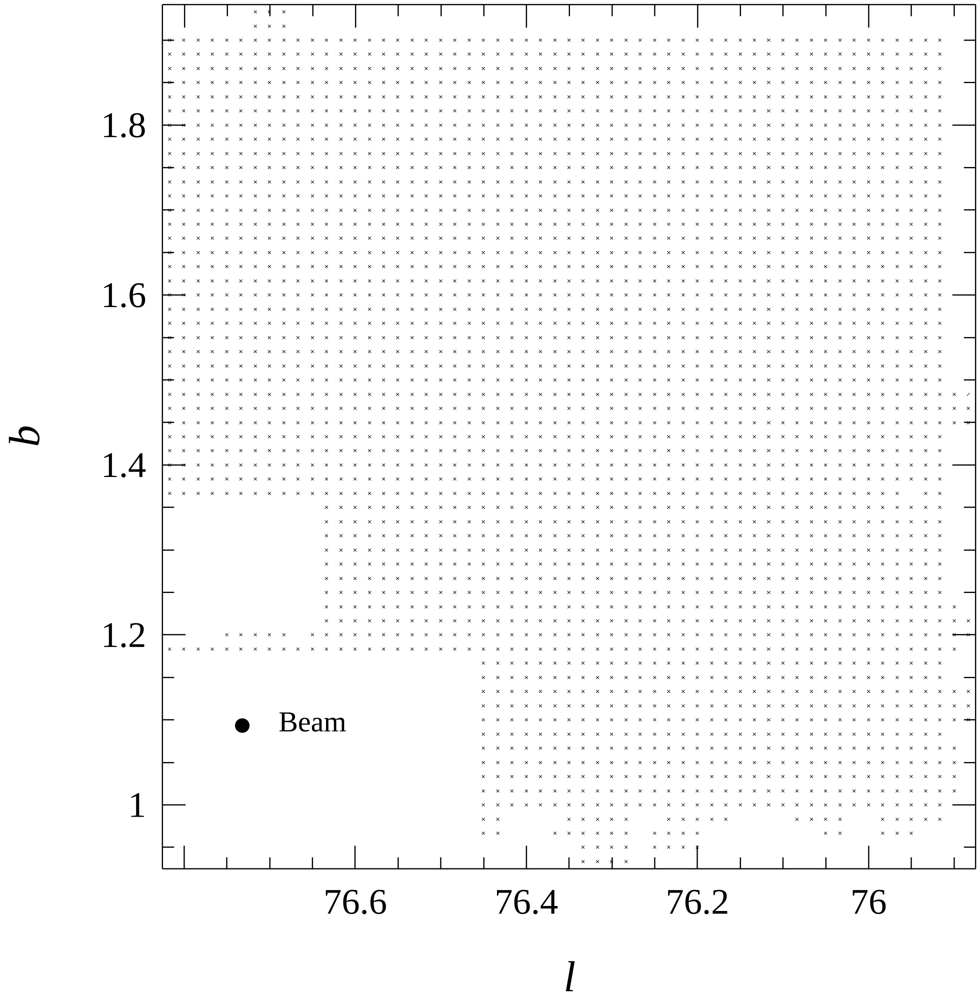

Figure 2.2: Positions mapped in ^{12}CO (J = 1 → 0)

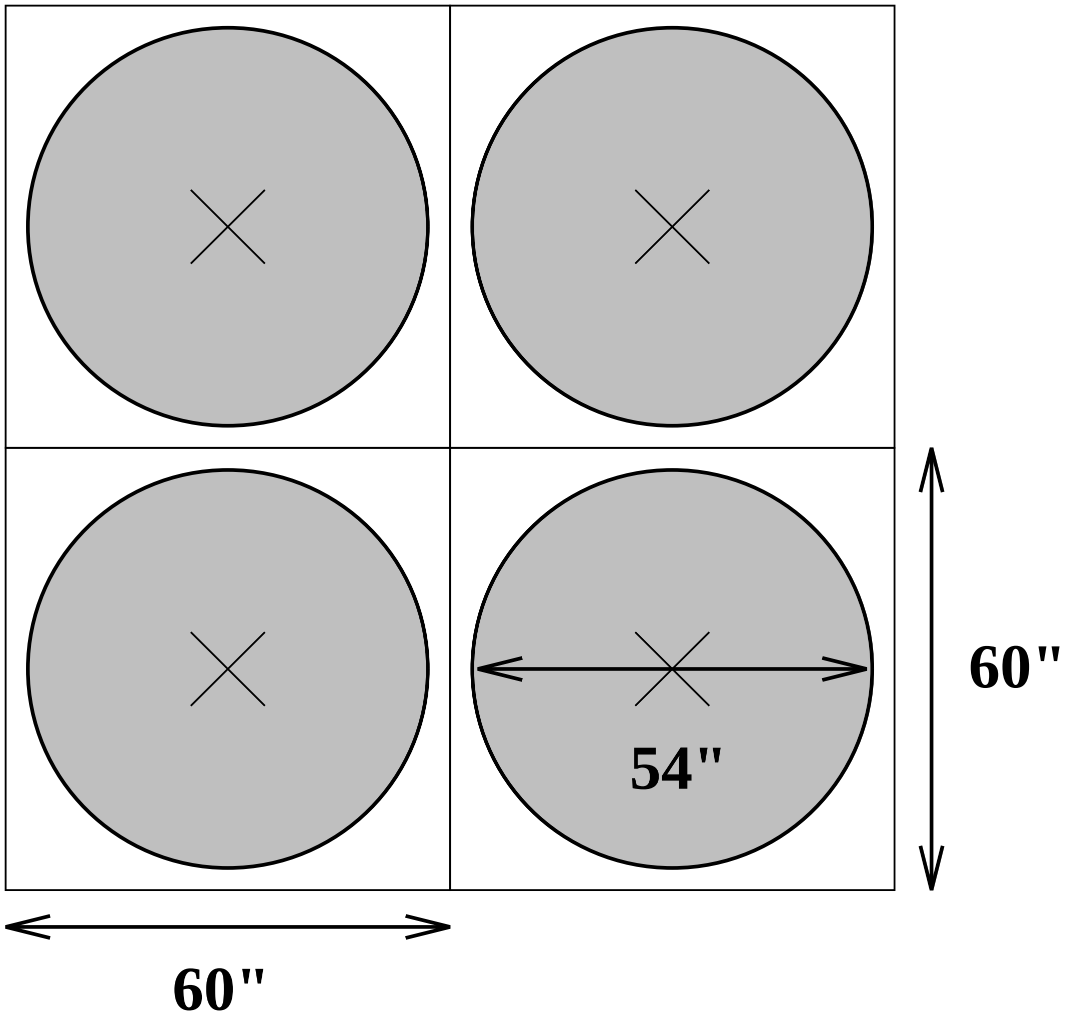

Figure 2.3: Schematic of main beam size relative to grid spacing

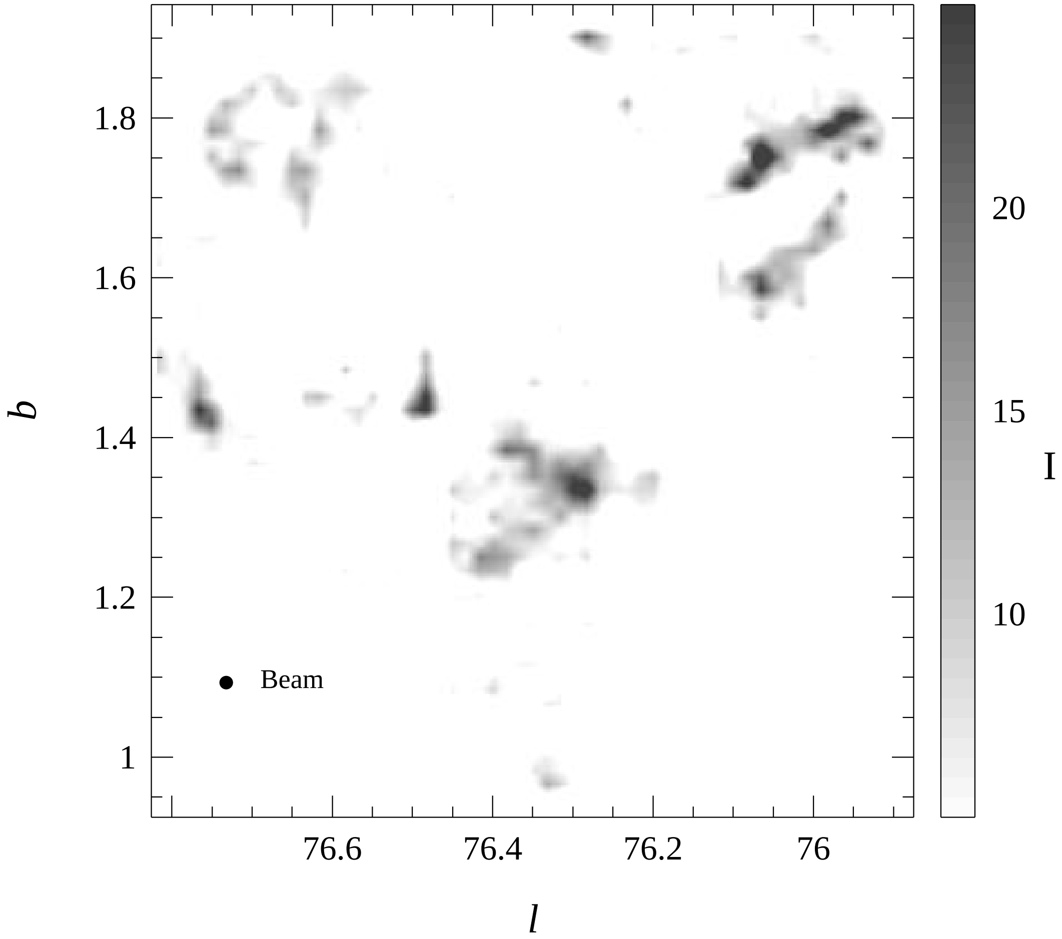

Figure 2.4: **Grayscale image of integrated intensity. The gray levels range from** 5 **to** $25\,\mathrm{Kkms}^{-1}$**. The beam size is displayed in the lower left hand corner.**

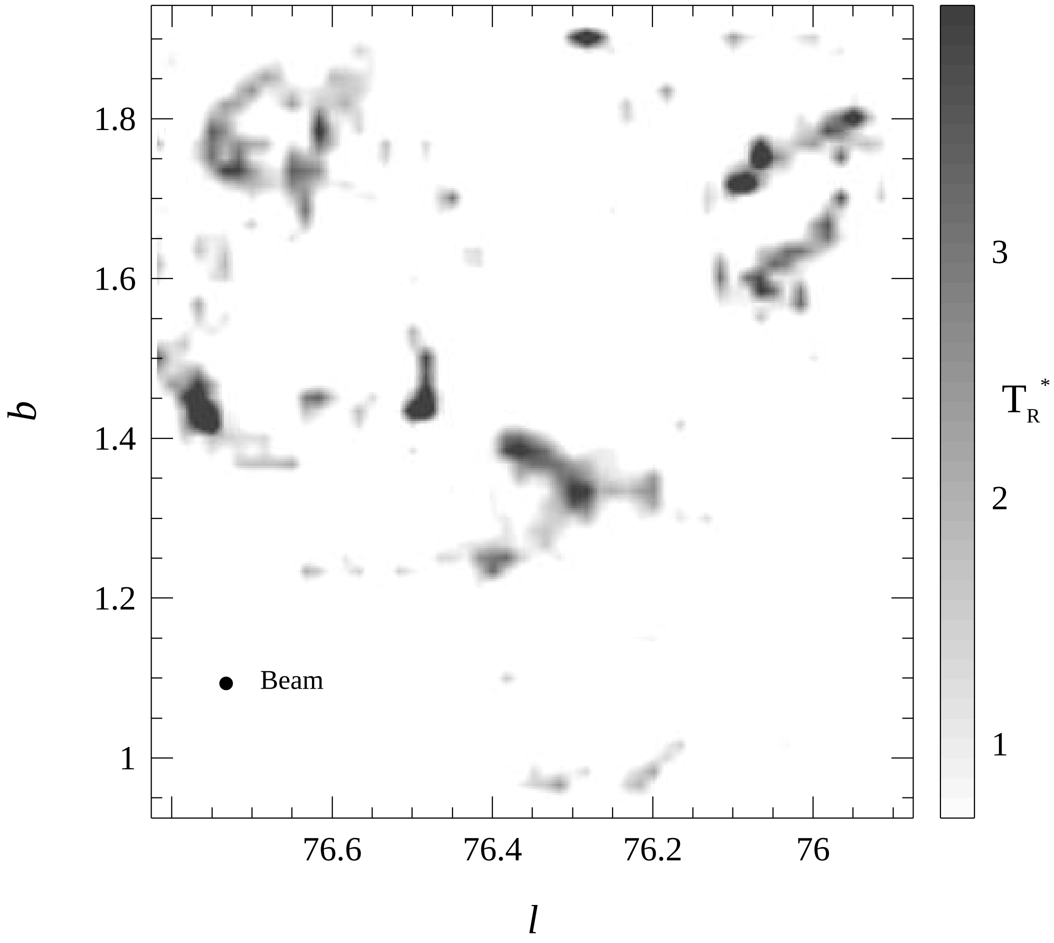

Figure 2.5: Grayscale plot of peak line intensity as a function of l **and** b**. The gray levels range from** $T_R^* = .7\,\mathrm{K}$ **to** $4.0\,\mathrm{K}$**. The beam size is displayed in the lower left hand corner.**

Table 2.2: System Parameters for NRAO 12 Meter Telescope[a]

Dish diameter	12.0 m
Main Beam diameter at $\nu = 115$ GHz	54”
RMS surface accuracy	77 μm
Receiver temperature	$T_{rx} \approx 100$ K
Forward spillover efficiency (η_{fss})	0.75
Rearward spillover efficiency (η_l)	0.85
Corrected main beam efficiency (η_M^* or η_c)	0.86
FWHM of main beam	54”
FWHM of error beam	17′
Ratio of error beam to main beam amplitudes (A_E/A_M)	6×10^{-4}

[a] [NRAO 12m Users’ Manual (1990)]

orthogonal receivers with SIS superheterodyne mixers. The major system parameters, including the various telescope efficiencies at a frequency of 115 GHz are given in Table 2.2, and a block diagram outlining the major components of the 12 meter is shown in Figure 2.6. The most important properties of the telescope to the data analysis process are the FWHM of the main beam, which is the resolution of the instrument, and the corrected main beam efficiency, η_M^*, which is the fraction of the total power received after correcting for ohmic losses, rearward and forward spillover and scatter that comes from the main beam (as opposed to the error beam). In the limit of a source filling the main beam, the source coupling efficiency $\eta_c = \eta_M^*$.

2.1.2 Contribution to Signal from Error Beam

An important concern when looking for weak signals is possible contamination of a spectrum by contributions to the signal from sources in the error beam. If the error beam is completely filled, it contributes up to 14% of the signal that is measured. Assuming a brightness temperature T_B of 1 K for sources in the error beam, clouds in the error beam would contribute .14 K (which is of the order of the root mean square [rms] noise) to the observed signal. As shown by the channel maps of Leung and Thaddeus (1992), the amount of emission that fills the error

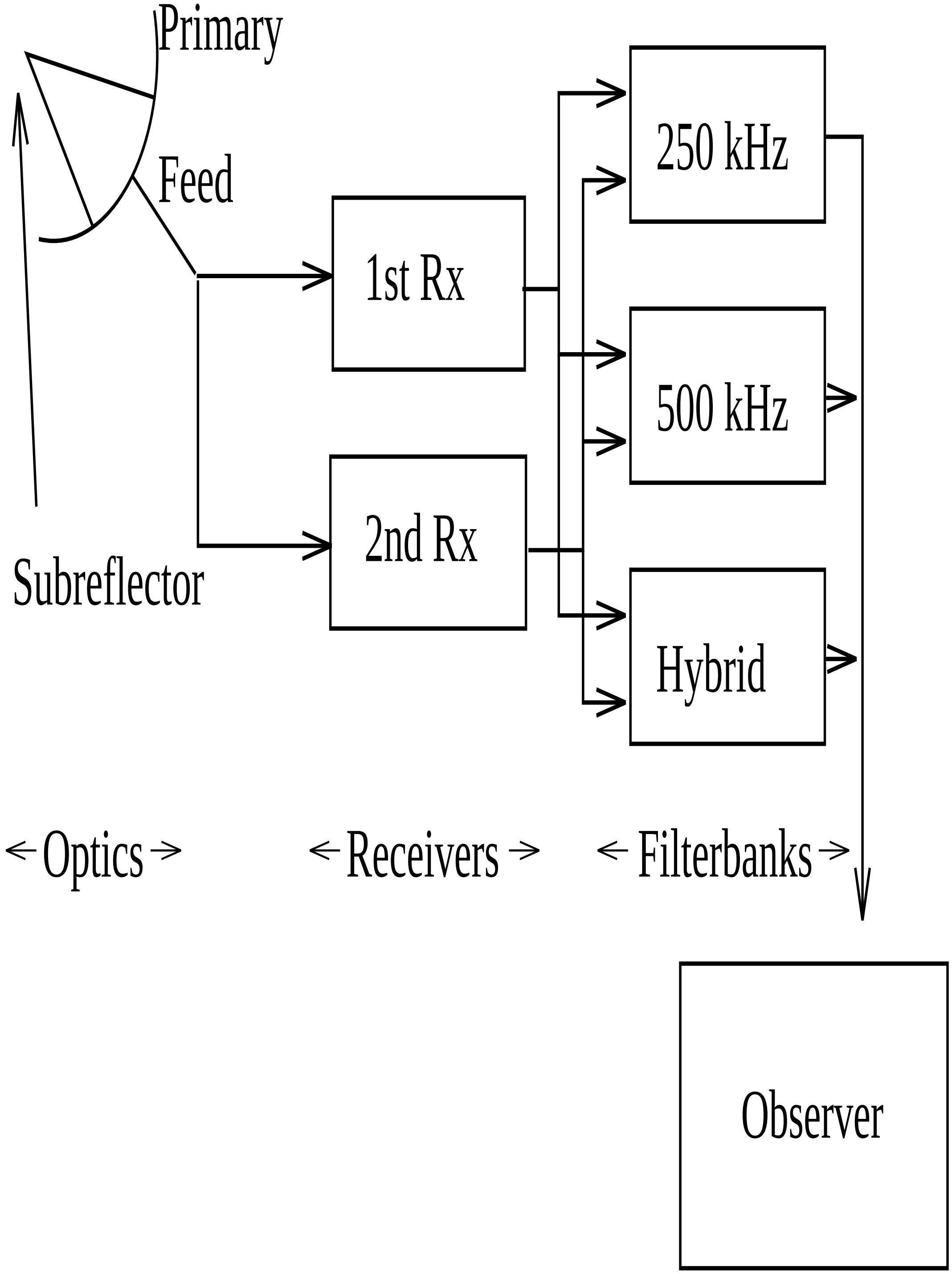

Figure 2.6: A block diagram of the various components of the NRAO 12 meter telescope.

beam over the region and velocities of interest is negligible. Emission in the error beam contributes significantly less than the rms noise level. It is difficult to estimate the maximum contribution without a detailed examination of the spectra of Leung & Thaddeus; however, I estimate it to be no more than .05 K for the peak channel. Contributions due to sources outside the main diffraction pattern are eliminated by comparison of the source positions with the nearby reference position.

2.2 Pointing and Calibration

The telescope pointing was checked and corrected approximately every 15° in elevation using standard sources Jupiter and DR21. For the observations in 1991 and 1992, a rising/setting pointing asymmetry of 5-15 arcseconds in elevation was noted. The pointing was checked by observing in a cross-shaped pattern a strong millimeter point source. The observations are spaced a half beamwidth apart. A two-dimensional Gaussian function was then fit to the observations. Subsequently, the pointing was adjusted by the difference between the Gaussian fit and the position of the central scan in the cross. I estimate the pointing for all observations to be accurate to better than 10 arcseconds, which is $\sim 20\%$ of the beamwidth.

The focus of the telescope was adjusted by changing the position of the sub-reflector to focus radiation from a point source. These focalizing observations were conducted daily at the start of the observing program and consisted of adjusting the position of the sub-reflector until the signal from Jupiter (a strong available millimeter point source) was maximized.

The observations were calibrated using the chopper wheel technique of Kutner & Ulich (1981). All results are reported on the $\mathrm{T}_{\mathrm{R}}^{*}$ scale. $\mathrm{T}_{\mathrm{R}}^{*}$ is the flux (in temperature units) received corrected for atmospheric losses, gain of the instrument and forward and rearward spillover and scattering. Standard sources DR21(OH) and Orion A (see Figures 2.7 and 2.8) were observed to check the calibration of the

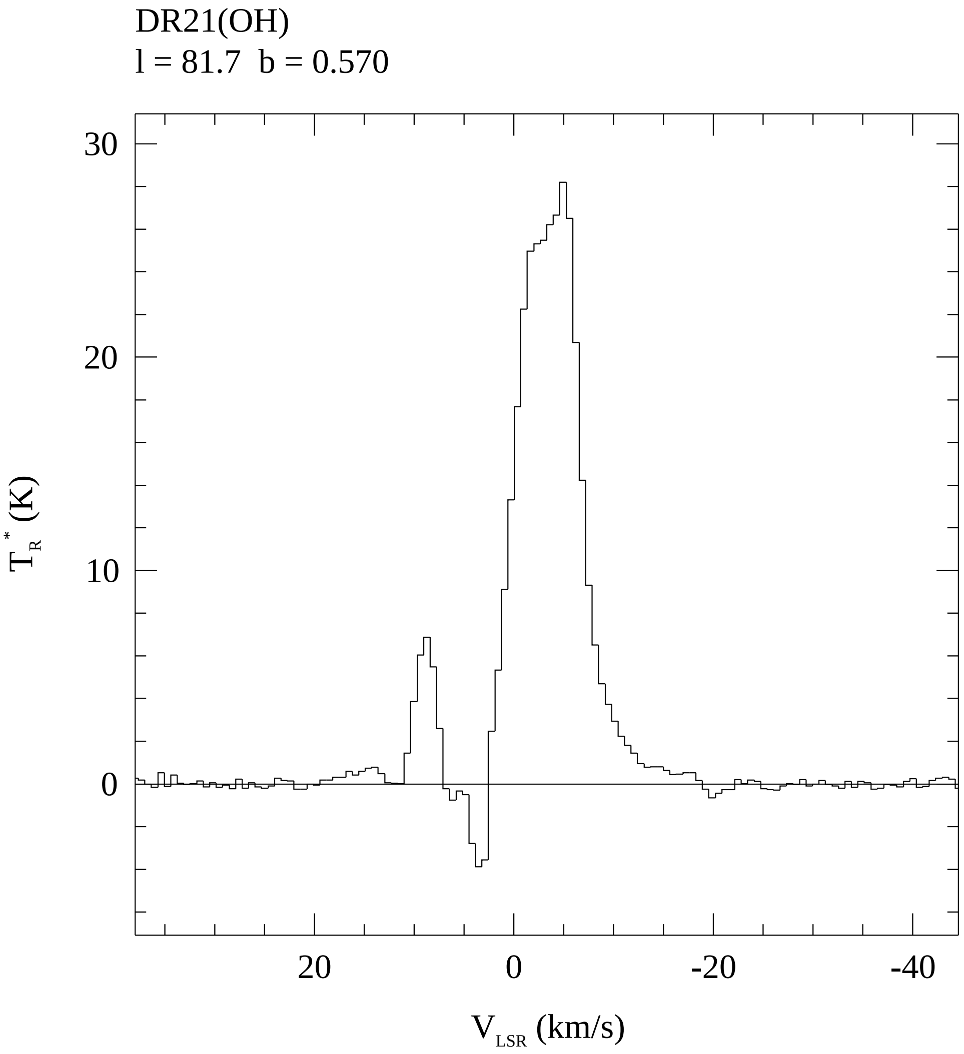

Figure 2.7: Sample spectrum of calibration source, DR21(OH)

telescope. The spectra obtained agree with previous observations taken at the 12 meter. In addition, we frequently monitored a source near the survey region called GCAL (l = 75.6°, b = 1.25°, $v_{LSR} = -42\,\mathrm{kms}^{-1}$, $T_R^* = 2.2\,\mathrm{K}$, see Figure 2.9); line temperatures of this source varied by less than 10% throughout the seven observing runs. In general, the line temperatures reported in this work are good to 10%. Each position was observed until a rms noise level of $\Delta T_R^* \approx 0.1\,\mathrm{K}$ (1σ) was achieved. For typical system temperatures of $T_{SYS} = 400 - 600\,\mathrm{K}$, integration times of 2 to 6 minutes were needed.

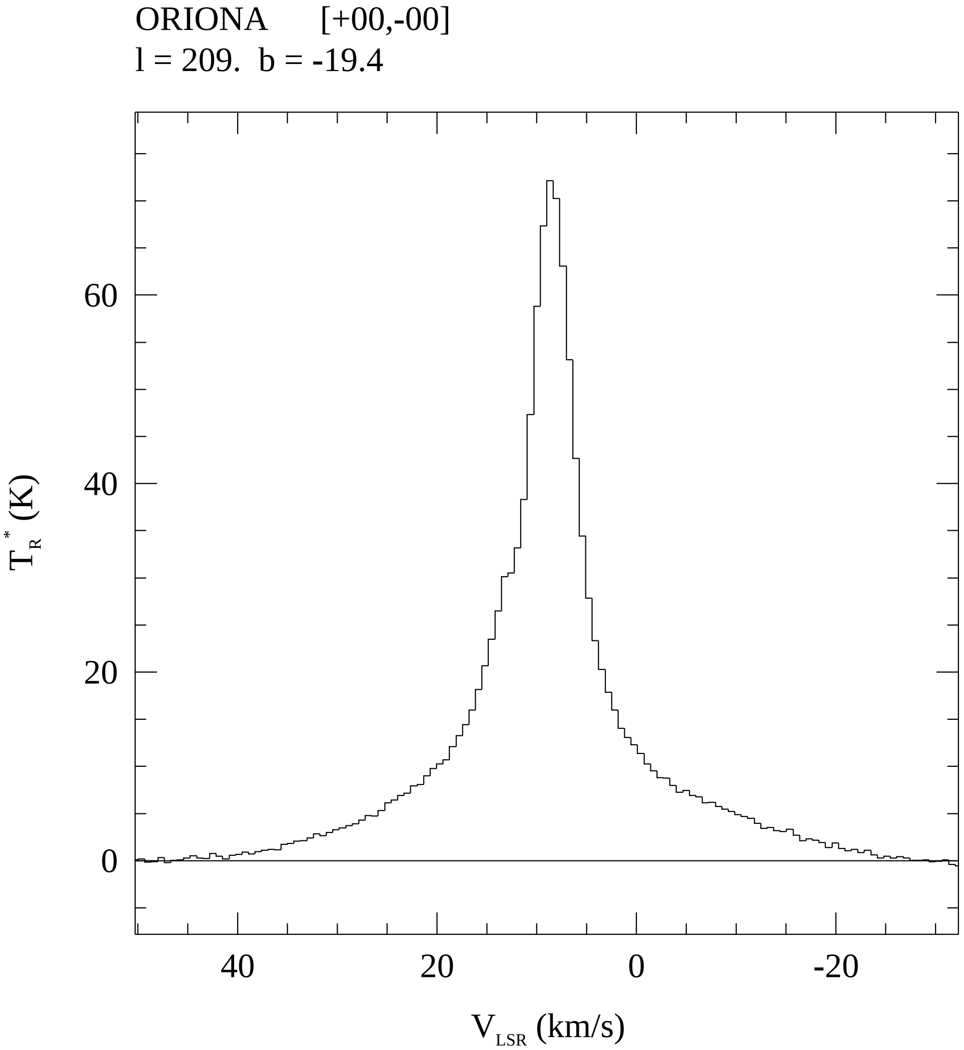

Figure 2.8: Sample spectrum of calibration source, Orion A

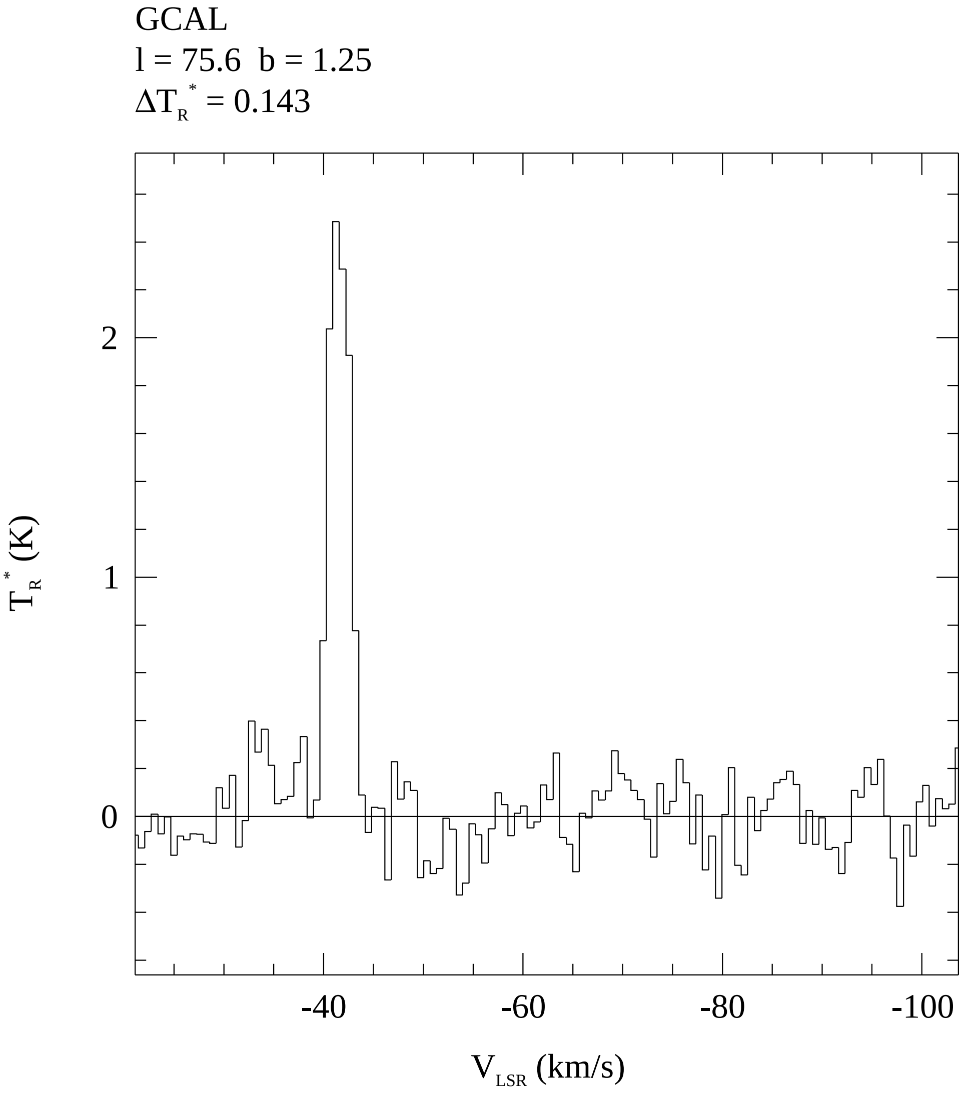

Figure 2.9: Sample spectrum of calibration source, GCAL

2.3 Spectra Processing

All data reduction was done using the REDUCE system, a X-window based, user friendly data processing package for single-dish radio observations. Spectra were visually investigated, using the simultaneously observed orthogonal polarizations to identify bad channels and aberrant spectra. Bad channels were deleted from each spectrum. When appropriate, the polarizations were averaged together. The averaged spectra had polynomial baselines subtracted. 56% of the spectra had linear baselines subtracted, and 94% of the baselines were third order or less. In the few cases where a higher order baseline was used, the amplitude of the higher order terms was small. The utility of using baselines of order 4 or greater may be questioned; however, they are a necessary evil in attempting to identify weak emission in spectra with small but significant curvature. The data from the first two observing runs were taken with a slightly different center velocity ($v_c = -52\,\mathrm{kms}^{-1}$), and the channels were shifted, so that they coincide with the rest of the data ($v_c = -62.4\,\mathrm{kms}^{-1}$). The last five channels on each end of the bandpass were dropped, as the baselines are much less reliable at the ends of the spectra. As a result, the useful velocity coverage of the data is $-100\,\mathrm{kms}^{-1}$ to $-25\,\mathrm{kms}^{-1}$. Examples of raw data, data after bad channel deletion and data after baselining are given in Figures 2.10 - 2.12. Relevant processing information is detailed in Table 2.3.

2.3.1 Baseline Bias

During initial processing, a subtle bias in setting the baseline regions around potential (but weak) emission resulted in a positive residual in most of the baselines fit. REDUCE uses a least squares method (Marquandt's method [Press *et al.* (1988)]), which determines the best-fit polynomial by minimizing the rms residuals in the regions selected for the fit. These regions are assumed to be emission free. By including more negative channels than positive channels in the

Table 2.3: Scan Processing Statistics

Baseline Order	Number of Scans	% of Total Scans	Average RMS	Max RMS	Min RMS
1	1547	6514	0.1	0.22	0.03
2	744	27.0	0.1	0.18	0.03
	287	10.4	0.1	0.22	0.06
		4.3	0.1	0.21	0.05
					.05

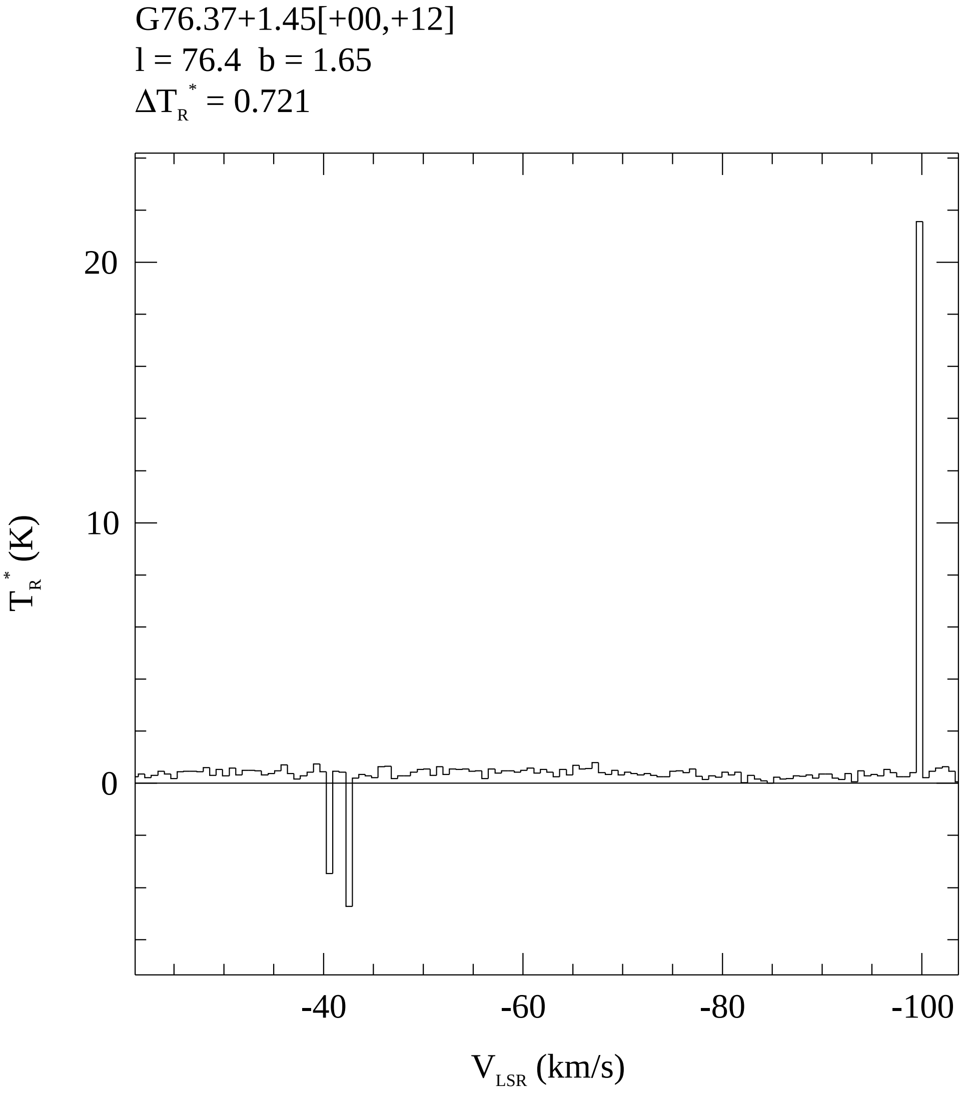

Figure 2.10: Example of spectrum before processing

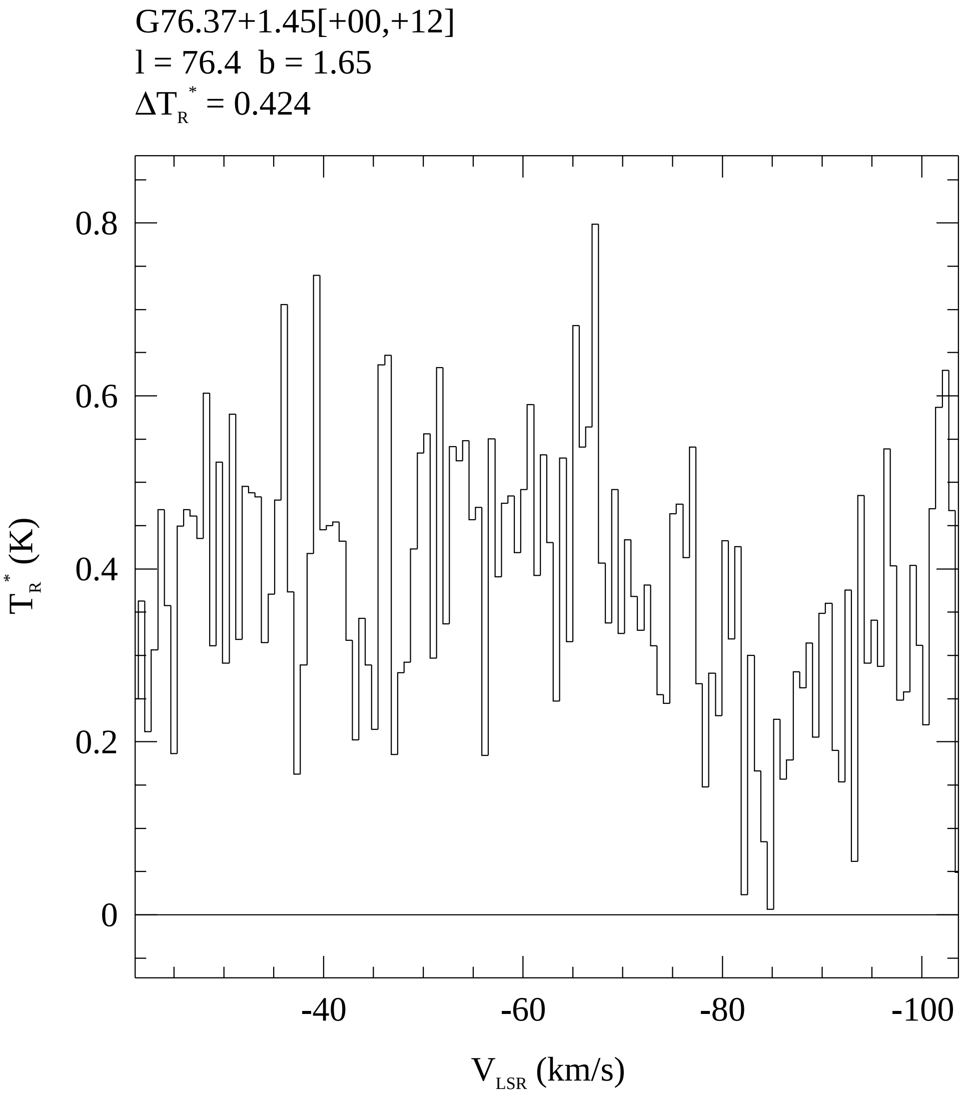

Figure 2.11: Example of spectrum after deletion of bad channels

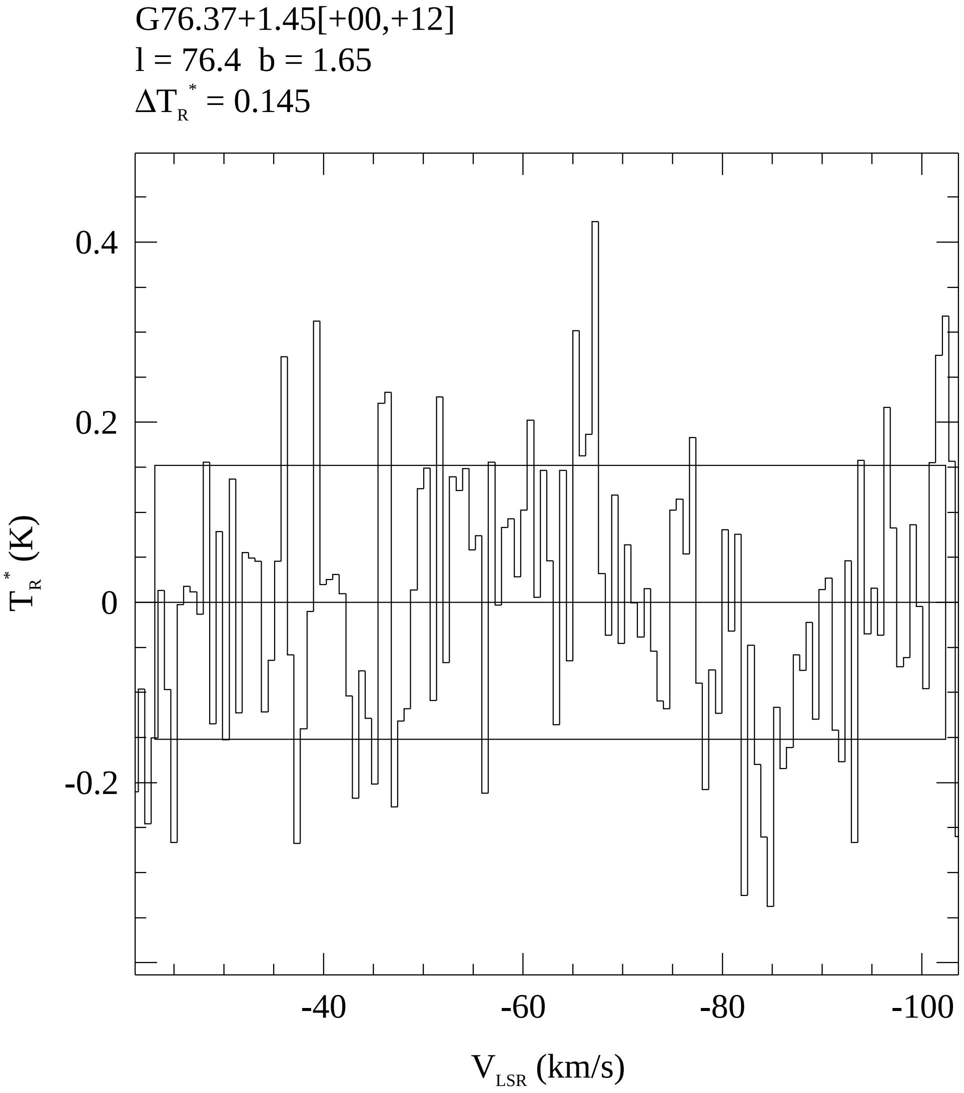

Figure 2.12: Example of spectrum after baselining

baseline regions, the zero point of the processed spectra is lowered resulting in a positive residual. As a result, an initial composite spectrum of the region had a positive offset which mimics a pervasive low level emission. To test this hypothesis, I developed an automated baselining algorithm, which baselines around both positive and negative excursions equally. When this algorithm was applied to the data set, the positive residuals disappeared. The difference between individual baselines for the two different methods (setting regions by hand and unbiased automatic baselining) is usually less than .01 K (1/10th of the rms noise) on a channel by channel basis. While this difference is insignificant in any individual spectrum, the uncertainties introduced in the composite spectrum make it difficult to learn anything about the nature of weak emission. The implications of baseline bias will be discussed in more detail in Section 5.2.1.

2.3.2 Description and Implementation of Automated Baselining Algorithm

Before useful information can be obtained from a spectrum, spurious contributions to the data from the instrument and incomplete subtraction of atmospheric signal must be identified and removed. In general, the data received from the telescope can be described as

$$I(\nu) = S(\nu) + A(\nu) + \epsilon(\nu) \tag{2.1}$$

where $I(\nu)$ is the observed data as a function of frequency ν, $S(\nu)$ is the signal from a molecular cloud, $A(\nu)$ is the unwanted contribution from instrument and sky, and $\epsilon(\nu)$ is the noise component of the signal. $S(\nu)$ has a functional form which can be reasonably approximated by one or two Gaussians. The random variable $\epsilon(\nu)$ is normally distributed with a dispersion which is theoretically given by

$$\Delta T = \frac{\alpha_{sys} T_{sys}}{\sqrt{Bt}} \tag{2.2}$$

where ΔT is the rms noise temperature per filterbank channel, α_{sys} is a constant which depends on the number of polarizations averaged together ($\alpha_{sys} = 1$, for my observations), T_{sys} is the system noise temperature, B is the bandwidth of an individual channel in Hz and t is the total integration time in seconds. $A(\nu)$ is the unwanted signal due to the instrument and sky. $A(\nu)$ does not have a simple functional form, but it can be adequately approximated by a polynomial function. To remove the contributions due to instrument and sky, a polynomial function is fit to the regions of the spectrum not containing emission from molecular clouds. If the residuals of the fit to $A(\nu) + \epsilon(\nu)$ have a variance equal to ΔT and the fit behaves nicely in the regions where $S(\nu) \neq 0$, then the fit is considered good.

I developed an automated method to remove the contribution of $A(\nu)$. I was motivated by the sheer size of my data set ($>$ 3000 individual spectra) and the potential for error due to bias by a human observer. The algorithm implements the same steps that a human observer (myself, for example) takes in determining a baseline but does so in a more uniform fashion. The algorithm is an iterative procedure, which involves identifying lines and fitting polynomial baselines to the data in the regions between the lines. The algorithm is outlined in Table 2.4. The extra iteration, to check if the baseline is better modeled by a function of opposite parity, is particularly useful in distinguishing between 2nd and 3rd order baselines.

In my implementation of this algorithm, the following specific parameters were used. Only four baseline regions can be set in REDUCE for a given spectrum; therefore, only the four largest (in terms of integrated intensity) lines are baselined around. The strength and width of the lines are free parameters in the algorithm which must be set by the user. It is assumed that the user has some knowledge of the size of the signal. For my work, I varied the minimum strength of the lines to baseline around between 1 and 3 σ with 2.5 σ working the best. The lines were expected to be a minimum of 4 channels wide and a maximum of 20 channels wide. The maximum width of the line is important to specify, since a plateau of bad channels could cause a false line identification. The algorithm fails to successfully baseline such aberrant spectra, but spectra with this type of defect would be discarded by a competent observer anyway. After some experimentation with various goodness-of-fit tests, I determined that an improvement of 10% in the rms noise level is reasonably significant for spectral line data. This criterion is not stringent but is a reasonable and efficient way of getting good baselines. More sophisticated goodness-of-fit tests such as the Student F-Test [Bevington (1969)] are too sensitive and prevent convergence of the algorithm. The failure of more sophisticated tests is expected as the signal-to-noise ratio is low. An improvement of 10% in the rms corresponds to a change in the baseline which is visible to the naked eye. Also, the algorithm converged quickly for this criterion. Demanding a less significant improvement before convergence will cause the algorithm to model the specifics of the noise resulting in a high order polynomial baseline, which may not be well behaved in the region of interest. By modeling the noise too well, the fitting function may not be realistic in the signal region.

The algorithm was tested against manual baselining of the survey data. As mentioned previously, the algorithm baselines data with comparable accuracy and removes any bias. Additional tests of the algorithm using a synthetic data set show that this method is very effective for data with signal strengths $> 3\sigma$ and baselines that are not extremely deviant. The synthetic data consisted of Gaussian signals with normally distributed noise and either a polynomial baseline or a polynomial+sinusoidal baseline. In general, spectra with large scale ripples and/or plateaus of bad channels cannot be reduced using my algorithm (or any other). This method of data reduction is extremely time efficient. The survey data set took approximately 2 months to reduce by hand and 2 hours to reduce using the algorithm.

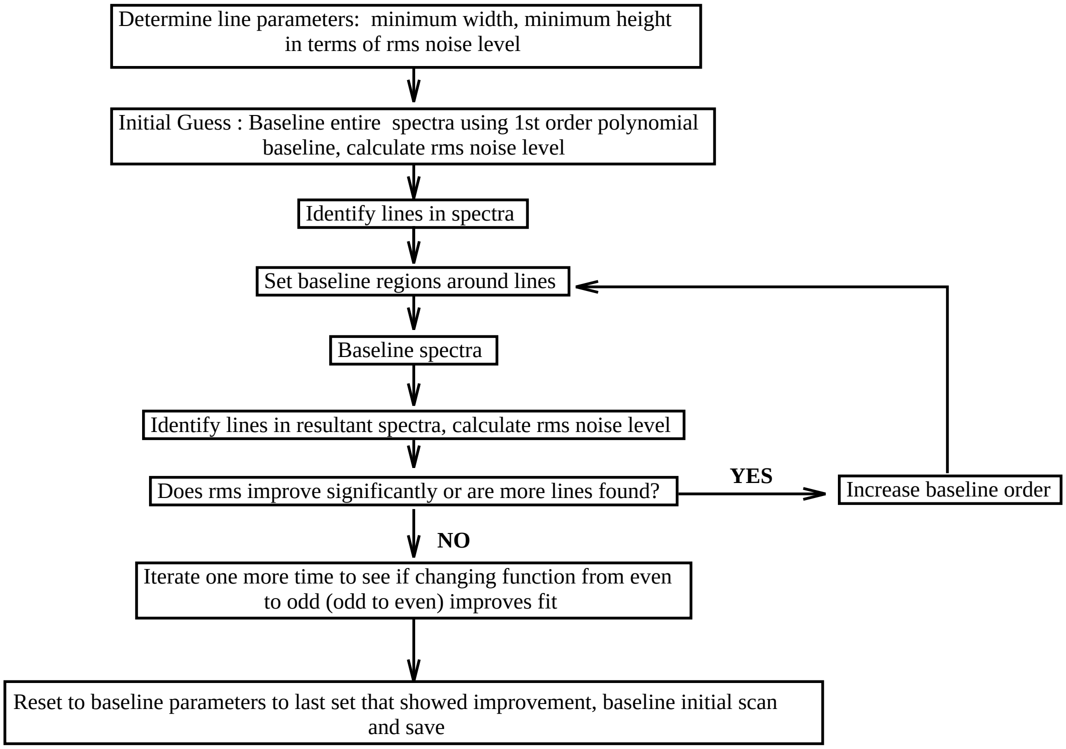

Table 2.4: Outline of Automated Baselining Algorithm

2.4 Distance Determination and Kinematic Parameters

An important quantity, to determine in measuring molecular cloud properties, is the distance to the cloud. Most derivable physical properties of the clouds scale as some power-law of the distance to the cloud. Distances are determined kinematically assuming a flat rotation curve as suggested by [Fich *et al.* (1989)] with the current IAU standards ($\mathrm{R_0} = 8.5\,\mathrm{kpc}$ and $\mathrm{v_0} = 220\,\mathrm{kms^{-1}}$). The Galactocentric radius of a cloud is given by

$$R = \frac{R_0}{1 + \frac{v_{LSR}}{v_0 \sin l}} \tag{2.3}$$

where v_{LSR} is the line of sight velocity of the emission with respect to the local standard of rest. The heliocentric distance of the cloud is

$$d = R\cos\left[\arcsin\left(\frac{R_0}{R}\sin l\right)\right] + R_0 \cos l \tag{2.4}$$

Unfortunately, no secondary distance determinations are available for these molecular clouds; it is impossible to assign an OB association, HII region or other object to these clouds, since they are on the other side of the 1st quadrant. Any optical or infrared tracer is invisible due to extinction by intervening dust and gas.

2.4.1 Uncertainty in Cloud Distance

The Galactocentric radii covered in this survey are 9.6 kpc to 16.0 kpc. Figure 2.13 is a plot of Galactocentric radius and heliocentric distance as a function of v_{LSR}. Non-circular cloud motions such as the random velocities of clouds and streaming motions of clouds [Kwan & Valdes (1987) and Brand & Wouterloot (1988)] along the spiral arm will introduce error in the distance determination. Assigning a cloud velocity dispersion of $\sim 5\,\mathrm{kms}^{-1}$ [Dame (1983)], the error in Galactocentric radius varies from .3 kpc at R = 9.6 kpc to .8 kpc at R = 16.0 kpc. Quantifying the effect of streaming motions is more difficult as I have no independent method of measuring these motions. In general, all distances calculated are good to within a kiloparsec. There is little benefit to using a more complicated rotation curve to determine distances. Other rotation curves are virtually flat; the rotation curve of Brand and Blitz (1993) differs from a flat rotation curve by less than 4% for $R < 17\,\mathrm{kpc}$. In addition, deviations from circular motions create large uncertainties in derived rotation curves reducing the utility of a more complex rotation curve.

2.4.2 Survey Coverage

The linear resolution of the survey varies from 2 pc for R = 9.6 kpc to 4.6 pc for R = 16.0 kpc. The total volume covered by the survey is $0.279\,\mathrm{kpc}^3$. For all Galactocentric radii sampled, the survey region contains at least the half maximum point of molecular emission [Wouterloot *et al.* (1990), also Combes (1991)] and the molecular midplane for $10\,\mathrm{kpc} < \mathrm{R} < 16\,\mathrm{kpc}$. Therefore, this data set should give a representative sample of the molecular emission for 9 kpc < R < 16 kpc in the 1st quadrant. However, the total volume covered by the survey is a very small fraction, 1.5×10^{-3}, of the volume of the molecular outer Galaxy; therefore, results pertaining to the distribution of molecular material in the outer Galaxy are suggestive, but are not definitive. I have approximated the total molecular volume of the outer Galaxy by a flared annulus

$$V_{OG} \approx \pi(R_{max}^2 - R_{min}^2)(z_{max} + z_{min}) \approx 192\,\mathrm{kpc}^3 \tag{2.5}$$

with inner radii $R_{min} = 9\,\mathrm{kpc}$, outer radii $R_{max} = 16\,\mathrm{kpc}$, inner scale-height $z_{min} = 100\,\mathrm{pc}$ and outer scale-height $z_{max} = 250\,\mathrm{pc}$ [Wouterloot *et al.* (1990)].

2.5 Identification and Measurement of Spectral Lines

Physical properties of molecular clouds can be inferred from information gleaned from the emission lines observed. The major steps of this process are:

- Line identification
- Measurement of line properties

These steps will be outlined in the following sub-sections. General properties of the ^{12}CO (J = 1 → 0) line for molecular clouds are

- Simple line profiles – model as a sum of 1-2 Gaussians
- Linewidths of a few km/s
- Typical line strengths greater than a few tenths of a Kelvin

Using these general properties as guidelines, line identification takes place as described in Section 2.5.1.

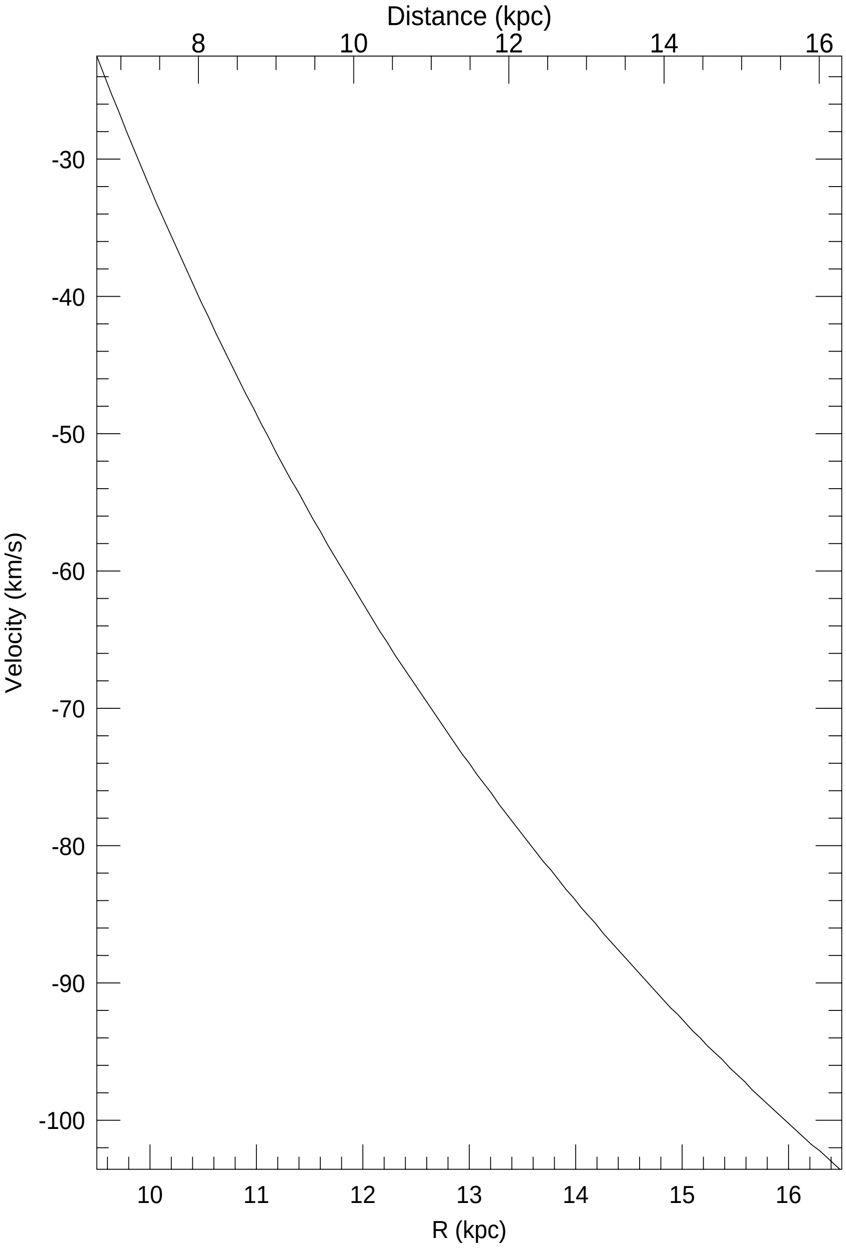

Figure 2.13: Plot of Galactocentric radius and source distance as a function of v_{LSR}.

2.5.1 Line Identification

The line identification process is a strong function of the noise level of the spectrum. For my survey, the rms noise level for a given position is $\sim .1$ K. In general, a signal to noise ratio of at least 3 is needed to detect a line. Therefore, the minimum detectable line strength for this survey is .3 K. As noise spikes can have strengths 3σ or greater, additional criteria on the width of the line must be set. The minimum requirements I have defined for a line are :

- Peak signal $> 3\sigma$ rms
- Signal in one adjacent channel $> 2.5\sigma$ rms
- Line profile must be a minimum of 4 channels wide
- The line should pass visual inspection

The line is bounded by the first negative channel to either side of the peak. For the 2756 positions observed (128 channels per position), there should be on the order of one false detection for the entire data set. As over 100 individual molecular clouds have been identified in this data set, the results of this thesis are not significantly affected by a few spurious detections.

The criteria for line identification are easy to combine into an algorithm (which I call the FINDLINE algorithm) to identify lines in spectra. Briefly, one scans through a spectrum until a channel with $T > 3\sigma$ is encountered; adjacent channels are checked to see if they meet the second criteria. Then, the width of the line (in number of channels) is measured by stepping in the positive and negative directions until a channel with a negative value is reached. If the total number of channels is greater than 4, then it is a line candidate. Once again, a computer program can be written to simplify and speed the data reduction process.

2.5.2 Measurement of Line Properties

Once lines have been identified, four major properties of the lines are measured:

- Peak line temperature
- Velocity of line center
- Linewidth – represented as either full width at half maximum (FWHM) or dispersion of line
- Integrated intensity of line

For the majority of lines observed, the line profiles can be well approximated by a single Gaussian. Using the REDUCE package, Gaussian profiles are fit to the data using Marquandt's method. Fits are rejected if the rms noise of the Gaussian fit is more than 4 times the rms noise of the data fit. All fits have been visually inspected and any aberrant fits have been discarded. The four measured properties of the line are taken from the Gaussian fit. For lines with unacceptable fits, the line properties are calculated directly from the spectra by :

$$T_{Peak} = MAX(T(v_{min}), T(v_{max})) \tag{2.6}$$

$$v_{avg} = \frac{\sum_{i=min}^{max} v_i T_i}{\sum_{i=min}^{max} T_i} \tag{2.7}$$

$$\sigma = \frac{\sum_{i=min}^{max} (v_i - v_{avg})^2 T_i}{\sum_{i=min}^{max} T_i} \tag{2.8}$$

$$I = \sum_{i=min}^{max} T_i \, \Delta v \tag{2.9}$$

where σ is the dispersion of the line, Δv is the channel width, I is the integrated intensity and the summations are over the range of channels comprising the line. $MAX(T(a), T(b))$ is a function that returns the maximum value of $T(v)$ between $v = a$ and $v = b$. All functions are evaluated between the minimum, v_{min} and maximum, v_{max} values of the line. As a check of the Gaussian fit routine, the line parameters for fitted lines were also calculated using the above equations and agree to within the error limit of the fit.

2.6 Measurement of Cloud Properties

While it is important to identify and measure individual spectral lines, most of the physical properties of a molecular cloud can only be determined by completely mapping the cloud in appropriate molecular tracers. The steps in determining the physical properties of a molecular cloud are :

- Identification of cloud boundaries
- Conversion of measured line properties to observed cloud properties
- Calculation of physical properties of cloud from observed quantities

Observations of the ^{12}CO (J $= 1 \rightarrow 0$) transition are sufficient to obtain reasonable estimates of the basic physical properties (size, mass, average kinetic temperature) of the clouds. To obtain more detailed information about the density and temperature structure of the cloud, other molecular tracers such as CS (J $= 3 \rightarrow 2$) and CS (J $= 5 \rightarrow 4$) must be considered [Gellert (1995)].

Some guidelines for the physical properties of molecular clouds are :

- Cloud diameters: $2r \sim 1 \rightarrow 50\,\mathrm{pc}$
- Cloud kinetic temperatures: $T_k \sim 5 \rightarrow 50\,\mathrm{K}$
- Cloud masses: $M \sim 10^3 \rightarrow 10^6\,\mathrm{M}_\odot$

The ranges of physical values given above can help distinguish between clouds and complexes of clouds. Typically, any object with a mass greater than $10^6\,\mathrm{M}_\odot$ is probably a complex of GMCs and not one individual cloud. For the smallest clouds, it is unlikely that a cloud will have a radius of less than one parsec, as this is

Table 2.5: Molecular Cloud Substructure Properties

Structure	T_k (K)	n_{H_2} (cm^{-3})	Radius (pc)	Mass ($M_\odot$)
Envelope	~ 10	$10^2 - 10^3$	$10 - 25$	$10^4 - 10^6$
Clump	$10 - 100$	$10^4 - 10^5$	~ 1	10^4
Core	$30 - 100+$	$10^5 - 10^6$	$\lesssim 1$	10^3

approximately the photodissociation length for CO [van Dishoeck & Black (1988)] using typical values for gas density and the interstellar radiation field.

As clouds generally have a lot of internal structure, such as clumps and filaments, it is important to distinguish between substructures in clouds and the actual extent of the cloud. A typical molecular cloud can be divided into three, very general parts: envelope, clumps and cores, as shown in Figure 2.14. The cloud envelope surrounds the other substructures and fills most of the volume of the cloud. The distinction between clump and core is somewhat arbitrary. Clumps have densities in between those of cores and the envelope. Cores are the condensations out of which stars can form. Observing ^{12}CO ($J = 1 \rightarrow 0$) alleviates the problem of distinguishing between cloud and substructure boundaries as the ^{12}CO ($J = 1 \rightarrow 0$) line is optically thick; therefore, the majority of the emission will be coming from the cloud envelope, which encompasses all the substructures within the cloud. Some properties of the substructures of molecular clouds are given in Table 2.5.

2.6.1 Identification of Cloud Boundaries

Determining the boundary of a molecular cloud is more difficult than it would seem as there is no rigorous definition of a cloud boundary. Most astronomers will agree that the boundary of a molecular cloud is where the gas makes the transition from mostly atomic to mostly molecular. This transition occurs in a relatively small region (approximately one parsec is size) in which the effects of shielding the

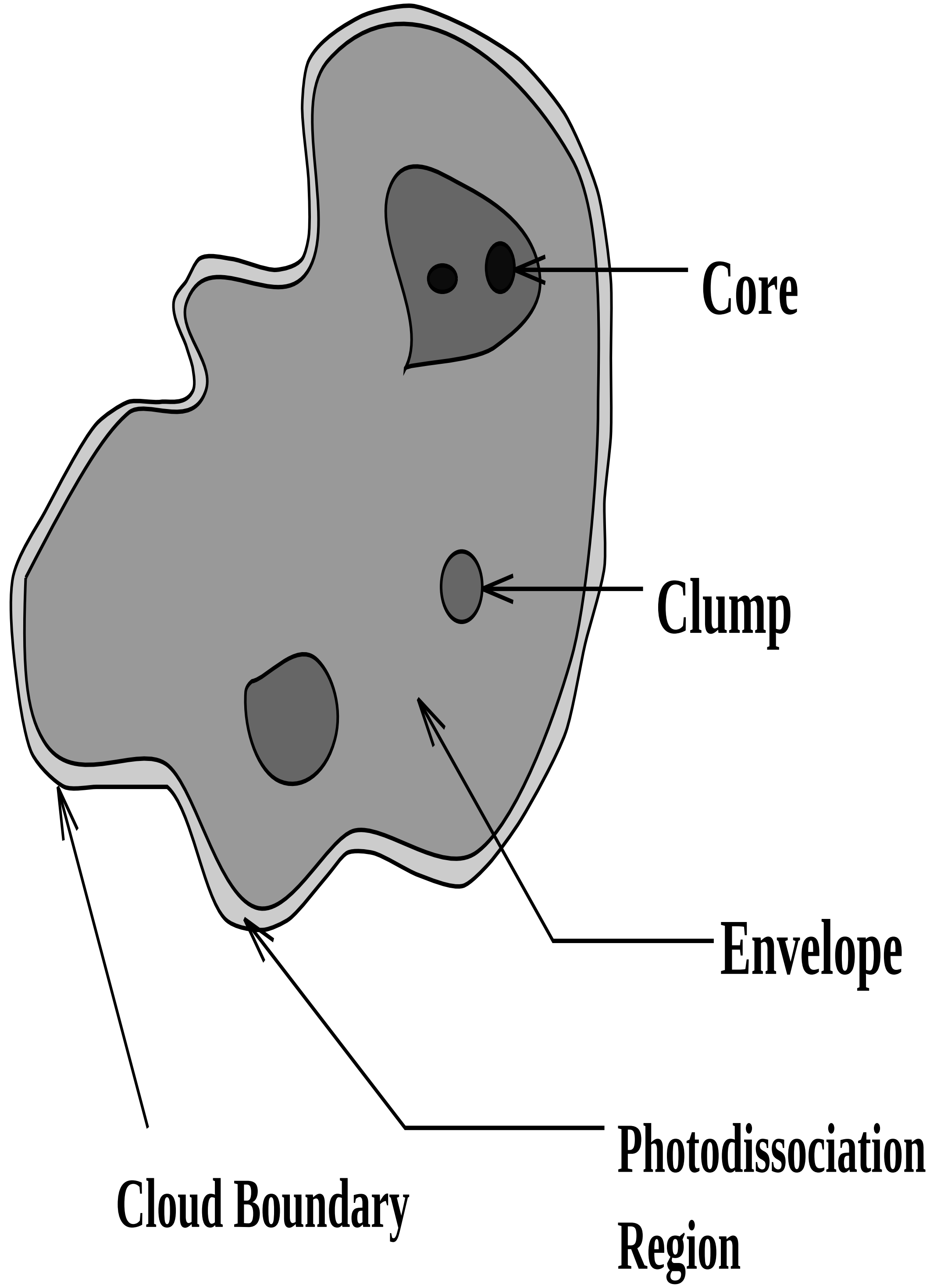

Figure 2.14: A sketch of the major components of a molecular cloud

molecules from UV radiation (which dissociates molecules) become important.

Whether molecular clouds are entities separate from the atomic gas they reside in or not is a currently unanswered question. The most prevalent theory is that the majority of molecular clouds are gravitationally bound objects [see however Maloney (1990)] with reasonably well defined borders. A competing viewpoint is suggested by Elmegreen (1993b) in which the question of whether a cloud is self-gravitating is separated from the chemical nature (atomic/molecular) of the cloud. In Elmegreen's scenario, clouds can be totally molecular without being gravitationally bound. These clouds are held together by external pressure. The converse is also true, clouds can be atomic while being gravitationally bound.

For the clouds investigated in this work, it will be assumed that the clouds are gravitationally bound or sufficiently close enough to this condition so that the approximation of virial equilibrium gives reasonably accurate mass estimates. This assumption is supported by the observations detailed in this chapter. This point will be further discussed in Chapter 4.

An operational definition of a cloud boundary is necessary before measuring cloud properties. Previous work in determining cloud boundaries includes :

- Fitting a three-dimensional Gaussian to the emission peak in l,b,v space and using the FWHM of the fit as the cloud radius [Solomon *et al.* (1987)]
- Calculating the integrated intensity as a function of position and defining a bounding contour (some percentage of the maximum value) as the boundary of the cloud [Digel *et al.* (1990)]

These methods work reasonably well for the largest molecular clouds but have some flaws. Modeling the spatial intensity distribution of a cloud using a Gaussian profile is not an accurate description of the angular intensity distribution for most clouds. Using a contour of integrated intensity is a better means of determining the extent of the cloud; however, it does not ensure that the entire extent of the cloud will be included within the boundary. There is a more accurate way to determine a cloud boundary, provided the observations have sufficient sampling, resolution and sensitivity. As the boundary of a molecular cloud is well defined in the molecule CO, the cloud is clearly delineated by emission lines of ^{12}CO (J $= 1 \rightarrow 0$), which is easily excited. All positions which contain ^{12}CO (J $= 1 \rightarrow 0$) emission at the same velocity and are simply connected in l,b space comprise a single molecular cloud.

For this method to work, the region must be surveyed at full beamwidth or better sampling to ensure accurate coverage of the region in question. Cloud diameters are inaccurate to one sample spacing. The survey resolution must be such that beam dilution effects on small clouds are not significant. If the emission from small clouds is beam diluted, these clouds may not be detected. Additionally, the calculated cloud diameters for beam diluted clouds will be ill defined. If a peak brightness temperature for a beam diluted cloud can be estimated, then the angular area of the cloud can be determined by

$$A_{cloud} = \frac{T_R^*(\mathrm{Observed}) A_{beam}}{T_R^*(\mathrm{Undiluted})} \tag{2.10}$$

where $T_R^*(\mathrm{Undiluted})$ is the estimated brightness temperature, A_{beam} is the angular area of the main beam and $T_R^*(\mathrm{Observed})$ is the actual brightness temperature measured. In general, it is not possible to accurately estimate what $T_R^*(\mathrm{Undiluted})$ is, as the brightness temperature of the source is directly related to the kinetic temperature of the cloud. However, a range of most probable brightness temperatures can be defined which will set the minimum and maximum possible cloud sizes for beam diluted clouds.

My algorithm for finding clouds (CLOUDFIND algorithm) starts with the identification of all the lines in the survey region using the FINDLINES algorithm. The lines are then sorted according to angular position on the sky. Lines that are adjacent to other lines in l, b, v space are grouped together to form a single cloud.

Lines are adjacent in l, b space, if the the positions of the lines differ by no more than one sample spacing in both l and b. For lines to be adjacent in velocity space, the velocities of the line centers needed to be within $5\,\mathrm{kms}^{-1}$ of each other. Once a line is assigned to a cloud, it is removed from the array of unprocessed lines. This step ensures that lines will not belong to multiple clouds. This algorithm is similar to the method Williams *et al.* (1994) used to identify clumps in an individual cloud. Their method differs slightly from my method in that they use intensity contours of twice the rms noise level to identify clumps, instead of identifying lines in the appropriate molecular tracer (which was ^{13}CO ($J = 1 \rightarrow 0$) for their work).

The results of the CLOUDFIND algorithm were checked by hand and needed very little adjustment. One cloud identified by CLOUDFIND was divided into two separate clouds as the line centers in the two separate portions of the clouds were just within the $5\ \mathrm{kms}^{-1}$ inclusion limit and the line profiles were noticeably different in shape and strength between the two regions. Further refinement of the CLOUDFIND algorithm is difficult as the distinction between two clouds crowded together in velocity space and a single cloud with some type of velocity gradient is not easy to quantify. A possible improvement of this algorithm is to employ a neural net trained to distinguish between these cases.

2.6.2 Conversion of Line Properties to Cloud Properties

Once the boundaries of the cloud have been determined, the individual line properties of each position in the cloud are used to determine the size, centroid and total emission from the cloud. The area of the cloud (A), effective cloud radius (r), integrated intensity (I), cloud centroid (l_0, b_0) and CO luminosity (L_{CO}) are calculated by

$$A = N(\theta d)^2 \tag{2.11}$$

$$r = \sqrt{\frac{A}{\pi}} \tag{2.12}$$

$$I = \sum_{i=1}^{N} I_i \tag{2.13}$$

$$\langle I \rangle = \frac{I}{N} \tag{2.14}$$

$$l_0 = \frac{1}{I} \sum_{i=1}^{N} l_i I_i \tag{2.15}$$

$$b_0 = \frac{1}{I} \sum_{i=1}^{N} b_i I_i \tag{2.16}$$

$$L_{\mathrm{CO}} = \langle I \rangle A \tag{2.17}$$

where N is the number of positions in the cloud, θ is the angular separation between adjacent positions, d is the kinematic distance to the cloud, I_i is the intensity at position i in the cloud, $\langle I \rangle$ is the average CO intensity of the cloud and l_i, b_i are the coordinates of each position.

2.6.3 Calculation of Cloud Physical Properties from Observed Quantities

The three physical quantities of the cloud that can be reasonably estimated from observations of the ^{12}CO (J $= 1 \rightarrow 0$) line are the cloud size, mass and kinetic temperature. These quantities are determined using assumptions that are plausible about the excitation of CO in the physical conditions of a molecular cloud ($n_{\mathrm{H}_2} \sim 10^2 - 10^4$ cm^{-3} and $T_K \sim 5 - 100$ K). As the ^{12}CO (J $= 1 \rightarrow 0$) line is optically thick for all molecular clouds, it is an unambiguous tracer of the extent of molecular material. The angular area encompassed by a molecular cloud is simply the number of positions observed multiplied by the spacing between positions (for full beamwidth sampling). The effective radius of the cloud (in parsecs) is given by

$$r = \sqrt{\frac{A}{\pi}} = \sqrt{\frac{N(\theta d)^2}{\pi}} = \theta d \sqrt{\frac{N}{\pi}} = 0.164 \left(\frac{d}{1\ \mathrm{kpc}}\right) \sqrt{N} \tag{2.18}$$

where d is the distance to the cloud, θ is the sampling spacing, and N is number of positions that the cloud is observed at. The uncertainty in the radius of any cloud is the linear size (2-4 parsecs) of the sample spacing at the distance of the cloud.

For clouds detected in only one beam, the cloud radii are uncertain by a factor of two. As it is most likely that a small cloud will not be centered on any given observation point, the measured radius should underestimate the actual radius of the cloud. Small clouds will not be identified in adjacent positions as they will fill only the periphery of the beam patterns of the adjacent positions; therefore, the measured line temperatures will be below the detection threshold. It is possible that clouds observed in one position are smaller than the beamsize. These clouds must have large undiluted line temperatures to be detected if they fill only a fraction of the beam. It is unlikely that a cloud, which is only marginally larger than the photodissociation lengthscale, will be intrinsically bright in ^{12}CO (J $= 1 \rightarrow 0$).

2.6.4 Kinetic Temperatures

The kinetic temperature of the cloud is determined from the average peak line temperature of the cloud. The peak line temperature is in units of T_R^* and must be converted to the brightness temperature of the source before the kinetic temperature can be determined. The brightness temperature, T_R is given by

$$T_R = \frac{T_R^*}{\eta_c} \tag{2.19}$$

where η_c is the source coupling efficiency and is equal to the corrected main beam efficiency of the telescope if the source fills the beam ($\eta_c = \eta_M^* = .86$). For sources that do not fill the beam,

$$\eta_c \approx \eta_M^* \left(\frac{\theta_{source}}{\theta_{beam}}\right)^2 \tag{2.20}$$

The excitation temperature (T_x) of the transition is given by solving the equation of radiation transfer

$$T_R = \frac{h\nu}{k}\left(\frac{1}{e^{(h\nu/kT_x)}-1} - \frac{1}{e^{(h\nu/kT_{BG})}-1}\right)(1-e^{\tau}) \tag{2.21}$$

where τ is the optical depth of the line and T_{BG} is the background temperature. As the cosmic background radiation is the only significant source of background radiation at millimeter wavelengths, $T_{BG} = 2.7\,\mathrm{K}$. As the ^{12}CO (J $= 1 \rightarrow 0$) line is optically thick ($\tau \gg 1$) for all molecular clouds, the excitation temperature is

$$T_x = \frac{h\nu}{k} \frac{1}{\ln\left[1 + \frac{1}{(kT_R/h\nu) + 1/(e^{h\nu/kT_{BG}} - 1)}\right]} \tag{2.22}$$

CO can be radiatively or collisionally excited (de-excited). As a result of the competition between radiative and collisional processes, the excitation temperature can be written as

$$T_x = \left(\frac{1}{1+x}\right) T_r + \left(\frac{x}{1+x}\right) T_K \tag{2.23}$$

where T_r is the effective temperature of the radiation field, T_K is the gas kinetic temperature and x is the ratio of the collisional de-excitation rate to the radiative de-excitation rate. This equation for T_x is rigorously correct for a two-level system and is a reasonable approximation for CO, although CO is significantly populated in the first five rotational levels at the temperature and densities of molecular clouds. If the trapping of line photons due to a high optical depth of material is not considered, then x is

$$x = \left(\frac{h\nu}{kT_k}\right) \frac{C_{10}}{A_{10}} \tag{2.24}$$

where C_{10} is the collisional de-excitation rate. For CO, collisions with H_2 molecules are the primary means of collisional de-excitation; therefore, C_{10} is

$$C_{10} = n_{H_2} \langle \sigma v \rangle = 2.2 \times 10^{-13} \left(\frac{T_K}{1\,K}\right)^{1/2} \left(\frac{n_{H_2}}{100\,cm^{-3}}\right) \tag{2.25}$$

For most molecular clouds (including all the clouds in my survey), the ^{12}CO (J $= 1 \rightarrow 0$) line is optically thick. Observations of a select sample of the survey clouds in the ^{13}CO (J $= 1 \rightarrow 0$) transition support this claim. The measured ^{13}CO (J $= 1 \rightarrow 0$) line strengths are approximately 25% of the ^{12}CO (J $= 1 \rightarrow 0$) line strengths reported in this work. As the abundance ratio of ^{12}CO to ^{13}CO is > 30 in the ISM [Jura (1987)], the optical depth of the ^{12}CO (J $= 1 \rightarrow 0$) line must be greater than one. Therefore, the trapping of photons due to optical depth effects must be considered. The trapping of photons effectively increases the lifetime of the $J = 1$ state with respect to radiative de-excitation. The spontaneous emission coefficient is effectively reduced by a factor equal to the escape probability of the photons. In the limit of high optical depth, the photon escape probability (β) is given by

$$\beta \approx \frac{1}{\tau} \tag{2.26}$$

then x is given by

$$x = \frac{h\nu}{kT_K}\frac{C_{10}}{A_{10}\beta} = 2 \times 10^{-5}\sqrt{\left(\frac{1\,K}{T_K}\right)}\left(\frac{n_{H_2}}{100\,cm^{-3}}\right)\tau \tag{2.27}$$

For typical molecular cloud densities and optical depths, $x \gg 1$ and $T_x \approx T_K$. Another way of describing this condition is to say that the ^{12}CO (J = 1 → 0) transition is thermalized. If the assumption of high optical depth ($\tau \sim 10$) and moderate density is incorrect, the excitation temperature of the cloud will be less than the kinetic temperature of the cloud. For the case of a sub-thermally excited cloud, the ^{12}CO (J = 1 → 0) line temperature will underestimate the cloud kinetic temperature.

I assume that any cloud which is observed in five or more adjacent positions completely fills the beam in the center position. With this assumption, $\eta_c = 0.86$. My approximation is slightly naive, as most of the emission from the cloud may come from clumps, and I have no way of determining the clump filling factor of the clouds from these observations. Observations of ^{13}CO (J = 1 → 0), ^{12}CO (J = 2 → 1), CS (J = 3 → 2), and CS (J = 5 → 4) have been conducted for a select sample of the survey clouds. Analysis of these observations will help determine the internal structure of the clouds and provide enough data for modeling of the cloud temperatures and densities using LVG analysis [Goldreich & Kwan (1974)] and possibly a micro-turbulent radiative transfer model [Leung (1975)].

For clouds which are smaller than 5 beams, the ^{12}CO (J = 1 → 0) line temperature will again underestimate the kinetic temperature of the cloud. The error in the derived kinetic temperature cannot be calculated for any given measurement as there is no way to predict what the filling factor or excitation of a cloud is. My best estimate of the smallest fraction of a beam that is filled by a cloud such that the cloud is still detected is $\frac{1}{2}$ (see Section 2.7). The excitation temperature is probably no less than one half the kinetic temperature. The worst possible estimate of the kinetic temperature is $\sim 25\%$ of the actual value. For undiluted T_R^*'s, the uncertainty is due to the inaccuracy of the models and the failure to adequately account for the effects of line trapping. For diluted T_R^*'s, the major contribution to the uncertainty in kinetic temperature is the amount that the emission is beam diluted.

2.6.5 Cloud Masses

There are two ways to determine the cloud mass from ^{12}CO $(\mathrm{J} = 1 \rightarrow 0)$ observations: assuming virial equilibrium and using an empirical relationship between CO luminosity and cloud mass. Both methods have difficulties, the virial approximation may not be valid for some molecular clouds and the relationship between CO luminosity and cloud mass varies as a function of cloud environment.

The empirical relationship between CO luminosity and cloud mass is

$$M_{CO} = 2.1X \frac{\langle I \rangle}{\mathrm{K\ kms^{-1}}} \frac{\pi r^2}{\mathrm{pc}^2}\ \mathrm{M}_{\odot} \tag{2.28}$$

where

$$X = \left(\frac{1}{1 \times 10^{20}}\right) \frac{N_{\mathrm{H_2}}/1\ \mathrm{cm}^{-3}}{I_{\mathrm{CO}}/1\ K\ \mathrm{kms}^{-1}} \tag{2.29}$$

and $\langle I \rangle$ is the average integrated intensity of the cloud, r is the radius of the cloud and X is the empirically determined ratio between the molecular hydrogen column density and integrated intensity. The numerical constant 2.1 contains the necessary unit conversions and a correction factor to account for the mass of helium in the cloud [Kutner (1987)]. Without the helium correction factor, the constant is 1.7. Mead & Kutner (1988) use $X = 4.0$ for outer Galaxy clouds. I will also adopt this

Table 2.6: Values of X

Author	X	Comments
Bloemen *et al.* (1986)	2.8	Gamma Ray calibration
Cohen *et al.* (1988)	17	Large Magellanic Cloud
Digel *et al.* (1990)	9.2	Outer Galaxy
Grabelsky *et al.* (1989)	2.8	Carina Arm
Mead & Kutner	4.0	Outer Galaxy
Mizuno (1995)	2.0	M31
Rubio *et al.* (1991)	60	Small Magellanic Cloud
Scoville *et al.* (1987)	3.6	Inner Galaxy

value, as my clouds are similar in temperature and environment to theirs. Other authors' values of X are listed in Table 2.6.

As ^{12}CO (J $= 1 \rightarrow 0$) is an optically thick transition, it is surprising that its total luminosity can be used as a tracer of cloud mass. For optically thick material, emission is observed from an optical depth of around one into the cloud. Therefore, it is improbable that ^{12}CO (J $= 1 \rightarrow 0$) could be used as a tracer of total cloud mass. However, several authors have calculated X factors using independent measures of cloud masses. Dickman (1978) used ^{13}CO (J $= 1 \rightarrow 0$) observations (which are optically thin) to determine H_2 column densities. Bloemen *et al.* (1986) used cosmic ray observations from the COS-B satellite to determine the X factor. As the COS-B observations have low angular resolution ($\sim 2.3^\circ$ FWHM) [Lebrun *et al.* (1983)], Bloemen's value of X is an average value for the Galaxy.

While this conversion factor may be a good tracer of mass for an ensemble of clouds, the efficacy of this approach for an individual cloud is questionable. It is evident from Table 2.6, that X varies as a function of cloud environment. X should be a strong function of the cloud's metallicity as the ratio of metals to H_2 will strongly influence the $N(H_2)$ to I_{CO} ratio. The X factors for the metal poor Magellanic Clouds support this claim [Cohen *et al.* (1988) and Rubio *et al.* (1991)]. In addition, X is a function of kinetic temperature, $X \propto T^{-1.3}$ [Kutner & Leung (1985)].

A second method of determining cloud mass is to assume that the cloud is in virial equilibrium. In virial equilibrium for a gravitational potential,

$$\langle U \rangle = -2\langle T \rangle \tag{2.30}$$

where $\langle U \rangle$ is the average gravitational potential energy and $\langle T \rangle$ is the average kinetic energy. Writing this equation in a more useful form for molecular clouds,

$$M = \frac{\langle \sigma^2 \rangle R}{G} \left(\frac{2\alpha + 5}{\alpha + 3} \right) \tag{2.31}$$

where I have assumed that the cloud is spherically symmetric, M is the mass of the cloud, σ is the 3 dimensional velocity dispersion of the gas in the cloud, R the radius of the cloud and α is the power-law exponent for the mass density distribution,

$$\rho(r) = \rho_0 r^{\alpha}, r \leq R \tag{2.32}$$

I assume that the density distribution is uniform, $\alpha = 0$. This is a reasonable approximation for giant molecular clouds as their clumps and cores are not centrally located. Also, most of the mass of a GMC is in the cloud envelope. Other popular choices for α are $\alpha = -2$ (isothermal sphere) and $\alpha = -1$ (density law profile needed for size-linewidth relation, $\sigma = r^{.5}$). These choices for α are more appropriate for clumps and cores in clouds. Using a different density profile will reduce the mass calculated by up to 40%. Modeling the cloud as an ellipsoid will also change the derived mass by a factor of order unity [see Binney & Tremaine (1987), Chapter 2, for a more detailed treatment].

The assumption of virial equilibrium implies that the cloud is gravitationally bound and that enough time has elapsed for the cloud to reach equilibrium. This should be several crossing times of an Alfvén wave for a molecular cloud.

$$t \sim 5\frac{r}{v_A} \tag{2.33}$$

where r is the radius of the cloud, and v_A is the Alfvén velocity or the speed that information can be propagated in a magnetic medium. The Alfvén speed is equal to $\sqrt{4\pi\rho}/B$ where ρ is the mass density of the cloud and B is the magnetic field strength [Lang (1986)]. For molecular clouds, the Alfvén speed is on the order of the linewidth of the cloud; that is about 1 km/s. For a molecular cloud with a radius of 5 parsecs, the time to reach virial equilibrium is on the order of 5×10^6 years.

As spiral arm passages are a proposed method of cloud disruption, current estimates for lifetimes of GMCs are in the tens of millions of years, which is the timescale for a spiral arm passage; therefore, most clouds have sufficient time to become virialized. Several authors [see for instance, Maloney (1988) and Leisawitz (1985)] have questioned whether virial equilibrium is a good approximation for molecular clouds, since there are many events in the ISM such as star formation and supernova which can disturb a molecular cloud. While these processes certainly affect a cloud, the virial approximation should be good to within a factor of 2 for clouds that are not totally disrupted.

Another class of clouds, which are not thought to be virialized or even gravitationally bound, are the diffuse high-latitude clouds identified by Blitz *et al.* (1984). They determined that these clouds were not gravitationally bound by comparing the mass calculated from the optically thin tracer, ^{13}CO (J $= 1 \rightarrow 0$), to the virial estimate. The point of whether the small clouds identified in this survey are like the high-latitude clouds will be discussed in Section 4.3.2.

Despite all the assumptions and uncertainties inherent to the virial approximation, it is a better approximation than deriving masses directly from the CO luminosity of a cloud, because the scaling factor between CO intensity and H_2 column density is a strong function of cloud environment. The virial approximation also has a stronger theoretical basis. As long as a cloud is gravitationally bound, the virial estimate will be within a factor of two of the actual mass. The two methods of estimating mass give upper and lower limits to the mass of a cloud. The virial mass will always overestimate the mass of the cloud (if the cloud is not virialized, it will have more kinetic energy than assumed and a lower mass). As the X factors previously used for molecular clouds in the Galaxy are too low for the clouds in my survey, the mass estimate from the CO luminosity will be a lower limit to the mass of the cloud.

Using appropriate units, the mass of a cloud using the virial approximation is

$$M_{VIR} = 1.2 \times 10^3 \left(\frac{r}{1 \text{ pc}}\right) \left(\frac{\sigma_{LSR}}{1 \text{ kms}^{-1}}\right)^2 \text{ M}_\odot \tag{2.34}$$

where r is the cloud radius and σ_{LSR} is the line-of-sight velocity dispersion, which is approximated by the dispersion of the ^{12}CO (J $= 1 \rightarrow 0$) line. As the virial mass is determined from gravitational considerations, it contains all the mass in the cloud; therefore, no correction for the mass of helium in the cloud needs to be made.

2.7 Completeness Limits of Survey

The observations used in this thesis cover Galactocentric radii between 9.6 and 16 kpc. At R = 16 kpc, the heliocentric distance is 15.7 kpc and the spacing between beam centers is 4.6 parsecs. As the main beam of the telescope is Gaussian in profile, a cloud should probably intersect the center of the beam to be detected. Using a minimum undiluted beam temperature of .6 K (the minimum peak temperature for a resolved cloud, see Table 4.8), a cloud will be detected if it fills approximately half the beam, as the observed line temperature will be above the detection threshold. Smaller clouds can be detected if the beam is centered exactly on the cloud. Clouds with larger peak temperatures will be more easily detected. If the brightness temperature of the cloud is not uniform across the cloud, this will further complicate the analysis.

As it is impossible to know the size and brightness temperature distribution of a cloud that is detected in one beam, I make a reasonable assumption about detected clouds. For a cloud to be detected at a given position, it must fill approximately one-half the beam (more explicitly, if the cloud fills the center of the beam, then it will be detected).

With this cautious assumption, the maximum cloud size that has a chance of not being detected is 85" in angular extent. This size corresponds to a circular cloud in cross section which is centered equidistant from four adjacent beam centers. The largest possible cloud that will not be detected is 3.25 parsecs in radius. The highest cloud brightness temperature, which will not be detected for clouds of this size or larger, is .6 K. This temperature corresponds to a kinetic temperature of 4.7 K using the approximations of Section 2.6.4. Therefore, this survey is complete for all clouds in the region with radii greater than 3 parsecs and kinetic temperatures greater than 4.7 K.

CHAPTER 3
THE 13 KILOPARSEC ARM

As stated in the introduction, a major goal of this work is to examine the properties of the molecular cloud population in the 13 kpc (Outer) arm. The arm was first identified in molecular material by Mead (1986) as shown in Figure 3.1. In addition, the arm is apparent as an enhancement in the HI surface density [Henderson *et al.* (1982)].

My work examines a small segment of the arm approximately 750 pc long. Two goals of this project are to determine the ratio of molecular emission between the arm and interarm regions and to investigate the cloud size distribution of the arm and interarm regions. This portion of the project can be divided into four main steps :

- Confirmation of 13 kpc arm
- Measurement of arm properties
- Determination of arm and interarm cloud populations
- Investigation of the physical properties of the cloud populations and mass distribution

It is well known that GMCs trace spiral arms [Vogel *et al.* (1990)]; therefore, an enhancement in molecular emission is a clear signature of a spiral arm. As an example, Grabelsky *et al.* (1987) calculated an arm/interarm contrast ratio of 13 for the Carina arm.

While Mead's survey indicates the presence of the 13 kpc arm, it is severely undersampled. As a result, estimates of the arm centroid and width cannot be made. The work of May *et al.* (1988) also shows an arm feature at R = 13 kpc in

Figure 3.1: Plot of molecular clouds distributed on the Galactic Plane from Mead (1988).

the second quadrant. The survey of Wouterloot *et al.* (1988) in the 2nd quadrant shows a small enhancement at $R \approx 13\,\mathrm{kpc}$ in the distribution of molecular emission believed to be associated with IRAS point sources. The 1st quadrant arm appears to be a continuation of the 13 kpc arm seen in the 2nd quadrant, but no observations trace the arm from the 1st to 2nd quadrants.

The observations of the Cygnus X region ($l = 75 - 85°$) by Leung and Thaddeus (1992) do not reveal a 13 kpc arm feature. However, their beam size (8.8 arcminutes) and sensitivity level ($\Delta T_R^* = 0.1\,\mathrm{kms}^{-1}$) are inadequate to detect the molecular emission present. The large distance to the 13 kpc arm, d = 12 kpc, and their large beam significantly dilute the emission of all but the largest molecular clouds. The smallest clouds that will entirely fill their beam have radii of 16 parsecs.

In the published work of Leung and Thaddeus, only two emission features are detected in the limits of my survey region as shown in Figure 3.2. Figure 3.3 is a plot of the total emission in the survey region degraded to the resolution of Leung and Thaddeus and plotted using the same integrated intensity contours. Their feature at $l \approx 76.2°$, $b \approx 1.0°$ has no counterpart in my work and is due to emission just outside the survey region. Followup observations to the initial survey indicate that a large region of molecular emission (one or more giant molecular clouds) exists at the edge of the survey region. The second emission feature at $l \approx 76.0°$, $b \approx 1.7°$ has a corresponding feature in my data. Two other features should be detected by Leung and Thaddeus at the same level, but they are not. One strong feature in particular, the feature at $l \approx 76.7°$, $b \approx 1.7°$, is not present in their data. The absence of this feature cannot be explained by beam dilution, but may be due to the smoothing feature employed in producing their maps. As the CfA (formerly Columbia) telescope was also used by Digel (1990), his survey is similarly hampered by beam dilution.

Unlike work with larger telescope beams, my work is sensitive enough to detect the emission coming from cold and/or small clouds in the arm. This survey provides an unbiased sample of material in the arm. The tradeoff for this sensitivity is the lack of spatial coverage necessary to determine global properties of the arm such as the pitch angle.

3.1 Arm Identification

The strong molecular emission characteristic of a spiral arm is clearly shown in Figure 3.4. Emission at constant R will be at single velocity for small arcs. As a spiral arm will be centered around a particular Galactocentric radius over distances of < 1 kpc along the arm, the 13 kpc arm is identified by a band of emission oriented vertically in the l-v diagram. Most of the emission observed is contained within the velocity range -80 to -50 kms^{-1}. Using kinematic information to calculate distances as described in Chapter 2, the Galactocentric radii encompassed by this emission are 11.1 to 13.6 kpc. Within the large uncertainties of calculating distances kinematically, this emission is centered around 13 kpc and corresponds to the spiral arm feature identified by Mead.

To differentiate between arm and interarm cloud populations, it is necessary to identify the limits of the arm. I have modeled the arm with a Gaussian function to facilitate assignment of the centroid and width of the arm. Visual inspection of the distribution of clouds as a function of R suggests that a Gaussian function is an appropriate model to the distribution. There is no physical reason that the molecular arm should be modeled by a Gaussian (or other simple function); however, a Gaussian is a rigorous way of measuring the basic arm parameters, arm center and width.

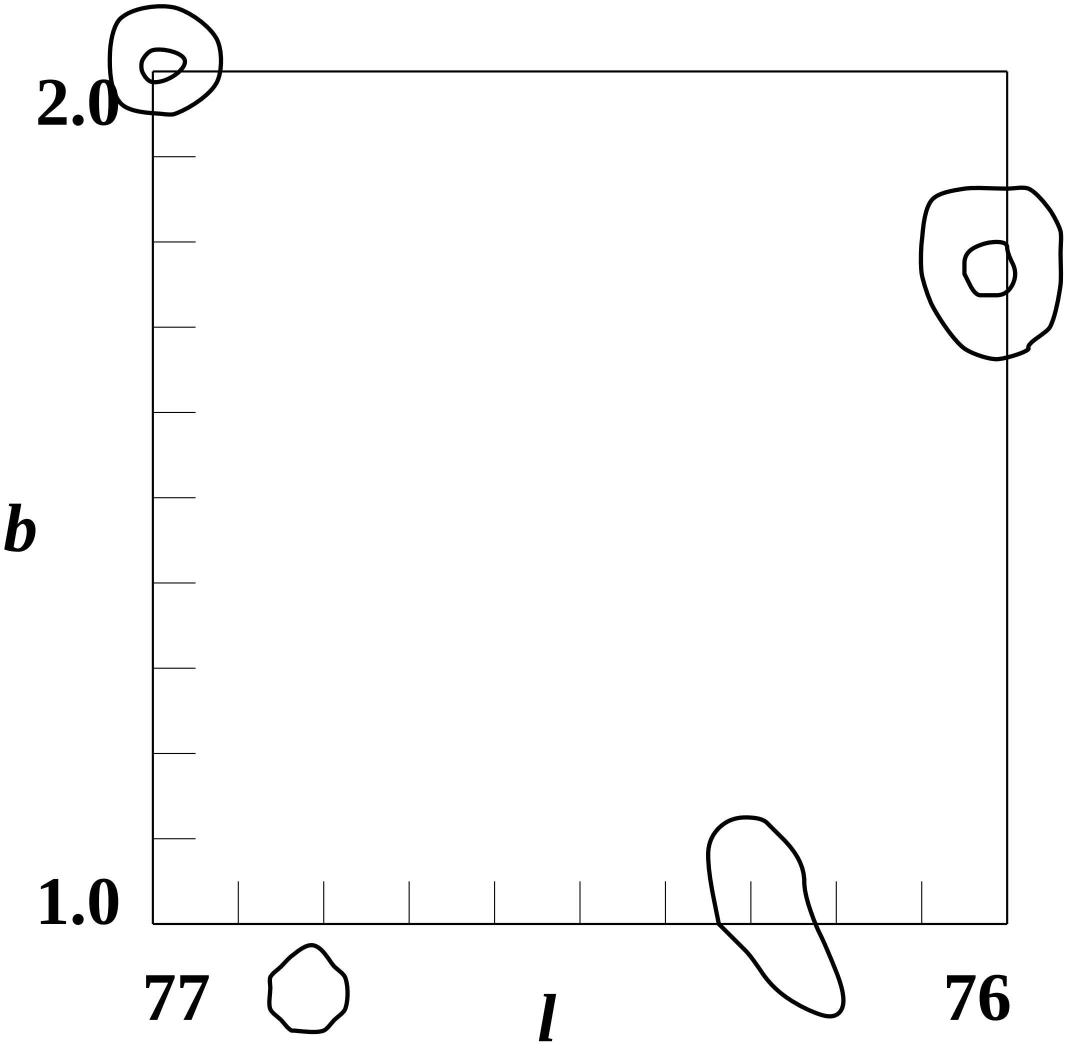

Figure 3.2: Integrated intensity over the velocity range $-55\,\mathrm{kms}^{-1} > v > -90\,\mathrm{kms}^{-1}$ adapted from Leung and Thaddeus (1992). The lowest contour level is at $3.16\,\mathrm{Kkms}^{-1}$.

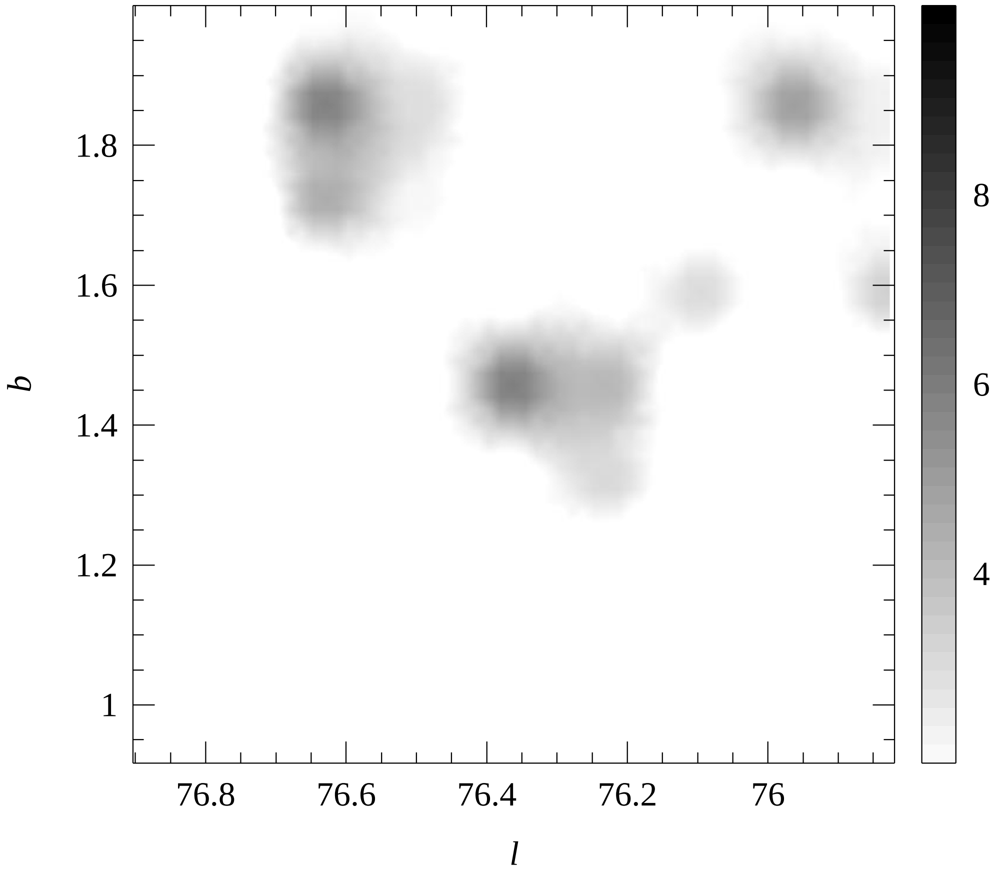

Figure 3.3: **Simulation of integrated intensity over the velocity range $-55\ \mathrm{kms}^{-1} > v > -90\ \mathrm{kms}^{-1}$ from current work. The data has been convolved with an 8.8' Gaussian beam to simulate the observations of Leung and Thaddeus (1992).**

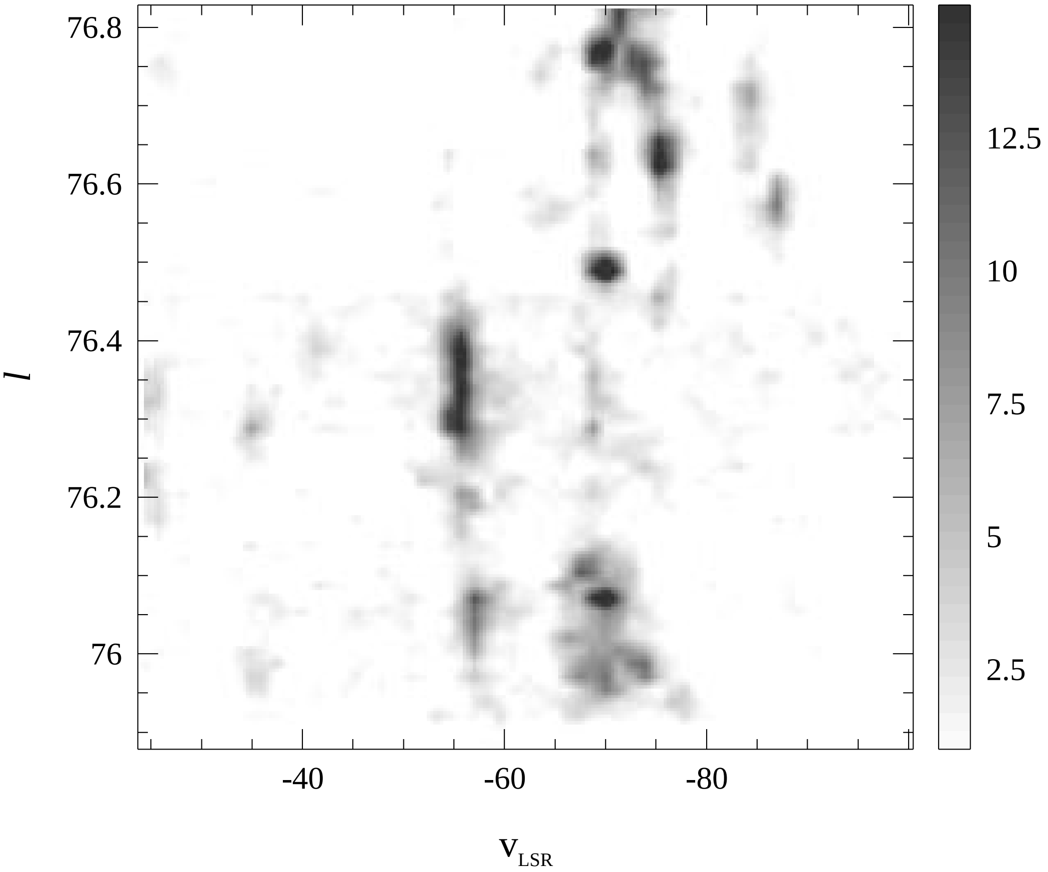

Figure 3.4: A longitude-velocity plot of integrated intensity for the survey region summed over all b. The gray levels range from 1 to $15\,\mathrm{K\,kms^{-1}\,{}^\circ}$.

3.1.1 Model of the 13 kpc arm

This section describes the particulars of the modeling process for the 13 kpc arm. The width of the arm is defined to be the full width at half maximum of the modeled Gaussian. All of the data in the survey is combined into a composite spectrum (see Figure 3.5). Galactocentric radii are calculated from the center velocities of each channel. The data is binned as a function of Galactocentric radius subject to two constraints: the bin size minimizes the mean integrated square error (MISE) [Vio *et al.* (1994)] and is greater than the largest uncertainty in R (δR) from calculating distances kinematically. As described in chapter 2, $\delta \mathrm{R} \approx .8$ kpc. MISE is determined by

$$MISE(N_B) = \frac{N_B}{NL}\,[1 - \frac{N+1}{N-1}\,(\sum_{i=1}^{N_B} \frac{N_i^2}{N} - 1)], \tag{3.1}$$

where N is the number of data points, $\mathrm{N_B}$ is the number of bins in the histogram, L is the bin size and $\mathrm{N_i}$ is the number of data points in the ith bin. As shown in Figure 3.6, the MISE is a increasing but noisy function of bin size; therefore, the bin size is only limited by the uncertainty in R. The most appropriate bin size is .8 kpc, which is the maximum uncertainty in R for the observations. Another factor to consider in binning data is the placement of the bin centers. Four different center positions were used, each shifted by .25 of the bin width. As shown in Figure 3.7, the results are reasonably insensitive to the placement of the bin centers.

To investigate the effect of noise, the data was modeled using all the data and data clipped at the 3σ level. The arm centroid and FWHM calculated do not depend strongly on whether clipping is used or not. Before the arm population can be modeled, the underlying (interarm) distribution must be subtracted. Two methods of background subtraction were employed: an average was subtracted and a first-order baseline was removed.

Forty-eight separate choices of modeling parameters were used. For some of the models, the data was clipped at the 3σ level before making the composite

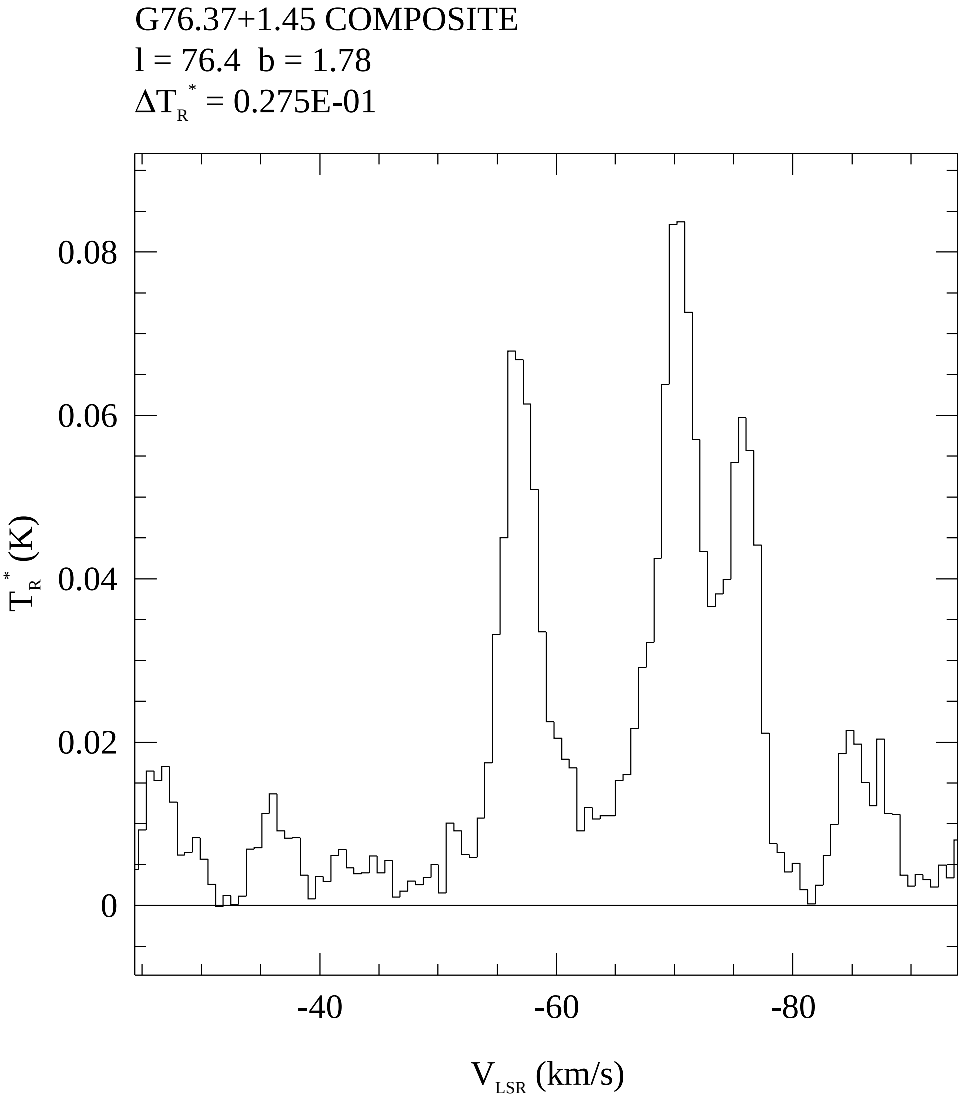

Figure 3.5: Composite spectrum of all data in survey

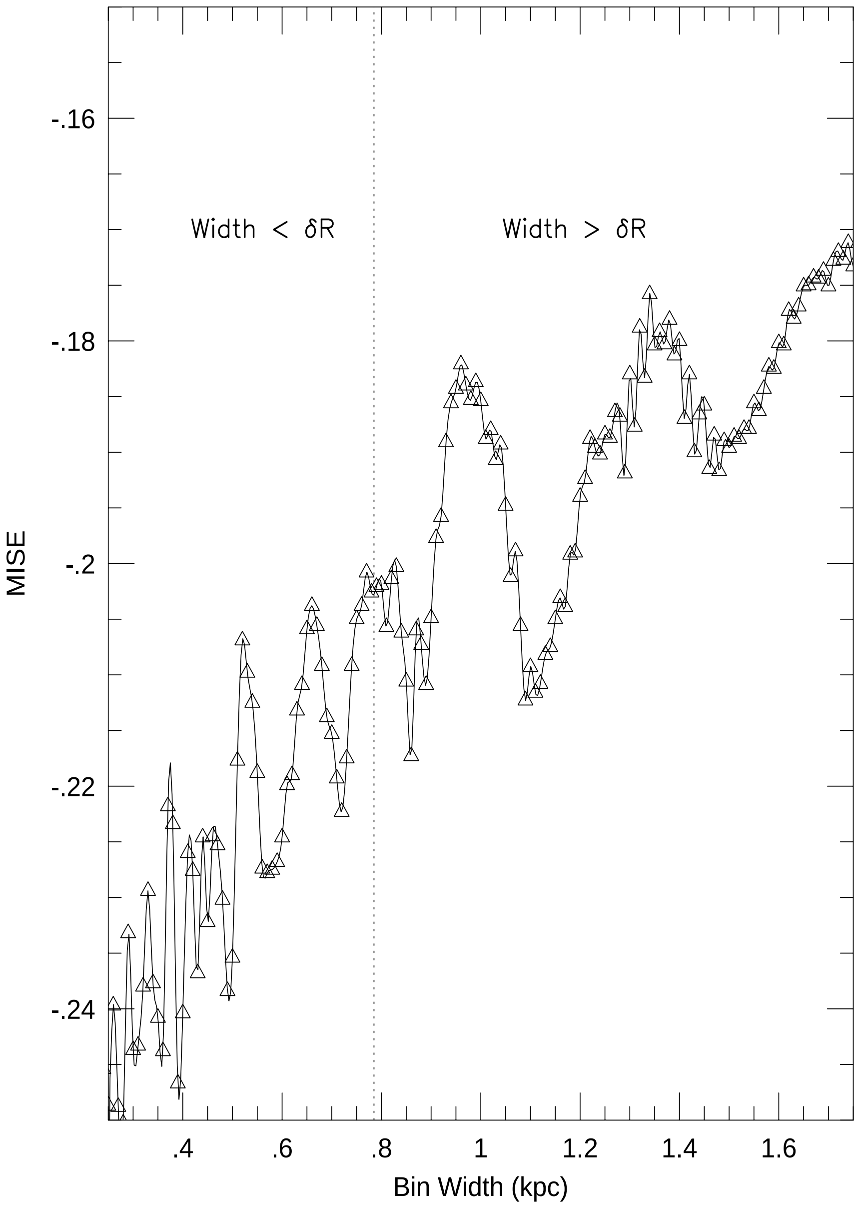

Figure 3.6: Plot of MISE as a function of bin width (δR). The dotted line is at $\Delta R = .8\,\mathrm{kpc}$, the smallest appropriate bin width.

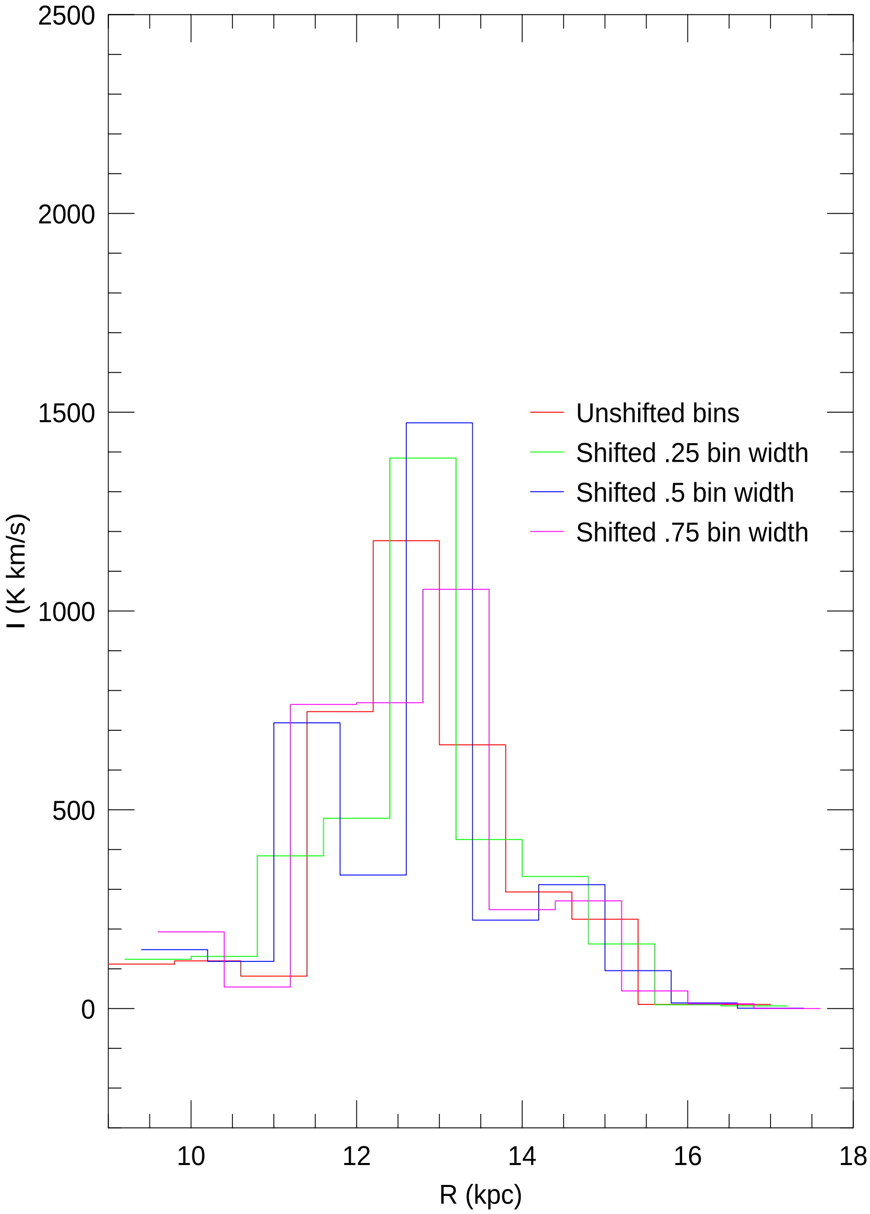

Figure 3.7: Intensity binned with most physical bin size

spectrum and re-binning. The models using the clipped data are designated **bclip** models, the unclipped models are designated **b** models. Four groups of bin centers were used, designated by **b_** (**bclip_**), **b25_** (**bclip25_**), **b50_** (**bclip50_**) and **b75_** (**bclip75_**), respectively. These designations refer to the initial choice of bin centers (**b**), bin centers shifted by 25% of bin width (**b25_**), shifted 50% (**b_50**) and 75% (**b_75**). Subtraction of the interarm background was handled three different ways:

- No subtraction was performed
- The background was averaged over $9\,\mathrm{kpc} < \mathrm{R} < 12\,\mathrm{kpc}$ and $14\,\mathrm{kpc} < \mathrm{R} < 16.5\,\mathrm{kpc}$ and then subtracted
- A linear baseline was removed from the composite spectrum using the regions, $9\,\mathrm{kpc} < \mathrm{R} < 12\,\mathrm{kpc}$ and $14\,\mathrm{kpc} < \mathrm{R} < 16.5\,\mathrm{kpc}$, to determine the fit

The average background subtracted models are designated by **_averaged**, and the models with a linear baseline subtracted are designated by **_based**. Each combination of bin center, clipping and background subtraction had a Gaussian feature fit to the observed peak by two slightly different fitting routines. Both fitting methods use Marquandt's method as implemented in REDUCE for doing the least squares fit. The **_2nd** routine uses a slightly different method of finding the initial parameters for the Gaussian fit.

3.2 Arm Properties

The results of all models are shown in Tables 3.2 and 3.3. The centroid is as expected for the 13 kiloparsec arm, but the FWHM of the arm is larger than that calculated for the Carina Arm [Grabelsky *et al.* (1987)] and the arms in M51 [Vogel *et al.* (1990)]. Table 3.1 lists the widths of other spiral arms in the Milky Way and external galaxies. The discrepancy, between the width calculated in this work and measurements of other arms, is probably due to two factors: poor counting

Table 3.1: Arm Properties for Various Spiral Arms

Galaxy	Arm Name	Arm Width	Reference
Milky Way	13 kpc Arm	1.3 kpc	This Work
Milky Way	Carina Arm	160-210 pc	Grabelsky *et al.*(1987)
Milky Way	Sagittarius Arm	750 pc	Peters & Bash (1987)
M51		300 pc	Vogel *et al.*(1990)
M31		1-2 kpc	Ryden & Stark (1986)

statistics and higher sensitivity. As my work only encompasses a small fraction of the arm feature, it is quite likely that the large width of the arm is due to the random motions of the clouds. A larger data set would reduce the uncertainty by $\sqrt{\mathrm{N}}$, where N is the number of clouds in the data set. More data would also permit modeling of possible streaming motions in the arm. As mentioned in Chapter 2, streaming motions can introduce non-circular velocities on the order of $10\,\mathrm{kms}^{-1}$ and may not affect all clouds equally, which would fragment the arm in velocity space. In addition, as this survey is more sensitive, weak emission at the edge of the arm will be detected which will increase the width of the arm. The measured width of the arm may be enhanced by inclusion of small interarm clouds in the fit.

The arm properties are determined by a residual weighted average of all models, where a Gaussian was a good fit to the intensity distribution. Fits failed for a variety of reasons: failure to converge from initial conditions, super-broad wings (due to emission in interarm region) and poor fits due to the limited number of data bins available. For the FWHM of the arm only the unclipped data were used, as the models of the clipped data were much too wide. The large width of the arm in the clipped data is a result of interarm emission being included into the wings of the fit.

As determined by visual inspection of the various models, the arm population is defined to be all clouds between R = 12.0 kpc and R = 13.3 kpc. The interarm population consists of all clouds at other Galactocentric radii. The centroid of the arm is at 12.66 ± 0.14 kpc. The FWHM of the arm is 1.28 ± 0.56 kpc. The uncertainties quoted are the statistical uncertainties associated with the fits. Taking streaming motions into account, both the centroid and FWHM of the arm are uncertain to approximately a bin width (.8 kpc). While slightly larger than estimates of other arm widths, this width is certainly reasonable for a local measurement of the arm. The ratio of total luminosities of arm clouds to interarm clouds is 1.9. This ratio is significantly lower than the contrast of 13 to 1 measured for the Carina arm; however, it is comparable to the 2 to 1 ratios observed for the Centaurus and Norma spiral arms [Grabelsky *et al.* (1987)].

One interesting feature which is readily apparent in the l-v diagram is the double-edged appearance of the arm. The two bands, one centered at $v \approx -55\ \mathrm{kms}^{-1}$ (R $\sim$ 11.5 kpc) and the other at $v = -70\ \mathrm{kms}^{-1}$ (R $\sim$ 12.6 kpc) are probably not two distinct arms. The two-band structure is a result of a few clouds contributing most of the emission observed. The random cloud-cloud motions readily account for the structure observed in the l-v diagram. Examining the data of Weaver and Williams (1973), no analogue to the double band structure is seen in HI. As spiral arms are delineated by large molecular clouds, a plot of the distribution of large ($r > 5$ pc) clouds versus R is another way to visualize the spiral arm. Figure 4.3 does not show the double edged structure of Figure 3.4 confirming that the structure is due to the emission being dominated by 5 individual clouds with CO luminosities greater than $10^3\ \mathrm{K\,kms}^{-1}$.

3.3 Determination of Arm and Interarm Cloud Populations

As described in Chapter 1, it is expected that clouds in the spiral arm region may have properties that differ from clouds in the interarm region. It is well known that GMCs are seen predominantly in spiral arms. To investigate the properties of molecular clouds as a function of environment, I have divided the data set into two populations; spiral arm and interarm. The spiral arm population consists of all clouds within the average FWHM of the Gaussian models fitting the arm; that is, all clouds with Galactocentric radii between 12 and 13.3 kpc. There are two corresponding interarm regions in the survey, $9.6\,\mathrm{kpc} < R < 12\,\mathrm{kpc}$ and $13.3\,\mathrm{kpc} < R \lesssim 16\,\mathrm{kpc}$. The properties of individual clouds and differences between the two cloud populations is the focus of Chapter 4.

Table 3.2: **Gaussian Model Fits to 13 kpc Arm Feature : Unclipped Data**

Model Name	R_0	FWHM	GRMS[a]	δR_0^b	δFWHM[c]
b_fit	12.50	1.58	32.2	0.001	0.002
b_2fit	12.50	1.59	54.6	0.001	0.002
b_avg_fit	12.61	2.90	178.9	0.005	0.030
b_avg_2fit	12.52	3.64	316.2	0.002	0.013
b_based_fit	12.51	0.90	275.0	0.001	0.020
b_based_2fit	12.52	0.94	302.0	0.001	0.003
b25_fit	12.70	1.11	41.8	0.001	0.001
b25_2fit	12.69	1.13	72.5	0.001	0.001
b25_avg_fit	12.67	2.04	364.6	0.001	0.005
b25_avg_2fit	16.99	4.08	516.7	0.002	0.012
b25_based_fit	12.75	2.30	162.2	0.001	0.005
b25_based_2fit	12.73	1.90	230.3	0.001	0.003
b50_fit	12.86	0.77	285.5	0.002	0.002
b50_2fit	12.84	0.75	147.9	0.002	0.002
b50_avg_fit	12.65	2.40	470.5	0.001	0.006
b50_avg_2fit	8.43	4.44	281.7	0.002	0.016
b50_based_fit	12.80	1.92	309.8	0.001	0.014
b50_based_2fit	12.90	3.77	332.7	0.002	0.017
b75_fit	12.57	2.01	69.2	0.001	0.004
b75_2fit	12.57	2.01	109.0	0.001	0.004
b75_avg_fit	12.40	3.20	378.0	0.002	0.011
b75_avg_2fit	14.49	4.73	296.8	0.004	0.023
b75_based_fit	12.36	3.10	178.5	0.007	0.042
b75_based_2fit	12.72	2.86	506.5	0.002	0.004

[a] RMS of model fit to data

[b] Uncertainty in centroid of fit

[c] Uncertainty in FWHM of fit

Table 3.3: Gaussian Model Fits to 13 kpc Arm Feature : Clipped Data

Model Name	R_0	FWHM	GRMS[a]	δR_0[b]	δFWHM[c]
bclip_fit	12.61	1.92	33.8	0.001	0.004
bclip_2fit	12.61	1.83	55.5	0.001	0.004
bclip_avg_fit	12.63	2.97	119.7	0.002	0.012
bclip_avg_2fit	12.52	2.66	163.2	0.002	0.011
bclip_based_fit	12.60	1.27	73.7	0.001	0.002
bclip_based_2fit	12.59	1.27	120.4	0.001	0.002
bclip25_fit	12.78	1.18	60.0	0.001	0.001
bclip25_2fit	12.78	1.24	99.3	0.001	0.001
bclip25_avg_fit	12.75	2.29	111.0	0.002	0.007
bclip25_avg_2fit	12.77	1.81	160.1	0.001	0.004
bclip25_based_fit	12.85	2.07	106.6	0.001	0.006
bclip25_based_2fit	12.82	1.92	160.4	0.001	0.005
bclip50_fit	12.77	2.35	98.9	0.001	0.007
bclip50_2fit	12.75	2.39	157.1	0.001	0.007
bclip50_avg_fit	12.75	0.86	129.6	0.001	0.002
bclip50_avg_2fit	12.92	1.34	187.9	0.001	0.002
bclip50_based_fit	12.94	1.94	124.8	0.001	0.006
bclip50_based_2fit	12.93	2.07	200.9	0.002	0.007
bclip75_fit	12.66	2.47	50.2	0.001	0.007
bclip75_2fit	12.67	2.46	80.2	0.001	0.007
bclip75_avg_fit	12.60	3.20	155.6	0.002	0.016
bclip75_avg_2fit	8.37	4.06	279.5	0.003	0.024
bclip75_based_fit	12.84	2.35	98.4	0.002	0.010
bclip75_based_2fit	12.84	2.35	103.7	0.002	0.010

[a] RMS of model fit to data

[b] Uncertainty in centroid of fit

[c] Uncertainty in FWHM of fit

CHAPTER 4

PHYSICAL PROPERTIES OF INDIVIDUAL CLOUDS

In this chapter, I will discuss the physical properties of the individual clouds identified in the survey using the methods outlined in Chapter 2. It is important not only to tabulate the properties of individual clouds, but also to determine the way cloud properties vary as a function of cloud size and environment. Two different cloud environments are investigated here: the 13 kpc spiral arm region and interarm regions. To facilitate the analysis, I further divide the clouds into two arbitrary classes, large and small. Large clouds have radii greater than 5 parsecs; small clouds have radii less than or equal to 5 parsecs. The large clouds include giant molecular clouds while the small clouds should be more similar to dark globules.

A more practical division of clouds is to divide clouds into groups based on how well resolved they are. For clouds which are detected in more than 5 beams, the cloud should be well resolved. Five beams is the minimum number needed for a central detection to be bounded along both the l and b directions. For clouds which are not detected in 4 positions surrounding a center detection but are detected in 5 or more positions (filamentary clouds), the peak temperatures of the detections are usually greater than .5K, which is an indicator that these detections are not beam diluted and the cloud is resolved. Clouds detected in one beam are most likely beam diluted and have very uncertain radii. To estimate the range of sizes that a cloud detected in only one beam can have, I assume that a cloud has to fill one-half of the beam to be detected (see the discussion in Section 2.7). The smallest possible angular radius of a cloud is 27". The largest possible angular radius is around 60". These two limits are shown in Figure 4.1. Clouds with smaller radii and larger brightness temperatures can exist; however, clouds should have minimum radii on the order of a parsec. A more detailed analysis of the minimum cloud temperature

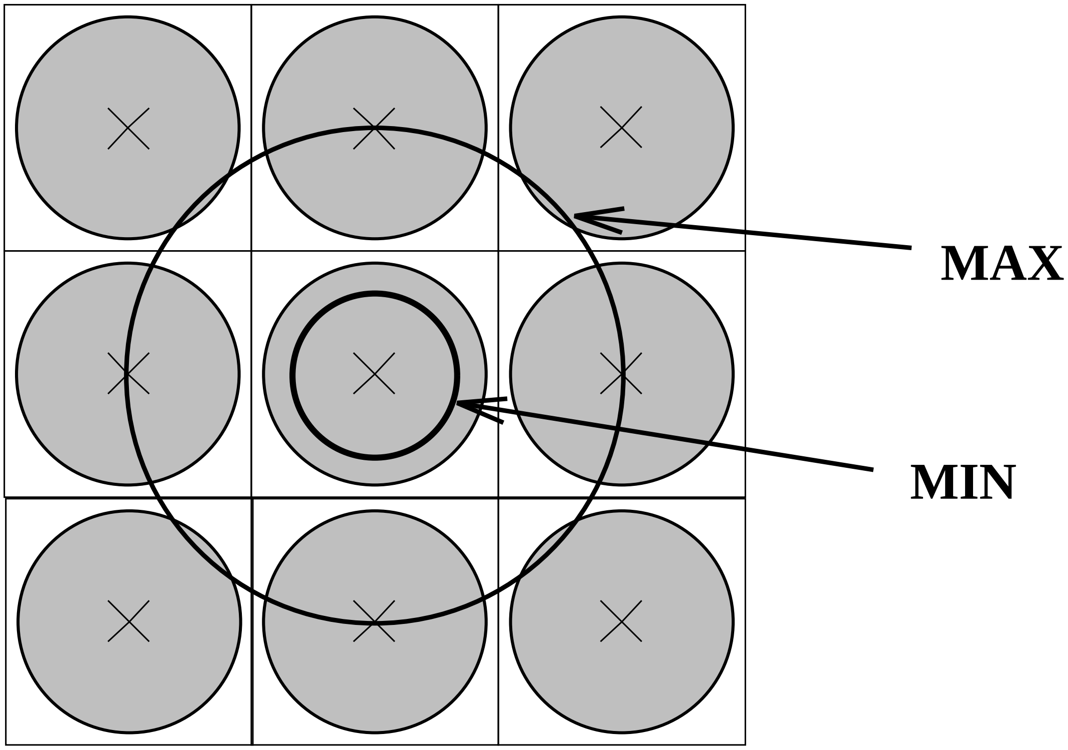

Figure 4.1: Sizes of largest and smallest clouds that can be detected at only one position

and size would involve convolving the surface brightness temperature distribution of the clouds as a function of cloud size and temperature with the main beam profile. As the clouds cannot be resolved, it is impossible to determine not only the brightness temperature distributions but also the sizes of the clouds.

The observed properties of all clouds identified in this survey are shown in Table 4.1. The name for each cloud has been determined from the centroid of the cloud's emission. All cloud names are of the form G##.##+#.## where the G stands for Galactic coordinates, the first numerical value is the Galactic longitude and the second is the Galactic latitude. Physical properties (mass, size, Galactocentric radius) of the clouds were derived using the methods outlined in Section 2.6. These quantities are tabulated for all clouds in Table 4.2.

Table 4.1: Observed Properties of Clouds in Survey

Cloud Name	Centroid		N	v_0	σ_v	Peak T_R^*	v_{Peak}	$\langle I \rangle$	$\langle rms \rangle$
	l	b	positions	kms^{-1}	kms^{-1}	K	kms^{-1}	K kms^{-1}	K
G75.92+1.47	75.92	1.47	1	-67.47	0.80	0.4	-67.300.6030.09		
G75.92+1.71	75.92	1.71	2	-54.68	1.02	1.4	-54.900	2.96810	
G75.93+1.76	75.93	1.76	9	-78.14	2.03	1.5	-77.700	2.18809	
G75.93+1.90	75.93	1.901	-72.55	0.74	0.6	-72.500.8320.09			
75.94	1.01	2	9-512	0.98	0.3	-58.800.5201.10			
2	-61.94	0.88	0.5	-62.100.680.10					
-0.45	1.93	0.6	-0.900	1.104	0.08				
-35.77	1.14	1.1	63100.92510						
0.4	-49.100	2.157	0.09						
-57.500.510.09									
0.08									
09									

Table 4.1 Observed Properties of Clouds in Survey – Continued

Cloud Name	Centroid l	b	N positions	v_0 kms^{-1}	σ_v kms^{-1}	Peak T_R^* K	v_{Peak} kms^{-1}	$\langle I \rangle$ K kms^{-1}	$\langle rms \rangle$ K
G76.05+1.05	76.05	1.05	1	-54.98	1.06	0.4	-54.90	0.727	0.12
G76.05+1.10	76.05	1.10	1	-88.63	1.10	0.3	-88.70	0.480	0.11
G76.05+1.67	76.05	1.67	1	-46.31	1.06	0.73	-46.50	0.70	0.09

85 1 -79.51 1.60.4 0.800 1.12 0.09

0.58 1.03 -51.00 0.867 0.11

6.900 1.03 0.09

1.414 0.09

Table 4.1 Observed Properties of Clouds in Survey – Continued

Cloud Name	Centroid l	Centroid b	N positions	v_0 kms^{-1}	σ_v kms^{-1}	Peak T_R^* K	v_{Peak} kms^{-1}	⟨I⟩ K kms^{-1}	⟨rms⟩ K
G76.18+1.58	76.18	1.58	1	-25.09	1.02	0.4	-25.000.634	0.09	
G76.18+1.80	76.18	1.80	1	-73.90	1.89	0.5	-74.400	1.59809	
G76.18+1.83	76.18	1.83	2	-57.31	0.61	2.0	-57.500	2.0260.09	
G76.18+1.87	76.18	1.87	1	-38.78	1.42	0.4	93300	1.10310	
G76.19+1.48	76.19	1.48	2	-32.58	1.07	0.4	-32.200.709.11		
+0.99	76.20.99		10	-0.36	1.17	1.9	-25.700	1.710.10	
	20	1.07	1	-40.92	1.22	0.3	-41.900.88308		
			6	-0.51	0.94	0.9	-0.800.88809		
				11	2.30	2.1	-0.900.86306		
						0.4	-64.000	1.510.11	
							68100	1.000.09	
							900.727	0.10	
								2.170.09	

Table 4.1 Observed Properties of Clouds in Survey – Continued

Cloud Name	Centroid l	b	N positions	v_0 kms^{-1}	σ_v kms^{-1}	Peak T_R^* K	v_{Peak} kms^{-1}	$\langle I \rangle$ K kms^{-1}	$\langle rms \rangle$ K
G76.28+1.17	76.28	1.17	1	-57.88	0.62	0.3	-57.50	0.53	0.12
G76.28+1.22	76.28	1.22	1	-57.89	1.13	0.5	-58.20	0.79	0.10
G76.28+1.33	76.28	1.33	1	-93.03	1.06	0.6	-93.30	0.90	0.08
76.28+1.43	76.28	1.43	1	-57.26	0.94	0.3	-58.20	0.59	0.10
	76.28	1.90	6	-35.80	0.66	5.3	-63.100	3.454	0.10
	76.31	1.35	36	-68.69	1.49	1.6	-69.900	1.26	0.13
		8	10	-60.40	2.23	1.3	-61.400	1.55	0.09
			1	-97.27	0.73	0.3	-97.20	0.50	0.08
				.96	1.20	0.4	-35.40	0.92	0.13
						2.1	-62.300	1.85	0.08
							-76.40	0.537	0.14
							00	1.50	0.08

Table 4.1 Observed Properties of Clouds in Survey – Continued

Cloud Name	Centroid l	b	N positions	v_0 kms^{-1}	σ_v kms^{-1}	Peak T_R^* K	v_{Peak} kms^{-1}	⟨I⟩ $K\,kms^{-1}$	⟨rms⟩ K
G76.39+1.30	76.39	1.30	13	-42.28	1.16	1.0	-42.600	1.340	0.11
G76.39+1.31	76.39	1.31	15	-42.33	1.12	1.0	-42.600	1.176	0.10
G76.40+1.33	76.40	1.33	1	-68.54	0.75	0.4	-68.800	0.585	0.09
G76.40+1.50	76.40	1.50	1	-79.68	0.75	0.3	-79.600	0.612	0.09
1.57	76.40	1.57	1	-42.48	1.43	0.4	-43.900	0.740	0.09
	2	1.23	1	-67.76	1.12	0.5	-68.600	1.298	0.10
			8	-76.42	0.76	1.1	-75.700	1.298	0.10
				-42.62	1.31	0.3	-41.300	0.908	0.11
				6	1.20	0.4	-33.500	0.880	0.07
						0.4	-24.400	0.680	0.09
							-54.900	0.610	0.10
								1.767	0.09
								7	0.10

Table 4.1 Observed Properties of Clouds in Survey – Continued

Cloud Name	Centroid		N	v_0	σ_v	Peak T_R^*	v_{Peak}	⟨I⟩	⟨rms⟩
	l	b	positions	kms^{-1}	kms^{-1}	K	kms^{-1}	K kms^{-1}	K
G76.53+1.52	76.53	1.52	1	-85.14	0.68	0.3	-84.80	0.425	0.09
G76.53+1.72	76.53	1.72	1	-32.11	0.72	0.3	-32.20	0.684	0.09
G76.53+1.76	76.53	1.76	2	-76.94	0.81	1.5	-77.000	2.628	0.10
G76.54+1.63	76.54	1.63	2	-76.46	0.63	0.8	-76.400	1.659	0.10
G76.55+1.57	76.55	1.57	1	-58.16	1.37	0.4	-58.20	0.736	0.06
72	76.55	1.72	1	-24.09	0.68	0.4	-24.40	0.699	0.10
		1.84	33	-87.12	1.47	1.7	-87.400	2.034	0.09
		1.25	2	-0.60	0.83	1.0	-0.300	1.311	0.07
			1	-63.97	0.51	0.4	-63.700	0.628	0.09
					0.90	0.3	-6.00	0.68	0.09
						2.8	-0.900	2.21	0.09
							-55.000	1.74	0.13
							.50	0.711	0.08

Table 4.1 Observed Properties of Clouds in Survey – Continued

Cloud Name	Centroid l	b	N positions	v_0 kms^{-1}	σ_v kms^{-1}	Peak T_R^* K	v_{Peak} kms^{-1}	⟨I⟩ K kms^{-1}	⟨rms⟩ K
G76.70+1.47a	76.70	1.47	1	-84.0870.3			-84.200	0.600.09	
G76.70+1.47b	76.70	1.47	1	-95.78	1.101.3		-95.900	0.950.09	
76.70+1.90	76.70	1.90	1	-23.54	0.821.3		-23.100	0.570.10	
	76.73	1.54	7	-64.32.87		1.1	-64.000	0.997	0.07
	3	1.67	1	-6.54	1.07	0.6	-6.600	1.134	0.07
		1.39	11	-27.37	0.79	1.0	-27.000	1.104	0.08
		1.60	1	-2.34	1.09.3		03200	0.710.08	
				-72.57	1.57	1.6	-71.200	2.05510	
				5	2.30	5.7	-70.600	2.477	0.07
					0.68	1.0	-6.000	0.940.11	
						.4	-94.600	0.650.10	
								0.720.09	
									0.09

Table 4.2: Physical Properties of Clouds in Survey

Cloud Name	R kpc	d kpc	Radius pc	Area pc^2	L_{CO} K kms^{-1}	M_{CO} $M_\odot$	M_{VIR} $M_\odot$
G75.92+1.47	12.4	11.4	1.9	10.9	7	47	1473
G75.92+1.71	11.4	10.0	2.3	16.9	50	340	2428
G75.93+1.76	13.4	12.6	6.2	121.8	266	1812	14722
G75.93+1.90	12.9	12.0	2.0	12.1	10	68	634
G75.94+1.01	11.8	10.4	2.4	18.5	10	65	1388
G75.94+1.43	12.0	10.8	2.5	19.6	13	91	1321
G75.95+1.01	12.6	11.6	4.7	68.2	75	512	20386
G75.96+1.66	10.2	8.1	4.0	49.8	46	313	3044
G75.97+1.17	11.0	9.4	1.5	7.5	16	110	12240
G75.97+1.28	11.6	10.3	1.7	9.0	5	31	1729
G75.97+1.30	13.2	12.4	2.0	13.0	6	41	1213
G75.97+1.78	10.3	8.2	3.8	45.2	79	536	7801
G75.98+1.87	10.1	7.9	1.3	5.3	4	26	1875
G76.00+1.50	12.9	12.0	2.8	24.3	27	185	996
G76.00+1.85	13.5	12.8	2.1	13.9	11	74	1570
G76.02+1.50	12.2	11.0	1.8	10.3	13	88	3968
G76.02+1.77	12.6	11.6	17.1	920.4	3613	24566	115103
G76.04+1.02	10.9	9.2	2.1	14.3	20	140	2429
G76.04+1.61	11.7	10.3	10.3	332.5	846	5749	9569
G76.04+1.62	12.8	11.9	13.9	609.3	1789	12165	130030
G76.05+1.05	11.4	10.0	1.6	8.4	6	42	1361
G76.05+1.10	14.5	14.0	2.3	16.6	8	54	907
G76.05+1.67	10.9	9.1	1.5	7.0	5	33	237
G76.05+1.85	13.5	12.8	2.1	13.8	16	105	3350
G76.06+1.32	11.1	9.5	2.7	23.1	20	136	5140
G76.06+1.46	11.5	10.1	2.3	17.3	18	122	11579
G76.06+1.73	10.3	8.1	3.5	39.2	55	377	9401
G76.07+1.65	13.1	12.3	2.0	12.8	6	38	732
G76.08+1.28	13.5	12.7	2.1	13.7	7	47	1448
G76.08+1.77	13.7	13.0	2.1	14.3	28	189	2216
G76.09+1.38	11.9	10.6	2.5	18.9	16	111	3384
G76.09+1.90	12.9	12.0	4.8	72.5	164	1116	4185
G76.12+1.10	11.7	10.3	1.7	9.0	9	59	1066
G76.13+1.03	11.7	10.3	3.4	35.8	27	187	3291
G76.13+1.17	9.6	7.0	1.1	4.2	3	19	1749

Table 4.2 Physical Properties of Clouds in Survey – Continued

Cloud Name	R kpc	d kpc	Radius pc	Area pc^2	L$_{\rm CO}$ K kms^{-1}	M$_{\rm CO}$ M$_\odot$	M$_{\rm VIR}$ M$_\odot$
G76.13+1.28	10.6	8.7	1.4	6.4	5	33	366
G76.13+1.69	10.2	8.0	1.9	10.8	17	118	1888
G76.16+1.41	11.5	10.1	4.0	51.5	50	343	3685
G76.17+1.83	14.1	13.5	2.2	15.4	10	71	1090
G76.18+1.58	9.6	7.0	1.1	4.1	3	18	411
G76.18+1.80	13.0	12.1	2.0	12.3	20	134	4088
G76.18+1.83	11.6	10.2	2.4	17.6	36	243	851
G76.18+1.87	10.4	8.3	1.4	5.9	6	44	3638
G76.19+1.48	10.0	7.7	1.8	10.1	7	49	1531
G76.20+0.99	9.7	7.1	3.7	42.8	73	498	3610
G76.20+1.07	10.5	8.5	1.4	6.2	5	37	2505
G76.20+1.15	11.9	10.5	4.2	56.4	50	341	3047
G76.20+1.34	12.5	11.4	7.5	175.5	152	1030	47640
G76.20+1.38	12.1	10.8	1.8	9.9	15	102	6746
G76.20+1.55	14.1	13.4	2.2	15.2	15	104	5673
G76.20+1.60	13.9	13.2	2.2	14.8	11	73	3568
G76.21+1.35	12.6	11.6	3.3	34.2	74	505	1773
G76.22+1.33	12.3	11.1	2.6	20.9	19	130	3732
G76.22+1.88	13.1	12.2	2.0	12.6	16	111	7464
G76.25+0.97	11.9	10.6	1.7	9.5	10	71	2391
G76.25+1.17	14.0	13.4	2.2	15.1	15	102	8626
G76.25+1.53	9.8	7.3	1.2	4.5	3	19	656
G76.25+1.79	13.0	12.1	8.2	211.0	316	2152	33901
G76.26+1.89	11.6	10.2	2.9	26.5	40	269	2712
G76.28+1.17	11.7	10.2	1.7	8.9	5	32	595
G76.28+1.22	11.7	10.2	1.7	8.9	7	48	508
G76.28+1.33	15.1	14.6	2.4	18.0	16	112	928
G76.28+1.43	11.6	10.2	1.7	8.8	5	36	1770
G76.28+1.90	10.2	8.0	3.2	32.7	113	767	1510
G76.31+1.35	12.5	11.4	11.3	397.9	502	3412	30181
G76.32+0.98	11.8	10.5	5.5	93.4	145	988	12374
G76.32+1.27	15.6	15.2	2.5	19.7	10	67	1002
G76.32+1.35	10.2	8.0	1.3	5.5	5	34	2288
G76.33+0.97	9.7	7.0	3.7	42.0	78	530	2900
G76.33+1.05	13.3	12.4	2.0	13.1	7	48	4323
G76.33+1.06	12.5	11.4	3.8	44.3	66	452	20354

Table 4.2 Physical Properties of Clouds in Survey – Continued

Cloud Name	R kpc	d kpc	Radius pc	Area pc^2	L$_{CO}$ K kms^{-1}	M$_{CO}$ M$_\odot$	M$_{VIR}$ M$_\odot$
G76.33+1.15	11.8	10.4	1.7	9.2	4	29	609
G76.33+1.30	13.4	12.6	2.1	13.5	5	32	356
G76.33+1.33	11.5	10.1	19.6	1202.6	3118	21206	33618
G76.33+1.35	9.6	6.8	1.1	4.0	4	25	2346
G76.35+0.98	11.0	9.3	1.5	7.3	6	44	1050
G76.37+1.17	14.0	13.4	2.2	15.1	9	62	933
G76.37+1.22	12.5	11.4	1.9	11.0	9	60	1501
G76.39+1.09	12.5	11.4	3.2	33.1	59	399	5601
G76.39+1.30	10.6	8.6	5.1	82.0	110	748	7937
G76.39+1.30	10.6	8.6	5.5	94.7	111	758	8795
G76.40+1.33	14.3	13.6	2.2	15.8	9	63	662
G76.40+1.50	13.5	12.7	2.1	13.7	8	57	1231
G76.40+1.57	10.6	8.7	1.4	6.3	5	32	3498
G76.42+1.23	12.4	11.3	1.9	10.8	14	95	3396
G76.42+1.63	13.2	12.3	5.7	102.8	134	908	4849
G76.43+1.07	10.6	8.7	1.4	6.3	6	40	3603
G76.43+1.20	10.1	7.8	1.3	5.1	4	31	1495
G76.43+1.23	9.6	6.9	1.1	4.0	3	19	568
G76.45+1.03	11.4	9.8	1.6	8.1	5	34	2996
G76.46+1.70	13.2	12.3	4.5	64.1	113	770	1907
G76.47+1.68	12.8	11.8	1.9	11.8	9	62	719
G76.48+1.58	9.7	7.1	1.2	4.3	3	20	695
G76.48+1.62	11.9	10.6	1.7	9.5	5	33	756
G76.48+1.75	13.3	12.4	3.5	38.9	52	352	1995
G76.49+1.46	12.7	11.6	9.9	309.4	1080	7344	13049
G76.49+1.62	12.6	11.4	3.8	44.3	34	232	2021
G76.50+1.38	10.5	8.5	1.4	6.1	11	77	463
G76.51+1.23	11.5	10.0	3.3	34.1	100	676	10651
G76.53+1.52	14.1	13.4	2.2	15.2	6	44	548
G76.53+1.72	10.0	7.6	1.2	4.9	3	23	816
G76.53+1.76	13.3	12.4	2.9	25.9	68	462	1860
G76.54+1.63	13.2	12.3	2.9	25.6	42	289	4198
G76.55+1.57	11.7	10.2	1.7	8.8	6	44	1238
G76.55+1.72	9.6	6.8	1.1	3.9	3	19	450
G76.57+1.84	14.3	13.7	12.9	523.2	1064	7236	33609
G76.58+1.25	12.6	11.5	2.7	22.3	29	199	1760

Table 4.2 Physical Properties of Clouds in Survey – Continued

Cloud Name	R kpc	d kpc	Radius pc	Area pc^2	L_{CO} K kms^{-1}	M_{CO} $M_\odot$	M_{VIR} $M_\odot$
G76.58+1.63	10.3	8.1	1.3	5.5	4	24	476
G76.58+1.90	12.2	11.0	1.8	10.2	7	47	1766
G76.59+1.44	12.5	11.3	9.5	281.2	621	4226	82372
G76.60+1.23	11.4	9.9	4.0	49.4	86	584	2220
G76.62+1.47	14.1	13.4	3.8	45.9	33	224	2371
G76.63+1.22	9.7	7.1	1.2	4.3	4	28	1399
G76.65+1.42	9.7	7.0	1.2	4.2	2	14	802
G76.65+1.82	11.6	10.1	1.7	8.6	4	29	1049
G76.67+1.57	12.9	11.9	2.0	12.0	9	63	645
G76.67+1.62	10.0	7.5	1.2	4.8	3	22	3177
G76.68+1.75	13.2	12.2	21.6	1459.6	3572	24287	41760
G76.69+1.83	14.1	13.4	13.4	560.5	975	6628	18285
G76.70+1.47a	14.1	13.4	2.2	15.1	9	62	1129
G76.70+1.47b	15.4	14.9	2.4	18.8	18	122	3969
G76.70+1.90	9.5	6.7	1.1	3.8	2	15	706
G76.73+1.54	12.1	10.8	4.7	69.7	70	473	2374
G76.73+1.67	12.3	11.1	1.8	10.4	12	80	1589
G76.75+1.39	9.7	7.1	3.9	46.9	52	352	2446
G76.75+1.60	9.8	7.3	1.2	4.5	3	22	1712
G76.75+1.63	12.9	11.8	7.5	176.4	362	2465	22364
G76.76+1.45	12.7	11.6	15.4	745.0	1846	12549	34588
G76.76+1.47	12.2	11.0	5.7	101.8	96	655	2858
G76.77+1.47	15.2	14.7	2.4	18.2	12	81	1218
G76.80+1.55	9.5	6.6	1.1	3.7	3	18	1123
G76.80+1.87	12.8	11.8	3.3	35.1	44	302	1854
G76.81+1.68a	13.0	11.9	10.4	337.9	508	3451	53910
G76.81+1.68b	13.9	13.1	3.0	29.2	17	116	2953
G76.82+1.50	14.3	13.6	2.2	15.7	14	94	607
G76.82+1.50	14.3	13.6	2.2	15.7	14	94	607

Table 4.3: Number of Clouds as a Function of Cloud Environment

	Arm	Interarm	Total
Small	28	88	116
Large	13	8	21
Total	41	96	137

4.1 Statistics of Cloud Ensemble

This survey observed 137 individual molecular clouds. These clouds were identified using the CLOUDFIND algorithm as discussed in Section 2.6. The distribution of clouds as a function of environment and cloud size is tabulated in Table 4.3. Table 4.4 gives the distribution of resolved/under-resolved clouds versus cloud size. Not surprisingly, all the large clouds fill five or more beams, while the majority of the small clouds are under-resolved. For under-resolved clouds, it is difficult to determine properties such as mass and size. While the number of under-resolved clouds decreases the usefulness of the data set, 35 clouds exist for which physical properties can be confidently determined.

In general, the clouds are not circular in cross section. Many clouds are elongated, and the larger clouds usually have more than one emission maxima. Some of the clouds have rather complicated boundaries which cannot be described using simple figures of rotation. The clouds are not elongated in any preferential direction. One can only speculate on the actual three-dimensional shapes of these objects, as no information exists on their structure along line of sight. Despite the irregular shapes of the clouds, they will be modeled as spheres with radii as defined in Section 2.6.2. The error introduced into the virial masses of the clouds is of order unity.

4.2 Cloud Sizes as a Function of Environment

The spiral arm is dominated by the large molecular clouds which make up 31% of the arm population. This result is not surprising as it is well known that GMCs are the dominant molecular component of spiral arms. As shown in Figure 4.3, the distribution of large clouds is sharply peaked with few clouds in the interarm regions. Large clouds make up a small percentage (8%) of the number of clouds in the interarm population.

As shown in Figure 4.2, small clouds are more pervasive. The distribution of small clouds is relatively constant from R = 9 kpc to R = 14 kpc with an enhancement in the number of clouds between 12 to 14 kpc due to the spiral arm. The enhancement in the number density of small clouds for the arm region is $\sim 40\%$.

There is a sharp drop in the small cloud distribution for $R > 14\,\mathrm{kpc}$, probably due to a combination of two effects. The density of molecular material appears to decrease as a function of Galactocentric radius. In addition, the linear diameter subtended by the telescope beam is larger for clouds at larger R; therefore, beam dilution will significantly affect the chance of detecting small clouds. From this survey, it is impossible to tell which of these effects is more prominent; however, it is likely that there is a real decrease in the amount of molecular material at larger R. This effect has been noted by several authors including Wouterloot *et al.* (1990), who used the IRAS point source catalog as an independent tracer of star-forming molecular material out to R = 20 kpc.

If the decrease is due solely to beam dilution effects, then the number of small clouds detected should decrease as the square of the distance to the clouds, which is approximately the square of the clouds' Galactocentric radii. Implicit in the estimate of an inverse square dependence are the assumptions: the cloud size distribution for the smaller clouds is the same for all R, and a fraction of the clouds have sizes such that they will not be detected at some fiducial distance. These assumptions seem reasonable for the smallest clouds in the survey. It is likely that there exists a number of clouds at R = 10 kpc that would not be detected at R = 16 kpc. It appears that the decrease in number of clouds observed at larger R is

Table 4.4: Resolved vs. Under-resolved Clouds as a Function of Cloud Size

	Small	Large
Under-resolved	102	0
Resolved	14	21

not due to beam dilution as illustrated by Figure 4.4, where the decrease in under-resolved clouds as a function of R is extremely sudden at $R \approx 14.5\,\mathrm{kpc}$, unlike the smooth variation in the number of clouds due to beam dilution effects, which is demonstrated by the dashed line in the figure.

The distribution of cloud sizes as a function of environment is directly related to the formation and destruction mechanisms of molecular clouds. Current thinking on cloud formation theories has been described in Chapter 1. The distribution of clouds in this survey may provide a useful data set to compare to predictions of new cloud formation theories.

4.2.1 Cloud Size Spectrum

The cloud size spectrum, or number of clouds as a function of cloud radius, is a diagnostic tool used in determining which physical processes affect the life cycle of a cloud. If a self-similar fragmentation process forms molecular clouds (and cores) on all size scales, there will be a universal relationship for the size spectrum [Scalo (1985)]. The exact nature of the scaling law will be determined by the nature of the process. Variations in the shape of the spectrum as a function of cloud size or environment may help determine the nature of the formation and destruction processes involved.

Typically, the size spectrum is modeled as a power law in either cloud size or mass. For the first formulation of the size spectra,

$$n_{cl}(r) = \left(\frac{r}{r_0}\right)^{\xi} \tag{4.1}$$

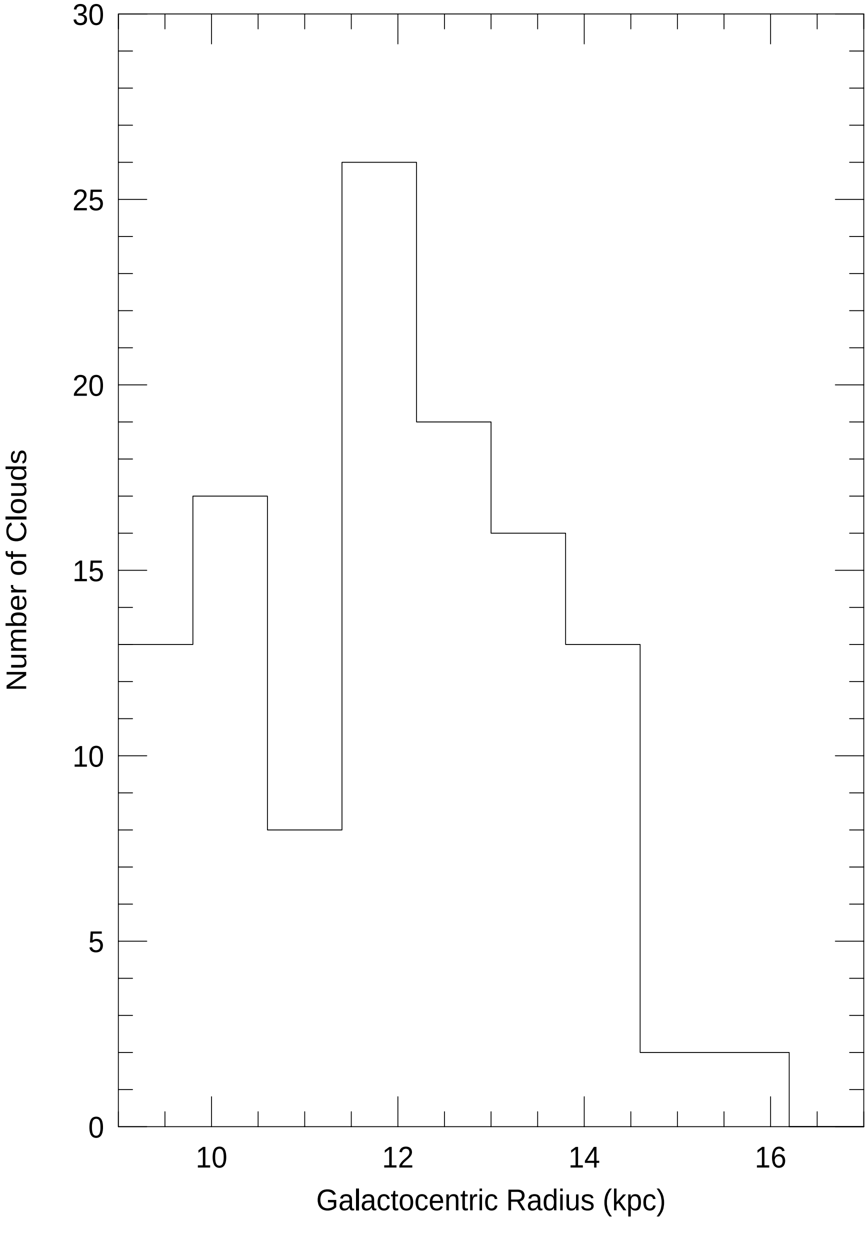

Figure 4.2: **Histogram of the distribution of small ($r < 5$ pc) clouds versus Galactocentric radius. The bin size is 0.8 kpc.**

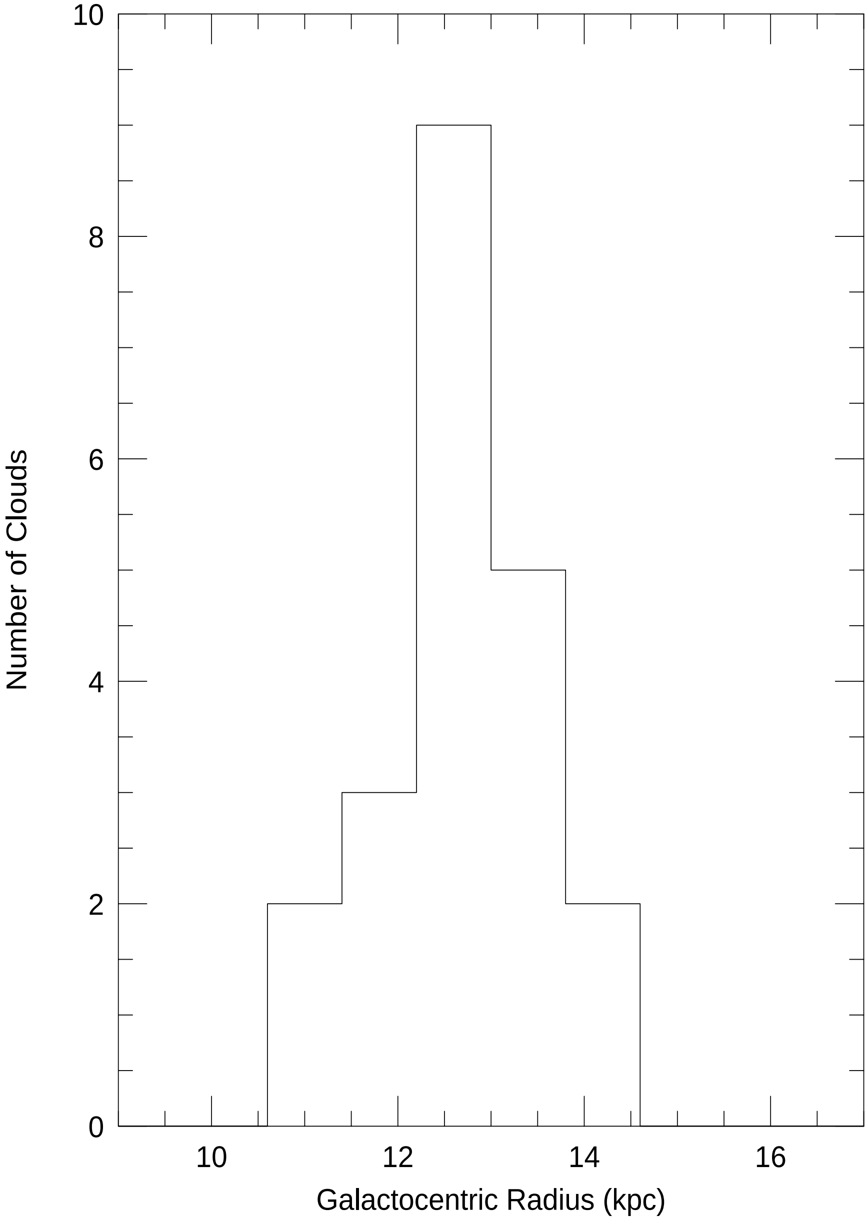

Figure 4.3: **Histogram of the distribution of large ($r > 5$ pc) clouds versus Galactocentric radius. The bin size is 0.8 kpc.**

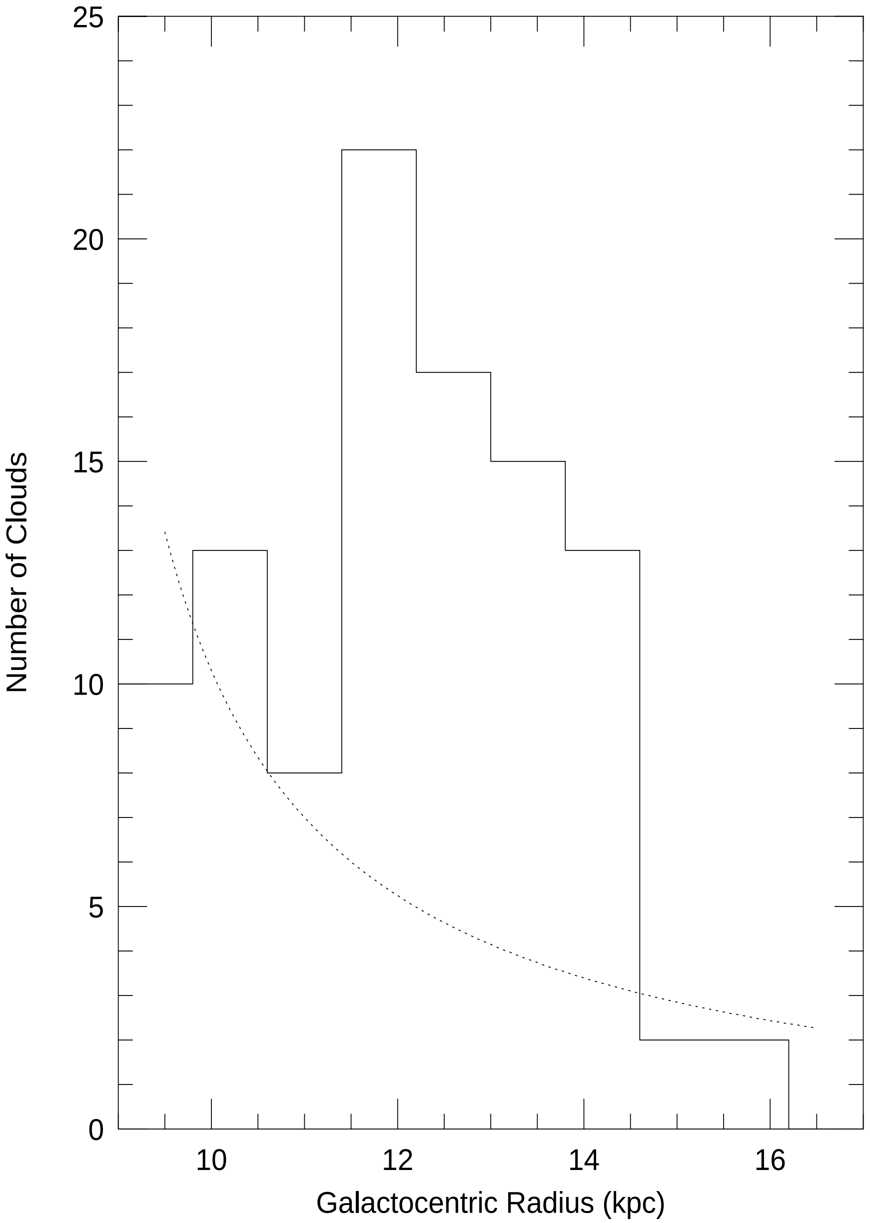

Figure 4.4: Histogram of the distribution of under-resolved clouds versus Galactocentric radius. The bin size is 0.8 kpc. The dashed line represents the smooth decrease in clouds detected if beam dilution was a significant factor in cloud detection.

Table 4.5: Previous Size Spectrum Measurements

Authors	ξ	Comments
Terebey *et al.* (1986)	-2.7	16 outer Galaxy clouds
Solomon *et al.* (1979)	-3.4	inner Galaxy
Liszt *et al.* (1981)	-3.3	inner Galaxy
Casoli *et al.* (1984)	-2.4	Orion and Perseus Arms
Sanders *et al.* (1985)	-2.3	Corrected for distance ambiguity

where $n_{cl}(r)$ is the number of clouds per unit cloud radius, r_0 is a normalization constant and ξ is the power-law index.

At the present time, little data exists on the size spectrum for molecular clouds in the outer Galaxy, Terebey *et al.* (1986) measured the size spectrum for 16 clouds identified in their observations. Their clouds ranged in size from 2 to 40 parsecs in diameter. Their best fit value for ξ is $-2.8\,^{+1.3}_{-1.0}$ for a flat rotation curve and $-2.6\,^{+1.9}_{-0.7}$ using the rotation curve of Blitz *et al.* (1980). Several authors have measured the size spectrum of clouds in the inner Galaxy (see Table 4.5).

Figure 4.5 shows the number density of clouds as a function of cloud radius for my data set. The majority of clouds have radii smaller than five parsecs. Most of the clouds with radii of one parsec or less are under-resolved; therefore, those radii are very uncertain and are probably larger (see Section 2.6.3). The variation in cloud size may be more easily visualized by plotting log(number) vs. log(cloud radius) as shown in Figure 4.6. Best fit values for the cloud size spectrum are given in Table 4.6. The uncertainty in the number of clouds per bin is approximated as

$$\delta N = \frac{1}{\Delta r} \sum_{i=1}^{N} \delta r_i \tag{4.2}$$

where N is the number of clouds per bin, Δr is the bin width and δr_i is the uncertainty in the radius of a cloud, which is the linear size of the sample spacing at the distance of the cloud. The values of Q, a measure of the goodness-of-fit, indicate that the fits are good. Q is the probability that χ^2 is greater than calculated for normally distributed errors [Bevington (1969)]. As $Q \approx 1$, it is likely that I have overestimated the error in N. Within the rather large uncertainties for each coefficient, the fits agree. Some evidence exists for a steeper power law when small clouds are included, as the arm fit will be dominated by the larger clouds (which have smaller uncertainties in $\log N$). In addition, the power law fit for just the resolved clouds is much flatter than the fit using all clouds, once again indicating that the size spectrum for larger clouds is flatter than for smaller clouds. The size spectra as a function of environment and cloud type are given in Figures 4.6-4.9.

The most appropriate value to compare with the Terebey *et al.* results is the fit for the resolved clouds (see Figure 4.7). The resolved clouds have the best determined cloud radii and should have the best fit. The χ^2 values for the fits for resolved clouds, all clouds and interarm clouds are excellent. The χ^2 for the arm cloud fit is slightly lower as there are fewer arm clouds. It is clear that the fits to my data are much shallower than the Terebey *et al.* results. It is quite likely that these discrepancies can be attributed to the small counting statistics in both samples (35 resolved clouds versus 16 total for Terebey *et al.*) and the coarse sampling of their survey (47% of their data was taken at four beamwidth sampling). Also, their 90% confidence level includes models with $\xi = -1.0$, which is in much better agreement with my values.

It is somewhat puzzling that the power-law index is so different for inner and outer Galaxy clouds. This difference is probably due to two different factors. The first factor is that the inner Galaxy studies primarily look at large clouds (or even complexes of clouds) and cannot measure the size spectrum of smaller clouds. In addition, the methods used to determine cloud sizes are very different. If the method of identifying clouds and measuring cloud sizes described in this thesis are applied to inner Galaxy data, it is possible that much of the difference between the inner and outer Galaxy size spectra can be resolved. Unfortunately, it may be impossible to apply the current methods of cloud detection in the inner Galaxy, as cloud blending prevents identification of unique cloud boundaries. The second cause could be that the cloud size spectrum really is different for the outer Galaxy than the inner Galaxy. It is likely that the difference between my results and inner Galaxy work is caused by a combination of these two factors.

The dip in the size spectrum for arm clouds at $\log(r) = 0.8$ (see Figure 4.8) may be an indication that the life cycles of small and large clouds in the arm region are governed by different physical processes. The dip in the number of clouds is on the order of the uncertainty in N for that bin, $N(\log r \sim .8) = 0.30 \pm .59$. Further observations of the cloud population in the 13 kpc arm are necessary to determine if this dip is significant. The interarm population size spectrum is monotonically decreasing as a function of cloud radius. This suggests that clouds of all sizes in the interarm region are affected by similar physical processes.

The differences in the shapes of the size spectra between arm and interarm regions may be an indication that the life cycles of arm and interarm clouds are different. One possible scenario is that clouds form in the arm as condensates of HI super-clouds. Then, these clouds undergo star formation and fragment as the spiral arm passes by. Large clouds form through instabilities in the super-cloud which condense into GMCs. The GMCs fragment and form smaller clouds. As time passes, the smaller remnant clouds enter interarm regions. Another probable scenario is that clouds form by both aggregation and condensation. As the arm and interarm regions will have different ratios of aggregation to condensation, the size spectra of each region should be different. Note that current observations do not rule out cloud formation governed entirely by aggregation; however, the variation in size spectra between arm and interarm regions is suggestive that condensation may be an important process in the arm. Additionally, it is extremely important to

Table 4.6: **Size Spectra Power Laws**

ξ	σ_ξ	χ^2	Q	Comments
-0.9	0.6	0.23	0.99	All Clouds
-0.8	0.7	0.16	0.96	Resolved Clouds
-0.7	0.7	0.75	0.86	Arm Clouds
-1.2	0.9	0.11	0.99	Interarm Clouds

consider cloud destruction mechanisms and how remnant clouds are formed.

4.3 Cloud Mass Distribution

The distribution of cloud masses as a function of cloud environment is shown in Figures 4.10-4.12 with all masses calculated using the virial approximation as described in Chapter 2. Uncertainties for each log mass bin were not calculated since the uncertainty in cloud mass can be quite large (factor of 2). As expected, the arm region has a significant number of high mass ($M > 10^4$ M$_\odot$) clouds, while there are very few high mass clouds in the interarm region. This does not imply that interarm regions are devoid of GMCs; however, GMCs are much more abundant in the arm region. It can be argued that the mass distribution is a truer measure of cloud size distribution than the distribution of cloud radii, but any mass estimate depends on cloud radius.

Both the arm and interarm mass distributions exhibit a turnover point at which the slope of the cloud mass distribution changes sign. If physical, this decrease in number of clouds for small mass bins would indicate that I have observed the lower limit of the cloud mass distribution ($\sim 10^2$ M$_\odot$). However, it is unlikely that this turnover is real. Cloud masses are extremely uncertain for under-resolved (smallest) clouds. In addition, no corresponding turnover is noticed in the cloud size spectra for the arm and interarm populations. Therefore, while the mass distributions

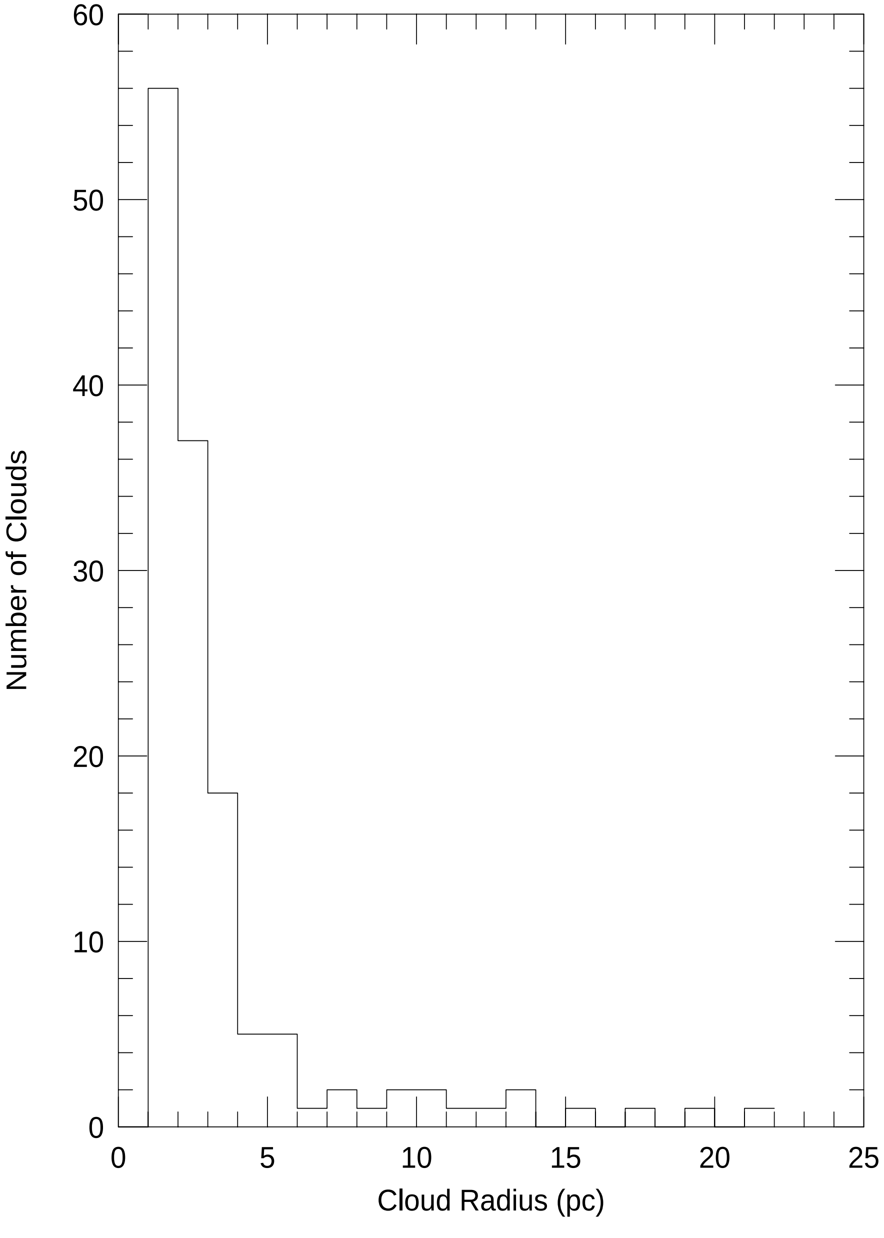

Figure 4.5: Number density of clouds versus cloud radius for all clouds

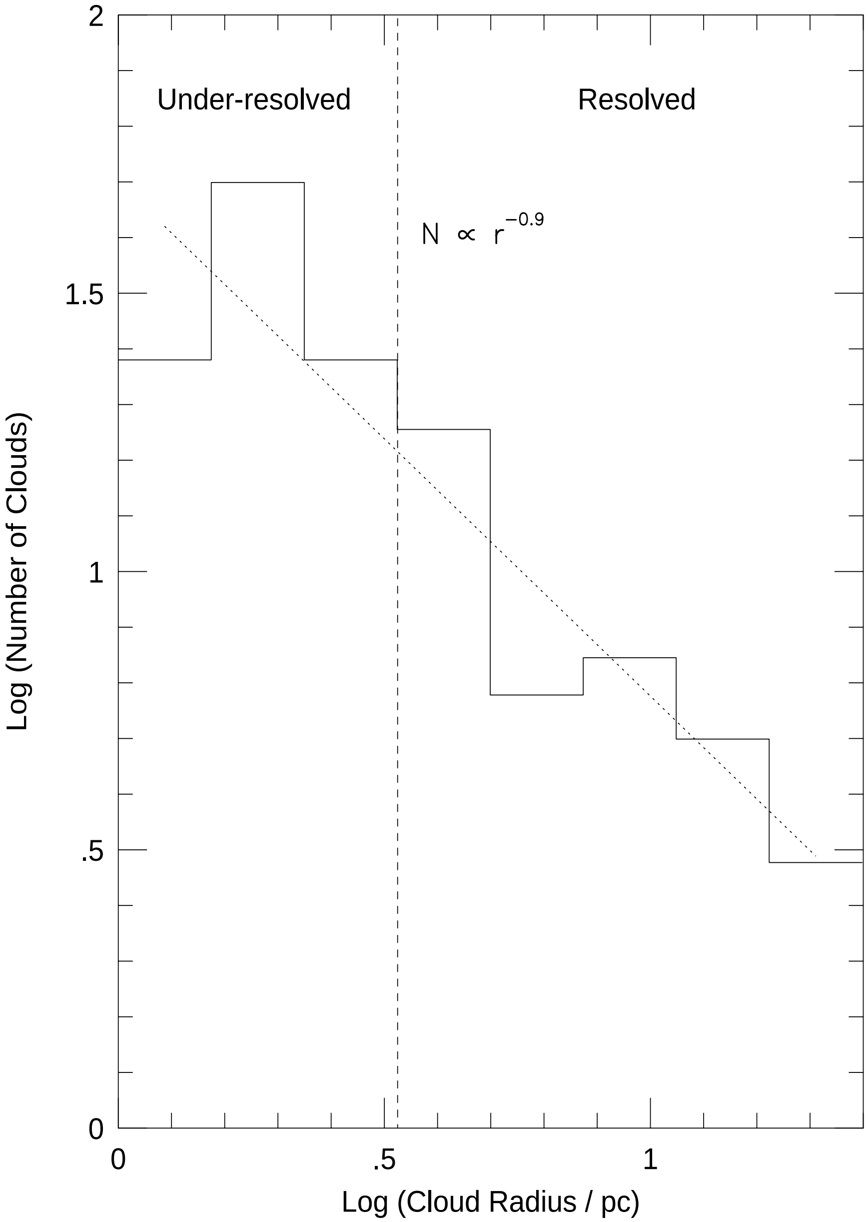

Figure 4.6: Log number density of clouds versus log cloud radius for all clouds. The dotted line is the best fit power spectrum to the data. The dashed line is the division between resolved and under-resolved clouds.

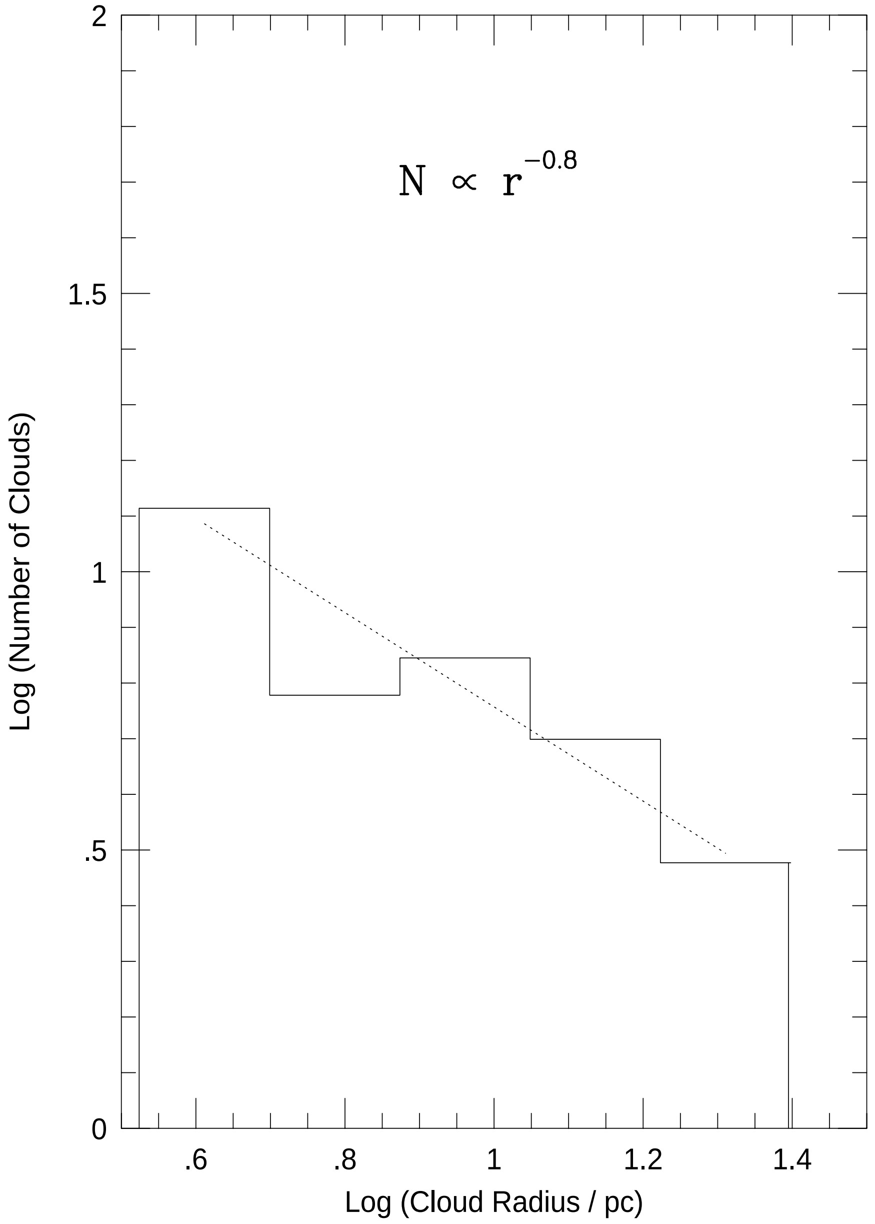

Figure 4.7: Log number density of clouds versus log cloud radius for resolved clouds. The dotted line is the best fit power spectrum to the data.

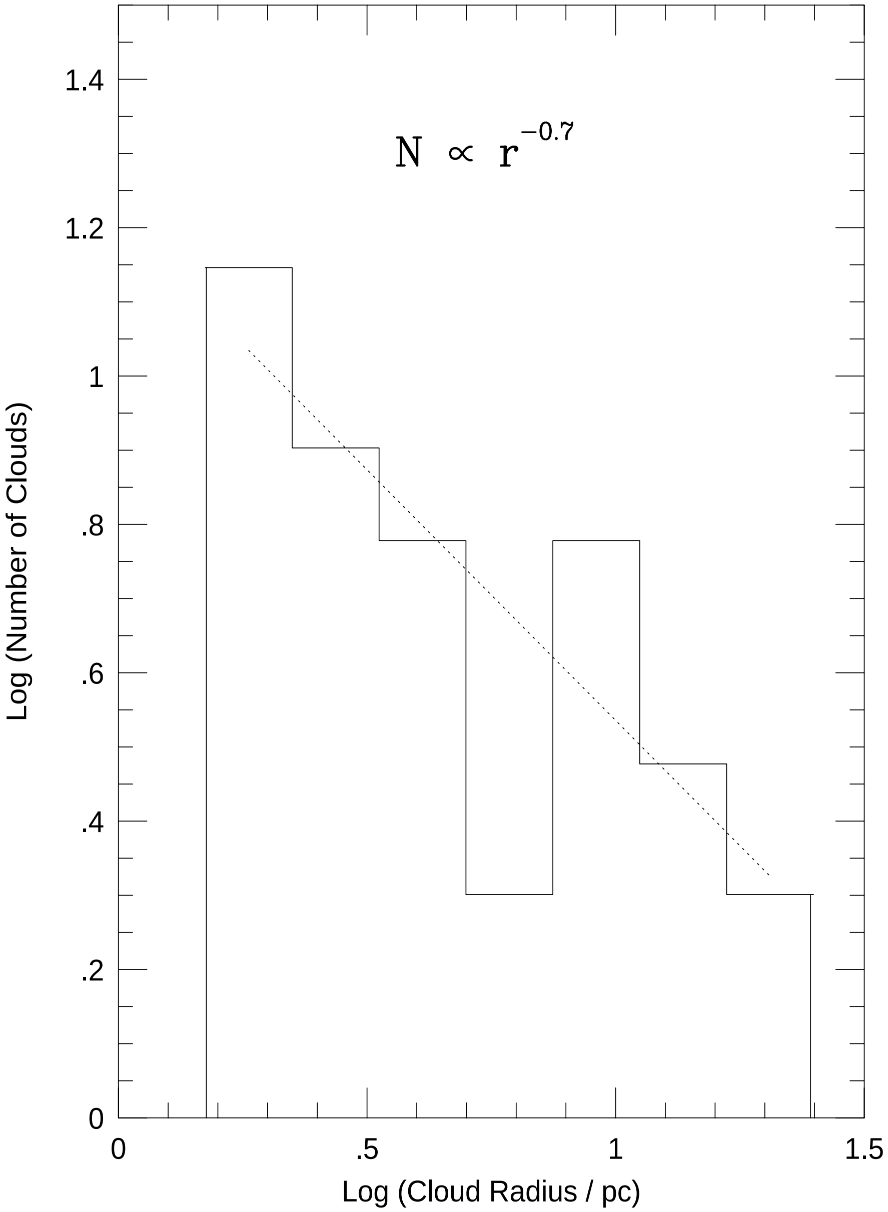

Figure 4.8: Log number density of clouds versus log cloud radius for arm clouds. The dotted line is the best fit power spectrum to the data.

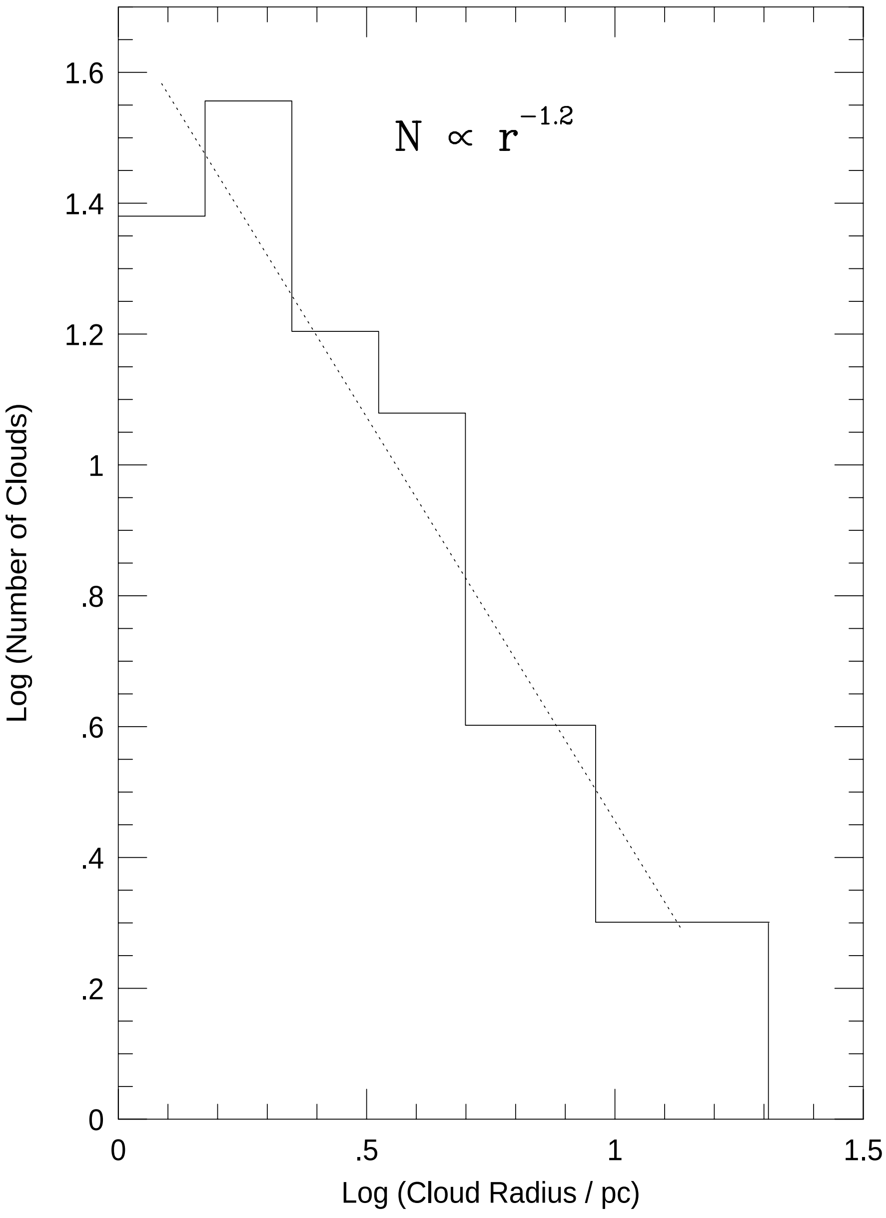

Figure 4.9: **Log number density of clouds versus log cloud radius for interarm clouds. The dotted line is the best fit power spectrum to the data.**

suggest a cloud mass cutoff of a few times $10^2\,\mathrm{M}_\odot$, this result is extremely tentative. Further observations are necessary to determine the lower limit of the cloud mass distribution. On the other hand, a dip in mass distribution at $M = 10^4\mathrm{M}_\odot$ for the arm population is very similar to the dip in the cloud size spectrum for arm clouds. The first maximum in the arm distribution occurs at $\log(M/\mathrm{M}_\odot) = 3.2$, which is where the global maximum occurs in the interarm distribution. It appears that the arm distribution consists of two components : a small cloud component, which resembles the interarm distribution, and a large cloud component.

4.3.1 Mass Breakdown By Environment

The total mass contained in the survey region is $1.07 \times 10^6\,\mathrm{M}_\odot$, which is about the mass of a very large inner Galaxy GMC or a molecular cloud complex. However, the clouds in this survey fill too large a volume to be considered a single complex. In other words, the survey region is not rich in molecular material. The breakdown of the total mass as a function of cloud environment and size is evident in Table 4.7. Included in Table 4.7 are masses calculated using the relationship between $L(CO)$ and $M(\mathrm{H}_2)$ as described in Section 2.6.5.

The fraction of total region mass contained in clouds within a certain mass range as a function of cloud environment is given in Figures 4.13-4.15. These figures have the same scaling so that histograms of equal size on separate graphs contain the same mass fraction. For the arm population, most of the mass is contained in clouds $10^4\,\mathrm{M}_\odot$ or larger. The distribution of total mass is a steeply increasing function of cloud mass. This sharply contrasts the interarm mass distribution, which is much flatter. An appreciable fraction of the interarm mass is made of clouds with masses ranging from $10^3 - 10^4\,\mathrm{M}_\odot$. The total mass distribution resembles the arm mass distribution in shape; however, 30% of the total mass is contained in small ($r < 5\,\mathrm{pc}$) clouds.

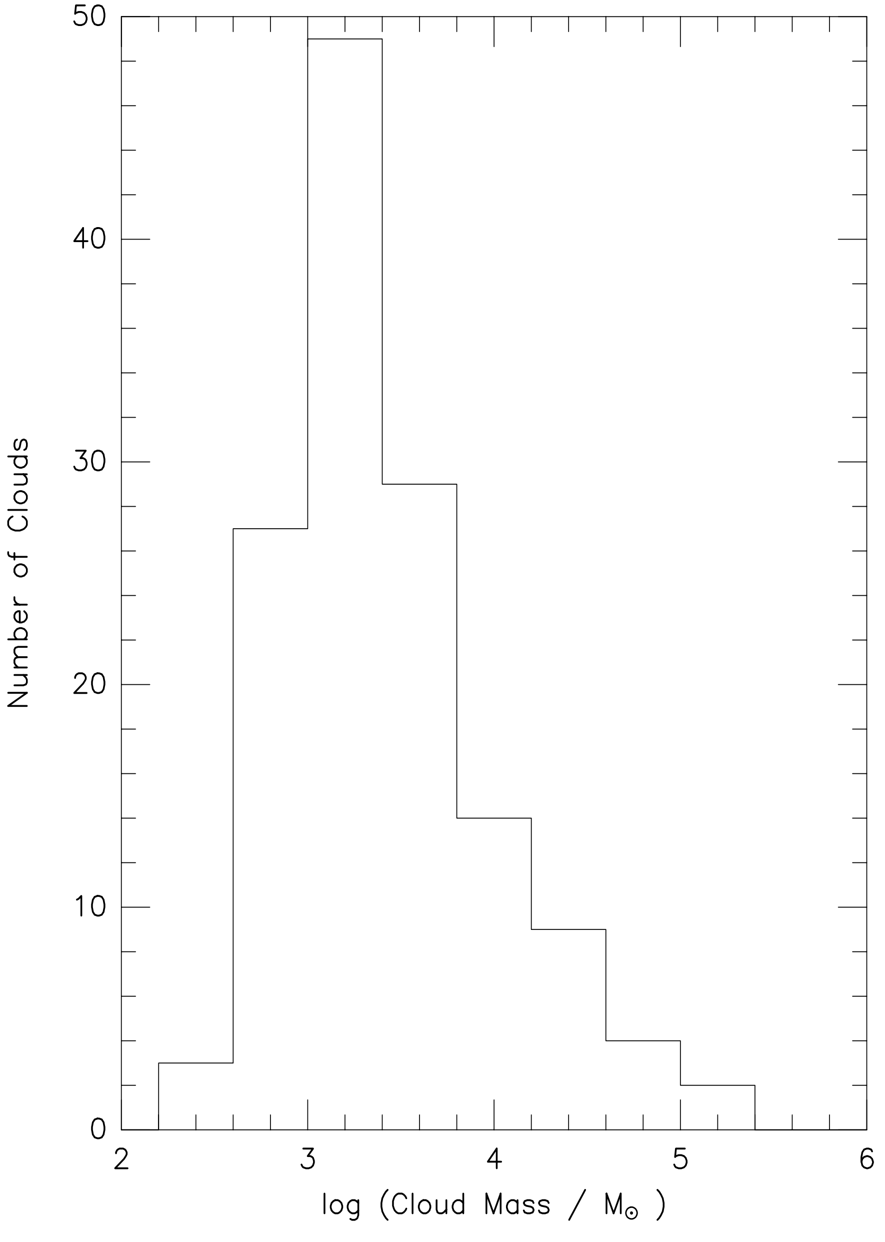

Figure 4.10: Number of clouds as a function of log virial mass

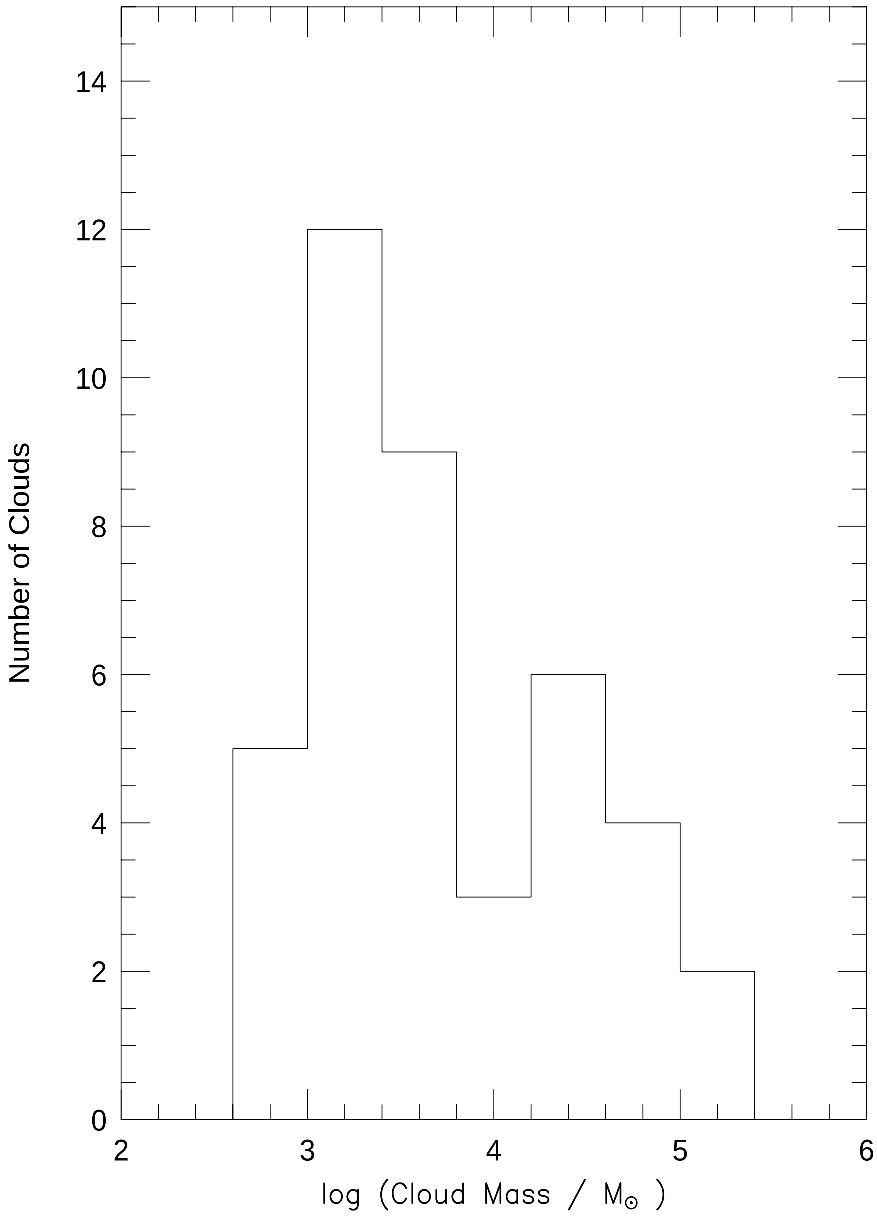

Figure 4.11: Number of arm clouds as a function of log virial mass

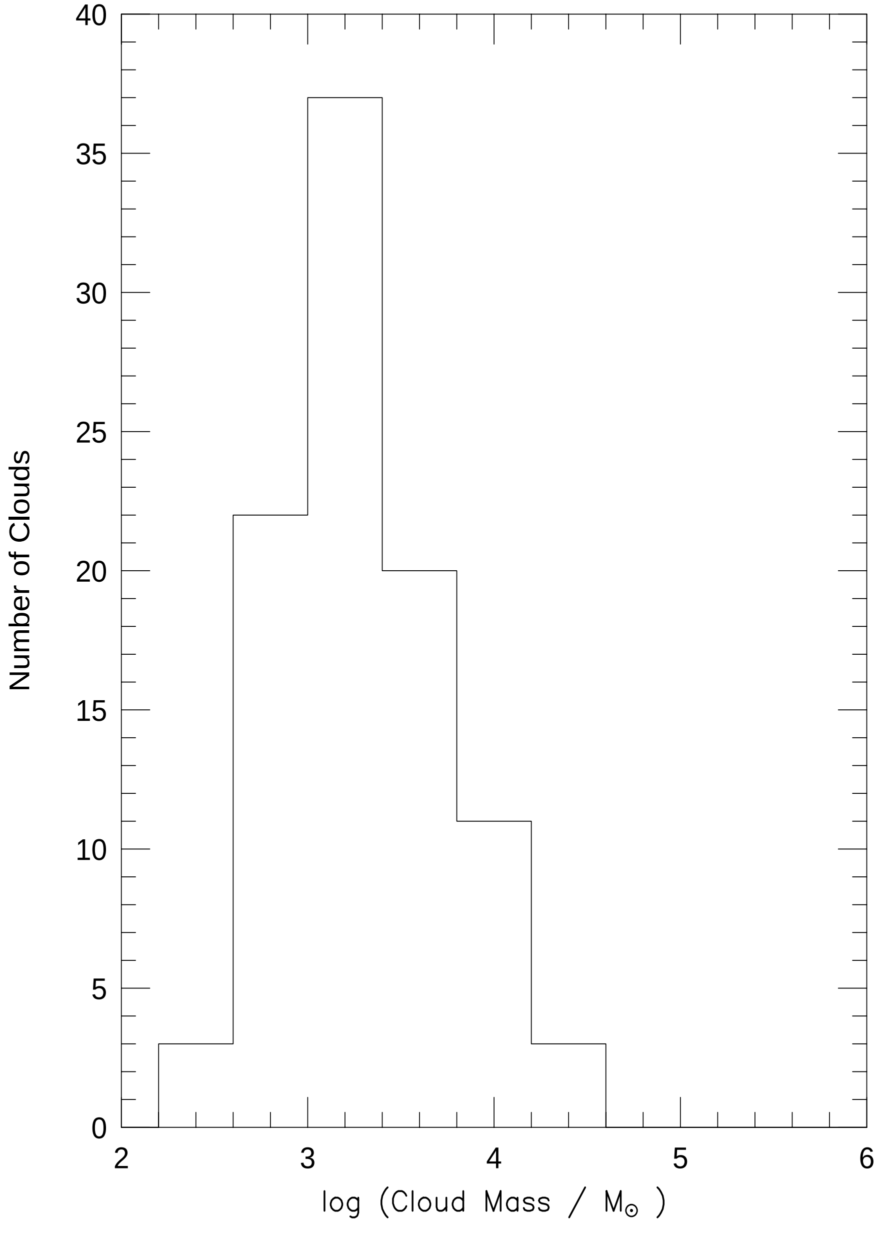

Figure 4.12: Number of interarm clouds as a function of log virial mass

For comparison, the fraction of total mass per unit cloud mass for the environments studied using the X factor mass estimate is shown in Figures 4.16-4.18. Using the X factor masses, the arm population contributes 65% of the total mass, which is identical to the virial mass result. However, the total mass in the survey region is an order of magnitude less. Small clouds contribute a small fraction (11%) of the total mass, if the X factor mass is the better estimate. More importantly, the contribution of small clouds to the interarm mass is significantly reduced. The distribution of total mass fraction as a function of cloud mass is steeper than the virial mass interarm distribution. The distribution function for the arm population is similar in shape for both types of mass estimation.

The major reason for the discrepancy with previous work is that previous molecular surveys were biased towards large and/or star forming clouds as described in Chapter 1. As a result, small clouds were either not observed or observed with such low resolution that the linewidths and physical sizes of the small clouds could not be determined. It is important to note that although the low resolution, fully sampled surveys receive the same amount of emission from the small clouds as received by my higher resolution, fully sampled observations; it is difficult to identify the small clouds in the low resolution surveys, as their emission is significantly beam diluted. As a result, it is difficult, if not impossible to identify lines in the spectra, and measure cloud sizes and linewidths. Therefore, low resolution surveys cannot be used to measure the masses of small clouds using the virial approximation. If the conversion factor for I_{CO} to N_{H_2} is not well known for the cloud type and environment, then the mass contribution due to small clouds would be miscalculated using a low resolution survey. The pros and cons of the two different mass estimates are outlined in the next sub-section.

4.3.2 Which Mass Estimate to Use?

Figure 4.19 shows the ratio of virial mass to X factor mass for my survey. For all clouds observed, the virial mass estimate is higher than the X factor estimate. It is unlikely that the largest molecular clouds are not gravitationally bound; therefore, the virial mass should be accurate to within a factor of two.

The situation is less clear for smaller clouds. It can be argued that the smaller clouds resemble high-latitude (HL) molecular clouds as discussed in Blitz *et al.* (1984). Both sets of clouds have small radii (on the order of a parsec) and low peak temperatures (as low as 0.6 K for the HL clouds, 0.3 K for my clouds). However, the mean ratio of the ^{12}CO line intensity to ^{13}CO line intensity is 10 for the HL clouds, while it is around 4 for the few clouds observed in both tracers for this survey. This is an indication that the clouds in this survey have higher optical depths than the HL clouds and are likely to contain more molecular material. The HL clouds are also characterized by a rich velocity structure and large internal velocity dispersions for some of the HL clouds. Blitz *et al.* argue that the HL clouds are not virialized for two reasons: that the internal velocities of the HL clouds are large, which is an indicator that the clouds are young and have not reached equilibrium, and the resulting contribution to the total molecular mass from these clouds results in an unreasonable mass surface density for the Galactic plane. For this reason, they argue that deriving cloud masses using the X factor is the most appropriate method for their cloud set. However, they question the validity of this approximation as the ^{13}CO results indicate that the masses of their clouds should be a factor of three lower than the masses calculated using the ^{12}CO luminosities.

The small clouds in this work do not have large internal velocity dispersions and a detailed internal velocity structure. This is in sharp contrast to the large velocity dispersions (up to $10\mathrm{kms}^{-1}$) for the HL clouds. The low cloud temperatures are partially due to beam dilution of the signal. In most regards, these clouds resemble the larger clouds in the survey except that they have smaller radii and masses. It is likely that the small clouds in my survey are close to virial equilibrium, and the virial approximation is the best mass estimate.

The large uncertainty in cloud size for the smallest clouds may help explain the large M_{VIR}/M_{CO} for small clouds. If the cloud radii listed are actually a factor of two larger for the under-resolved clouds, then M_{VIR}/M_{CO} will be reduced by a factor of two. This is likely because some emission is missed by sampling with full beamwidth spacing. If the cloud does not completely fill the majority of an adjacent beam, then the emission from that beam will not be identified as belonging to the cloud. It is much less likely that the clouds are smaller than the radii listed, as the radii would be smaller then one parsec, which is approximately the size of a photodissociation region for a molecular cloud in the ISM. Preliminary results from half-beamwidth sampled maps of some of the clouds indicate that the cloud radii are slightly larger than reported for the smallest clouds.

Considering the uncertainties in the cloud radii (a factor of 2 for the smallest clouds) and virial mass (a factor of two for all clouds), there still remains a large discrepancy between the virial and X factor masses for all clouds, large and small, resolved and under-resolved. The data strongly support the conclusion that the X factor for the clouds in this survey is much larger than the X factor for inner Galaxy clouds and is also larger than the X factor used by Mead & Kutner (1988). From Figure 4.19, it is clear that there is no trend based on the environment (arm/interarm) of the cloud. One possible cause of the difference may be the star formation efficiency of the clouds. Internal heating sources may dramatically change the ^{12}CO emission of the cloud by localized heating of the gas. As reviewed in Section 2.6.5, the X factor is inversely proportional to cloud temperature. The star formation efficiency of these clouds is presently unknown due to obscuration and blending with foreground objects along the same line of sight. The clouds from

Table 4.7: Total Molecular Mass as a Function of Cloud Environment and Size

	Arm			Interarm			
	Small	Large	Total	Small	Large	Total	Total
				(10^5 $M_\odot$)			
Virial	1.08	6.13	7.21	2.11	1.34	3.50	10.07
L(CO)	0.06	0.99	1.05	0.12	0.45	0.57	1.62

Mead & Kutner (1988) are large, bright clouds. Many of these clouds are actively forming stars [Mead *et al.* (1990)]. Therefore, it is not surprising that my random sample of outer Galaxy clouds has a higher X factor than Mead's sample of bright, star forming clouds.

4.4 Cloud Temperatures

The kinetic temperatures of the clouds have been estimated using the method outlined in Section 2.6.4 and by assuming the ^{12}CO ($J = 1 \rightarrow 0$) transition is thermalized. While the two-level approximation is not strictly valid for ^{12}CO, this approximation provides some information on the coupling of the line brightness temperature to the radiation temperature of the cloud. It is a better approximation than assuming that the transition is totally thermalized, and the excitation temperature of the line is the kinetic temperature.

The kinetic temperature of the cloud is determined from the peak line temperature observed. As the beam subtends 2-4 parsecs at the distances of the clouds, the calculated temperature is an average temperature over that length scale in the cloud. As clumps in clouds are usually a parsec or smaller in length, it is likely that the ^{12}CO observations will measure the temperature of the envelope or an average of a clump and the envelope.

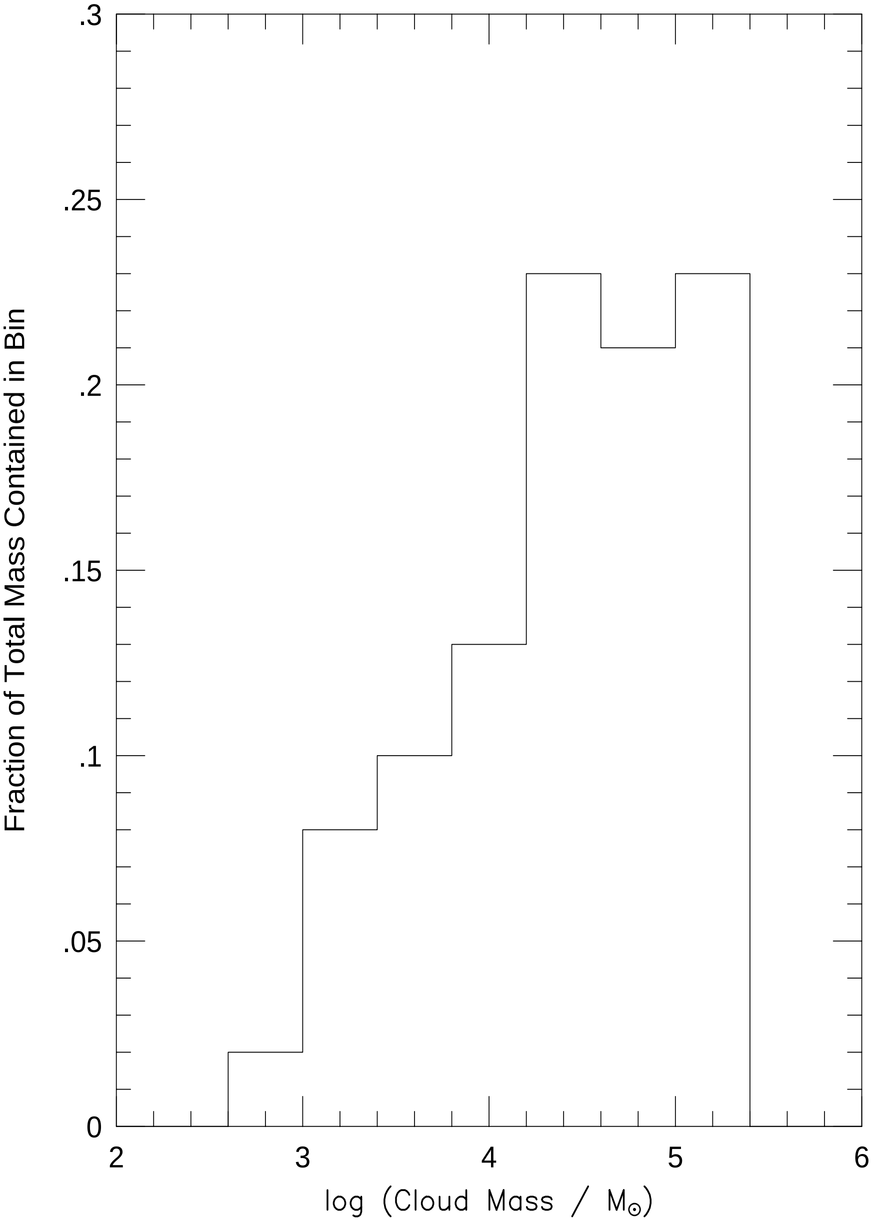

Figure 4.13: Fraction of total mass contained in clouds versus log(cloud mass). Mass is calculated using the virial approximation, and the data bins are 0.4 decades in width.

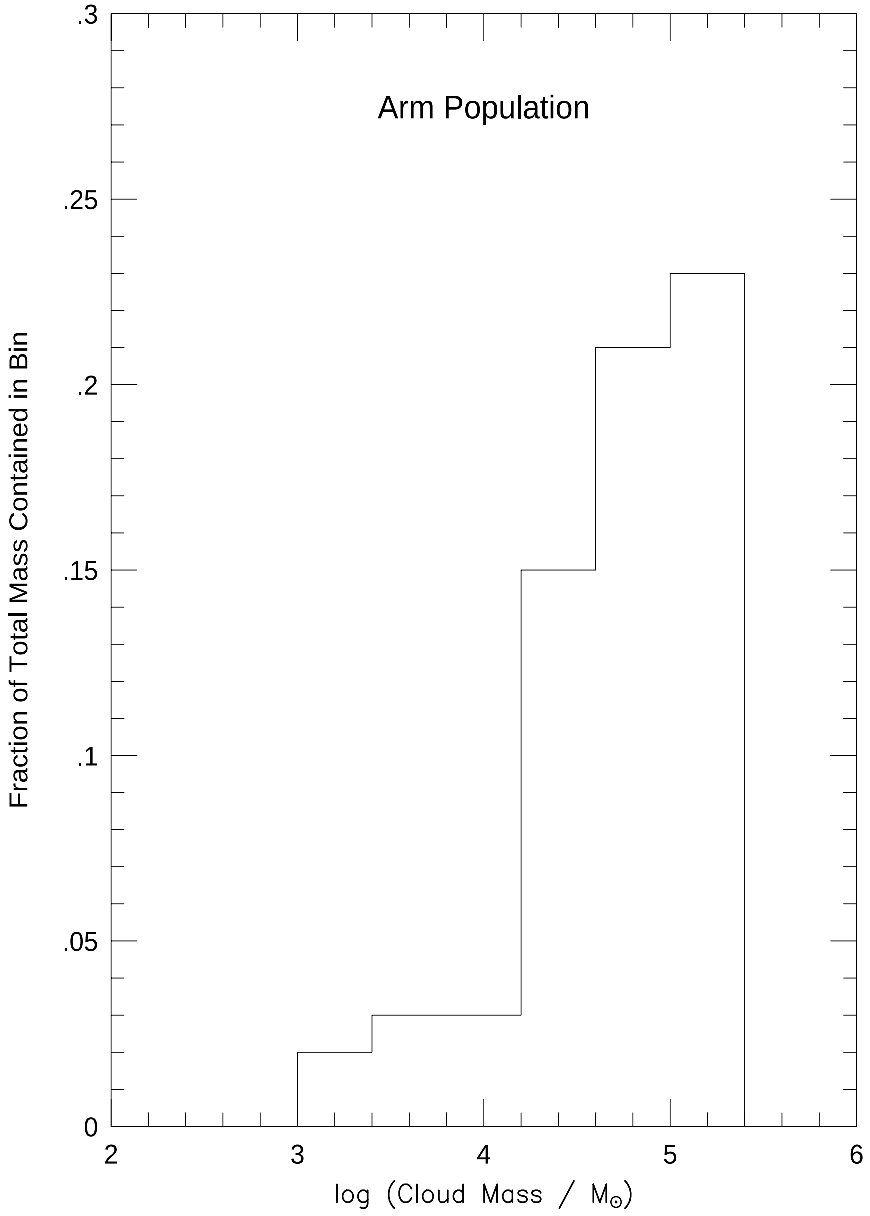

Figure 4.14: **Fraction of total mass contained in arm clouds versus log(cloud mass). Mass is calculated using the virial approximation, and the data bins are 0.4 decades in width.**

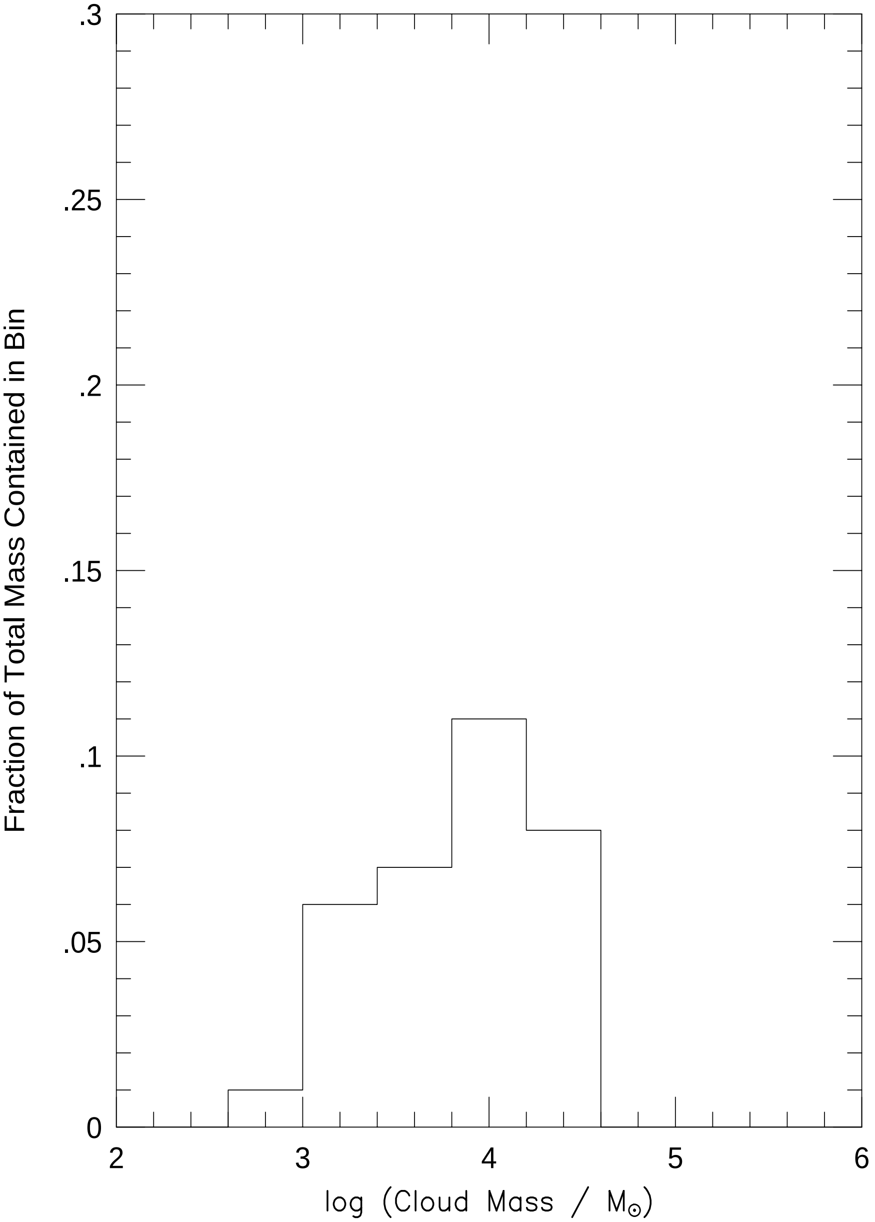

Figure 4.15: Fraction of total mass contained in interarm clouds versus log(cloud mass). Mass is calculated using the virial approximation, and the data bins are 0.4 decades in width.

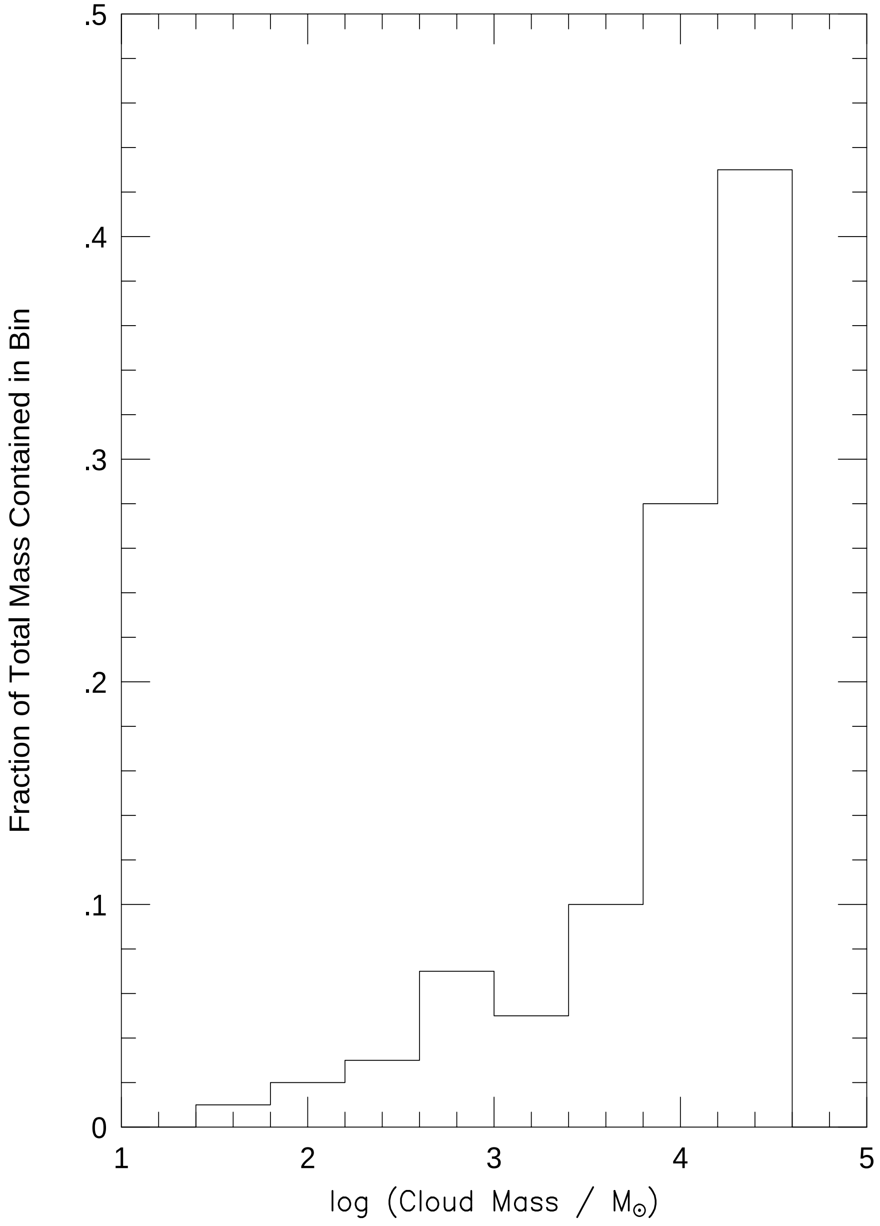

Figure 4.16: Fraction of total mass contained in clouds versus log(cloud cloud mass). Mass is calculated using the X factor approximation, and the data bins are 0.4 decades in width.

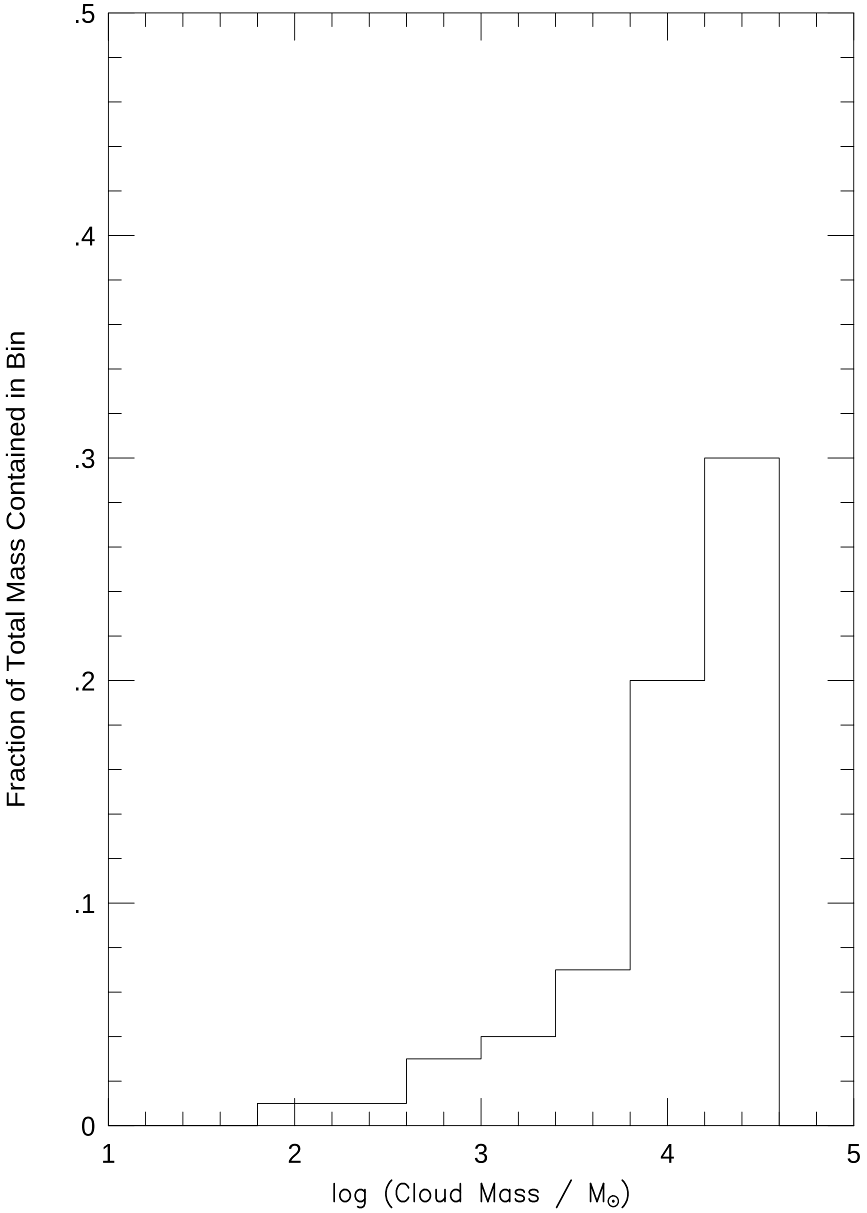

Figure 4.17: **Fraction of total mass contained in arm clouds versus log(cloud mass). Mass is calculated using the X factor approximation, and the data bins are 0.4 decades in width.**

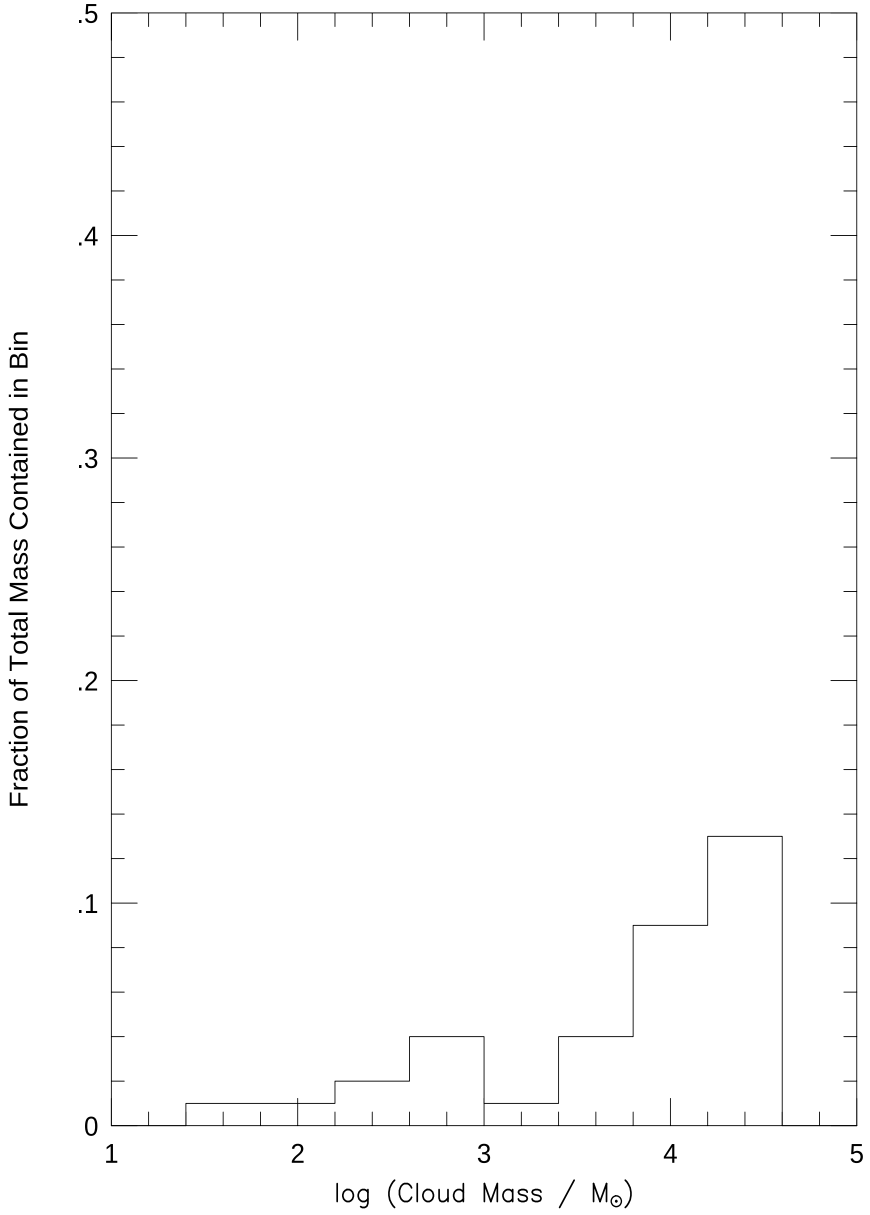

Figure 4.18: **Fraction of total mass contained in interarm clouds versus log(cloud mass). Mass is calculated using the X factor approximation, and the data bins are 0.4 decades in width.**

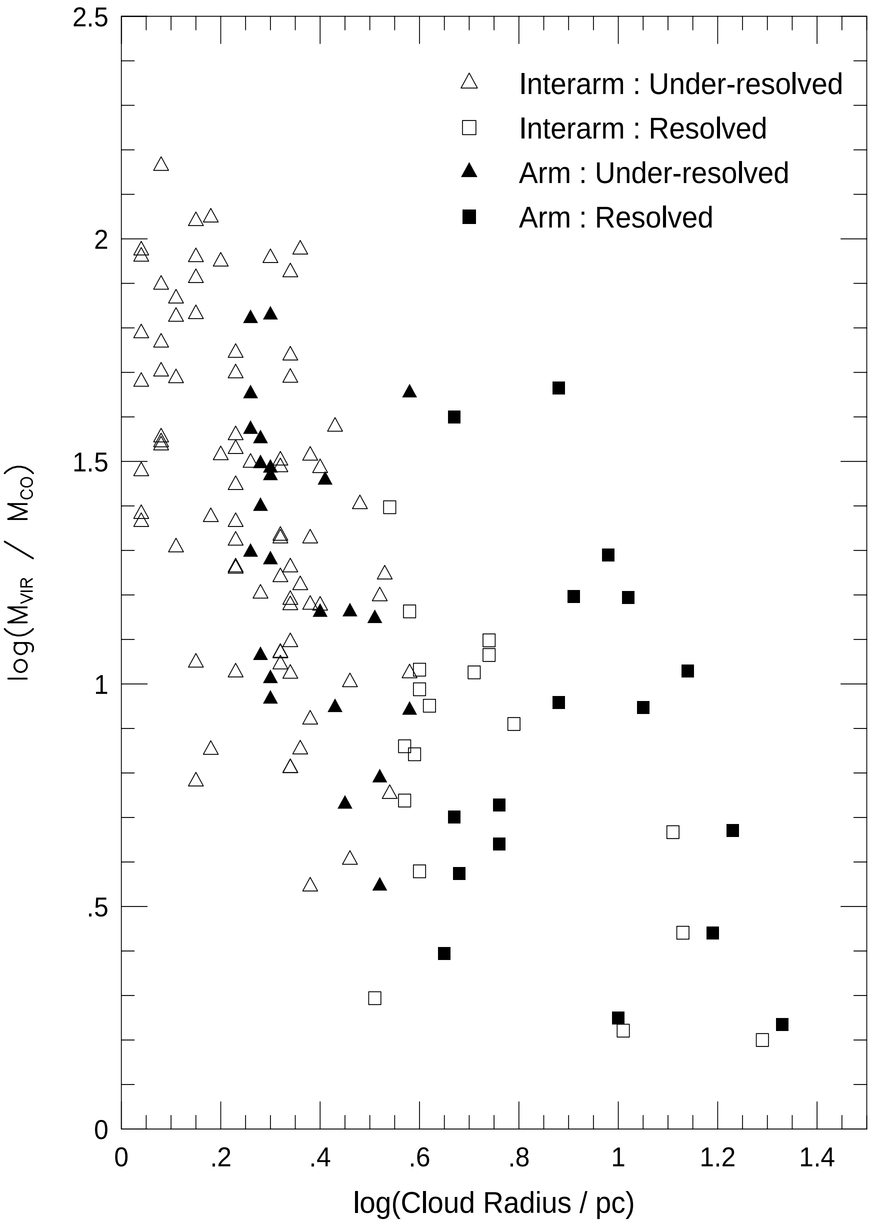

Figure 4.19: The log of the ratio of virial mass estimate to X factor mass estimate for all clouds versus log cloud radius. Note the extremely large scatter in the ratio for the under-resolved clouds. There appears to be little difference between the ratios for arm and interarm clouds.

The minimum, maximum and average line temperatures and corresponding kinetic temperatures for the cloud ensemble, as a function of cloud size and environment, are shown in Table 4.8. The two-level approximation gives slightly higher temperatures than the simplest approximation, as it includes the contribution of the excitation due to the radiation field (microwave cosmic background). Although the under-resolved clouds are included in Table 4.8, they are not included in the rest of the analysis because their peak temperatures are most likely beam diluted. The smallest line temperatures for the under-resolved clouds are at the detection limit for a line. The corresponding kinetic temperatures are extremely low and are unlikely to be physical.

The kinetic temperatures for the resolved clouds range between 5 and 12 K. The average kinetic temperature of clouds in this survey is 7 K, which is the value determined by Mead & Kutner (1988) for outer Galaxy clouds. In addition, there is no evidence of very cold (3-4 K) molecular material in the outer Galaxy as suggested by Lequeux *et al.* (1993). The difference between the temperatures of arm and interarm clouds is minor, as shown in Figure 4.20. The average temperature of the arm clouds is slightly higher, which could indicate heating of clouds by collisions or an enhanced rate of star formation. The spread in cloud temperature is larger for the arm population, which may also be explained by increased star formation for some but not all arm clouds. The small number of clouds observed and large systematic uncertainties in the calculation of kinetic temperatures make a more quantitative analysis impossible. Cloud temperatures are probably accurate to within 2-3 K (the variance between different models) and are not lower than the temperatures given here. More transitions need to be observed to provide better data on the physical properties of the clouds, so that large velocity gradient radiative transfer calculations [Goldreich & Kwan (1974) and Gellert (1995)] and micro-turbulent radiative transfer modeling [Leung (1975)] can be performed on these clouds.

Figure 4.21 is the distribution of cloud temperatures as a function of cloud radius. There appears to be a trend towards increasing cloud temperature as a function of cloud radius. It is unclear why this should be, since the dominant mechanisms for the heating of clouds in the outer Galaxy are cosmic rays, internal heating sources (young stars) and the ISRF. The heating due to cosmic rays depends only on the density of the cloud, which on average should not be significantly different for clouds with radii between 5 and 20 parsecs. It is also unlikely that the star formation efficiency (or number of stars formed per unit mass) of the clouds increases as a function of cloud radius. Observations of the star formation efficiency of molecular clouds [Mead *et al.* (1990)] as a function of mass (represented as the ratio of far-infrared luminosity to cloud mass) show that the star formation efficiency has a large scatter and is insensitive to cloud mass for clouds between 10^3 and 10^6 $M_\odot$. The contribution to the heating of the cloud by the ISRF is dependent on the surface area of the cloud (assuming a cloud opacity of $A_v > 3$ magnitudes), while the cooling of the cloud is a volume effect (mostly through optically thin molecular rotational transitions). If clouds are primarily heated by the ISRF, the cloud temperature should not increase as a function of cloud radius. It is more likely that this trend is an artifact of the relatively small sample size.

To test this hypothesis, I calculated the Kolmogorov-Smirnov (K-S) statistic [Press *et al.* (1988)] for three different models: the best fit linear model to the data, a uniformly distributed random temperature between the minimum and maximum observed temperatures and a uniformly distributed random temperature between the minimum and the 4th largest temperature. This last model regards the three highest data points as spurious outliers. The random models are controls as two random distributions will not general come from the same parent distribution. For the linear fit to be a good approximation to the parent distribution of the data, it should fit the data significantly better than the random models.

The K-S statistics for the three models are 0.559, 0.676 and 0.676 for the linear, random and random with outliers models respectively. While the linear fit is slightly better, all three models are poor fits to the data, the probability that the data and any of the models are members of the same distribution is less than 10^{-5}. If the data set is separated into arm and interarm clouds, the trend becomes slightly less significant. The K-S statistics for the models of the arm population only are 0.667, ≈ 1 and ≈ 1, respectively. While the linear model fits the data slightly better, its fit is not significant. For the interarm clouds, the K-S statistics are 0.438, 0.563 and 0.563. The linear model is only slightly better than the random distributions for the interarm clouds. As the linear fit is not a significantly better model of the data than the random distributions of points, it is likely that the trend of increasing temperature with cloud size is not physical.

Table 4.8: Statistics of Kinetic Temperatures of Clouds

T_R^* (K)

	Arm		Interarm		Total	
	Resolved	Under-resolved	Resolved	Under-resolved	Resolved	Under-resolved
Minimum	0.0.0.0.6	0.2				
2.1 5.3 2.0	5.7	2.1				
1.0.5 2.1	0.5					

T_K (K) : Thermalized Approximation

	Arm		Interarm		Total	
	Resolved	Under-resolved	Resolved	Under-resolved	Resolved	Under-resolved
Minimum	3.6	3.0	4.0	3.0	3.6	3.0
Maximum	1.0	9.5	5.4	1.0	5.5	
Average 5.9	3.7	5.3	3.4	5.6	3.5	

T_K (K) : 2-level ($n_{H_2} = 300\,\mathrm{cm}^{-3}$) Approximation

	Arm		Interarm		Total	
	Resolved	Under-resolved	Resolved	Under-resolved	Resolved	Under-resolved
Minimum	4.7	4.1	5.2	4.1	4.7	4.1
Maximum	12.3	7.0	11.7	6.9	12.3	7.0
Average	7.4	4.0.8	4.5	7.1	4.6	

Table 4.9: **Power Law Indices for Size-Linewidth Relation**

β	Recalculated β^a	Reference
0.5	0.5	Dame *et al.* (1986)
0.5	0.3	Solomon *et al.* (1987)
0.63		Leisawitz *et al.* (1990)
1.35		Chiar *et al.* (1993)[b]
1.17		Chiar *et al.* (1993)[c]

[a] From Chiar *et al.*(1990)

[b] Using ^{12}CO (J = 1 → 0) measurements

[c] Using ^{12}CO (J = 2 → 1) measurements

4.5 Size-Linewidth Relation

A correlation which is commonly examined by investigators of molecular clouds is how the observed linewidth, σ, varies with cloud radius, r. Larson (1981) determined a power law relation for cloud cores $\sigma \sim r^\beta$, $\beta = -0.5$. This relation has been observed for molecular clouds in general by many authors. The values of β for several authors are tabulated in Table 4.9. Included in Table 4.9 are the power-law indices as refit using the method of Chiar *et al.* (1994). Most values quoted in the literature for the power-law exponent are around 0.5.

The most straightforward physical consequence of this relationship is that the internal energetics of a molecular cloud are proportional to the cloud radius. The virial approximation is another relationship between cloud size and linewidth. If a cloud is in virial equilibrium, then the size-linewidth relation ($\beta = 0.5$) implies that the cloud density is inversely proportional to cloud radius. Maloney (1990) argues that $\beta = 0.5$ implies that clouds may be in pressure equilibrium; especially, if this relationship holds for clouds of all masses.

However, the physical interpretation of the size-linewidth relation is more complex than assumed by many authors. The correlation between size and linewidth

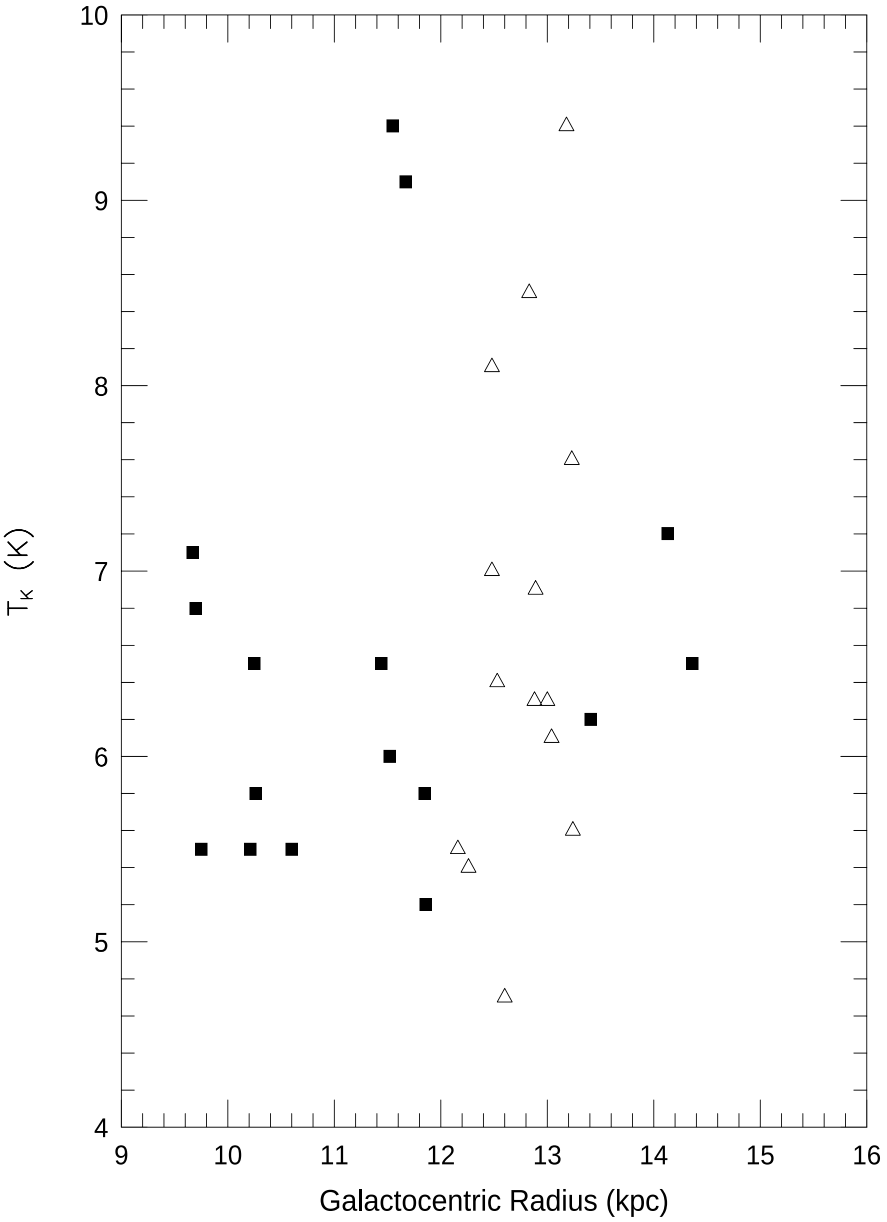

Figure 4.20: Plot of cloud kinetic temperature versus Galactocentric radius. Arm clouds are represented by filled squares, interarm clouds are unfilled triangles.

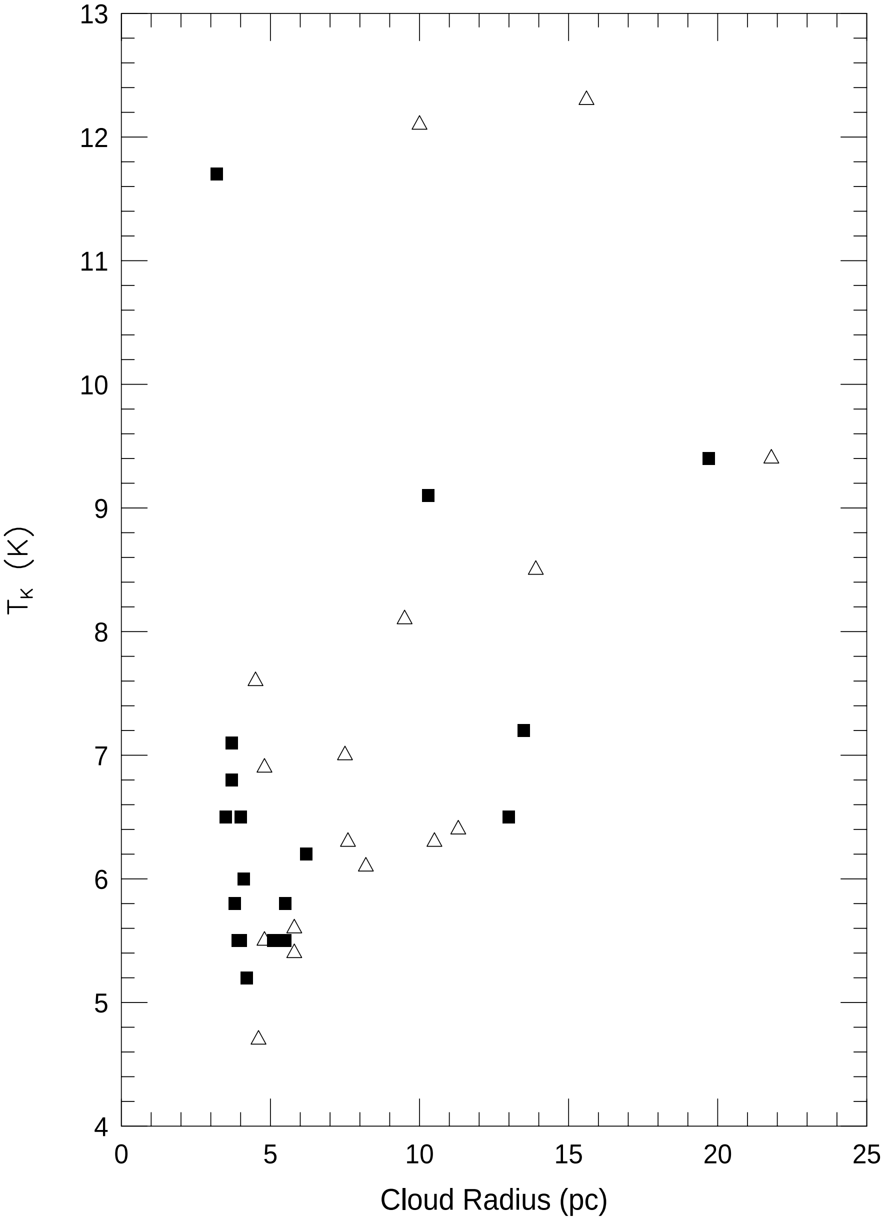

Figure 4.21: Plot of cloud kinetic temperature versus cloud radius. Arm clouds are represented by filled squares, interarm clouds are unfilled triangles.

is not very good for many clouds. In addition, many authors have used a simple least-squares fit approach to the problem. Implicit in this approach is the assumption that the abscissa of the fit (cloud radius) is error free. The radius of a cloud has a significant uncertainty associated with it for two reasons. First, the linear size of the cloud is equal to the angle subtended times the distance to the cloud. As most distances to molecular clouds are determined kinematically, there is a large uncertainty in the resultant radius, as described in Section 2.6.3. Also, the actual angle subtended by a cloud is uncertain by a beamwidth. The error is more extreme for unresolved clouds since the fractional error (error relative to cloud size) is higher.

I follow the prescription of Chiar *et al.* (1994) in calculating the best power-law fit to the size-linewidth relation. They use a fitting algorithm [Fasano & Vio (1988)] which accounts for uncertainties in both coordinates (multivariate algorithm). Essentially, the fit is done using an iterative process treating both the cloud size and linewidth as dependent variables. Figure 4.22 shows the size-linewidth relation for my data set along with the best fit power-law models to the arm, interarm and total samples of clouds. The power-law indices for the fits to all clouds, arm clouds and interarm clouds are $.65 \pm 0.85$, 1.09 ± 1.73 and $.27 \pm 1.07$, respectively. As the intrinsic scatter in the data is large, it is not surprising that the fits are very uncertain. For comparison, fits using a normal least-squares fit algorithm are shown in Figure 4.23. The values of the fits along with the K-S statistic for each fit and a comparison of the data with a random set of numbers are given in Table 4.10.

The fit for the spiral arm population is closest to the fit of Chiar *et al.* for the ^{13}CO $(\mathrm{J} = 1 \rightarrow 0)$ data. This is expected, as both samples are of spiral arm clouds and both fits are done the same way. The fit for just the interarm clouds is extremely flat and is closest to the revised fit of Solomon's data, which are part of the UMASS-Stonybrook survey. It is surprising that two very dissimilar data sets should have nearly the same power-law index. Whether the difference between the interarm and arm population relations is significant needs to be decided by further observations.

The K-S statistic of the multivariate fits is better than the statistic of the simple least-squares fit for all cloud populations. This implies that the multivariate fits are a better representation of the data, as the multivariate method allows for the scatter of data in both dimensions. However, it is more likely that neither fit is very good. Table 4.10 shows that the interarm data is fit equally well by a random distribution of points as compared to the simple least squares fit. The probability that the data and fits are from the same distribution is not significant for both least squares fitting methods. Considering the large variance in the fitting coefficients and the low likelihood that the fits are a good representation of the data, it is likely that the correlation between size and linewidth has little significance. It is likely that any correlation between the power-law coefficients for the clouds in this survey and the work of other authors is serendipitous.

While a size-linewidth relation may be valid for a particular cloud environment and range of cloud masses, it is obvious that there is no simple universal scaling relation between cloud size and linewidth. Even if a size-linewidth relationship can be determined for a particular set of clouds, it is extremely dangerous to use that relationship to determine the properties of any individual cloud. As the scatter in the data is large on a log-log scale (see Figure 4.22), any individual cloud can deviate significantly from the relationship calculated. It is even more dangerous to use the size-linewidth relationship to determine the cloud density structure or to decide whether molecular clouds are pressure bounded.

4.6 Luminosity-Mass Relation

Another pair of quantities, that is frequently examined for correlations, is the mass and CO luminosity of the clouds. Typically, the virial approximation is used to

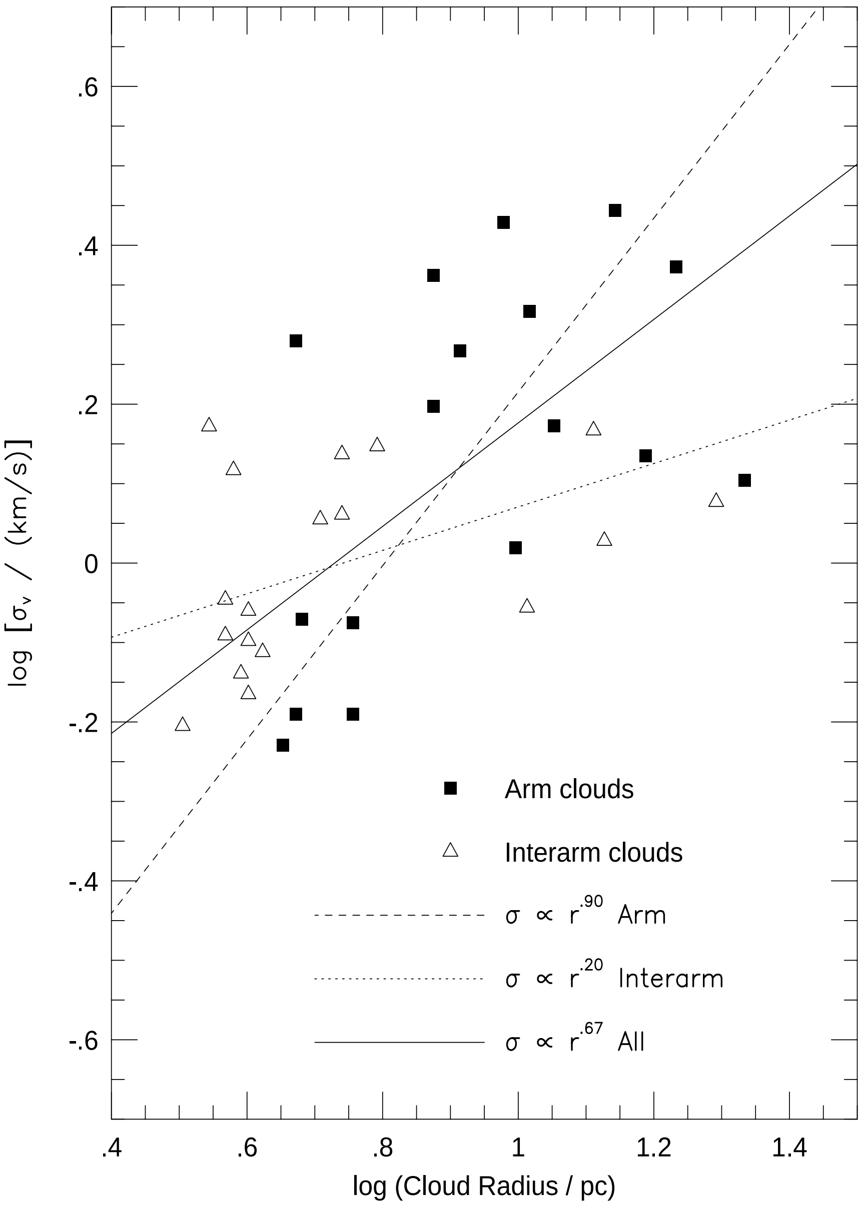

Figure 4.22: Size-linewidth relation for survey clouds. The fit is done using a multi-variate least squares algorithm.

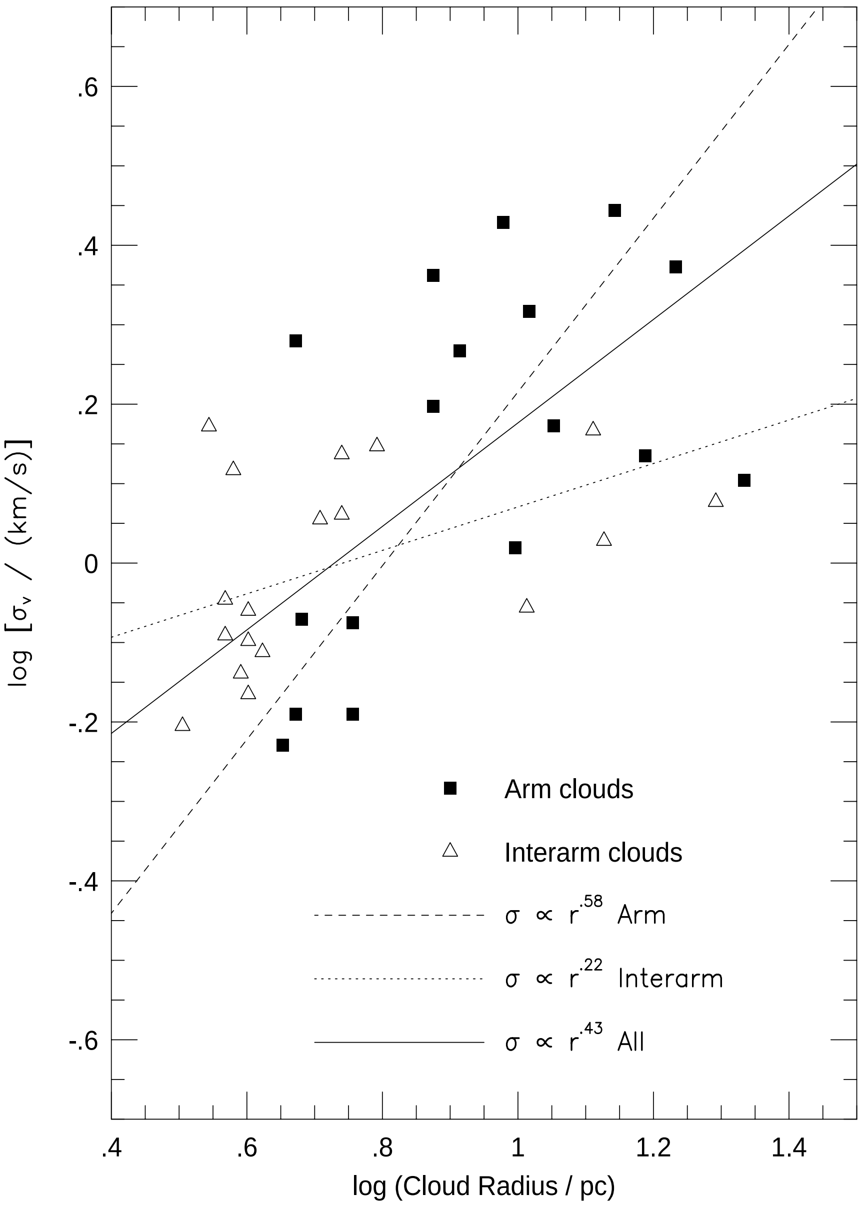

Figure 4.23: Size-linewidth relation for survey clouds. The fit is done using a normal least squares algorithm.

Table 4.10: Size-Linewidth Fit Coefficients for Different Cloud Populations

		Cloud Population		
		Arm	Interarm	All
Multivariate Fit	β	1.09 ± 1.23	0.27 ± 1.07	0.65 ± 0.85
	K-S Statistic	0.62	0.56	0.55
Simple LSQ Fit	β	0.58 ± 0.22	0.22 ± 0.11	0.43 ± 0.11
	K-S Statistic	1.00	0.89	1.00
Random Distribution	K-S Statistic	1.00	0.85	1.00

determine the mass for this relation. It makes little sense to relate the CO luminosity to the cloud mass determined from the luminosity. If the cloud mass and luminosity are linearly correlated, then the cloud mass can be reasonably approximated by the CO luminosity. The slope of the correlation is the X factor. Assuming that the virial approximation holds for the majority of the clouds used in the analysis, deviations from a linear relationship indicate that the CO luminosity cannot be used to estimate cloud masses.

The luminosity-mass relation is another manifestation of the size-linewidth relation; therefore, it gives no new insight on the physical properties of the clouds. To illustrate the link between the two relations consider the virial mass of the cloud

$$M_{VIR} = \alpha \langle \Delta v \rangle^2 r \tag{4.3}$$

where the cloud velocity dispersion has been rewritten in terms of the observed FWHM, Δv, and the cloud luminosity

$$L_{CO} = \langle I \rangle A = \langle T \Delta v \rangle \pi r^2 \tag{4.4}$$

where the average intensity has been written in terms of the peak temperature, (T), and linewidth (Δv) of the cloud, and the area is calculated using the effective radius (r) of the cloud. Making the assumption that the peak temperature and linewidth of the cloud are uncorrelated,

$$\frac{M}{L} = \frac{\alpha\langle\Delta v\rangle^2 R}{\langle T\rangle\langle\Delta v\rangle\pi R^2} = \frac{\alpha}{\pi\langle T\rangle}\frac{\langle\Delta v\rangle}{R} \tag{4.5}$$

The luminosity-mass relation is just another way to relate the size and linewidth of the cloud. For completeness, the best power-law fits to log cloud mass versus log cloud luminosity for the resolved clouds are shown in Figure 4.24.

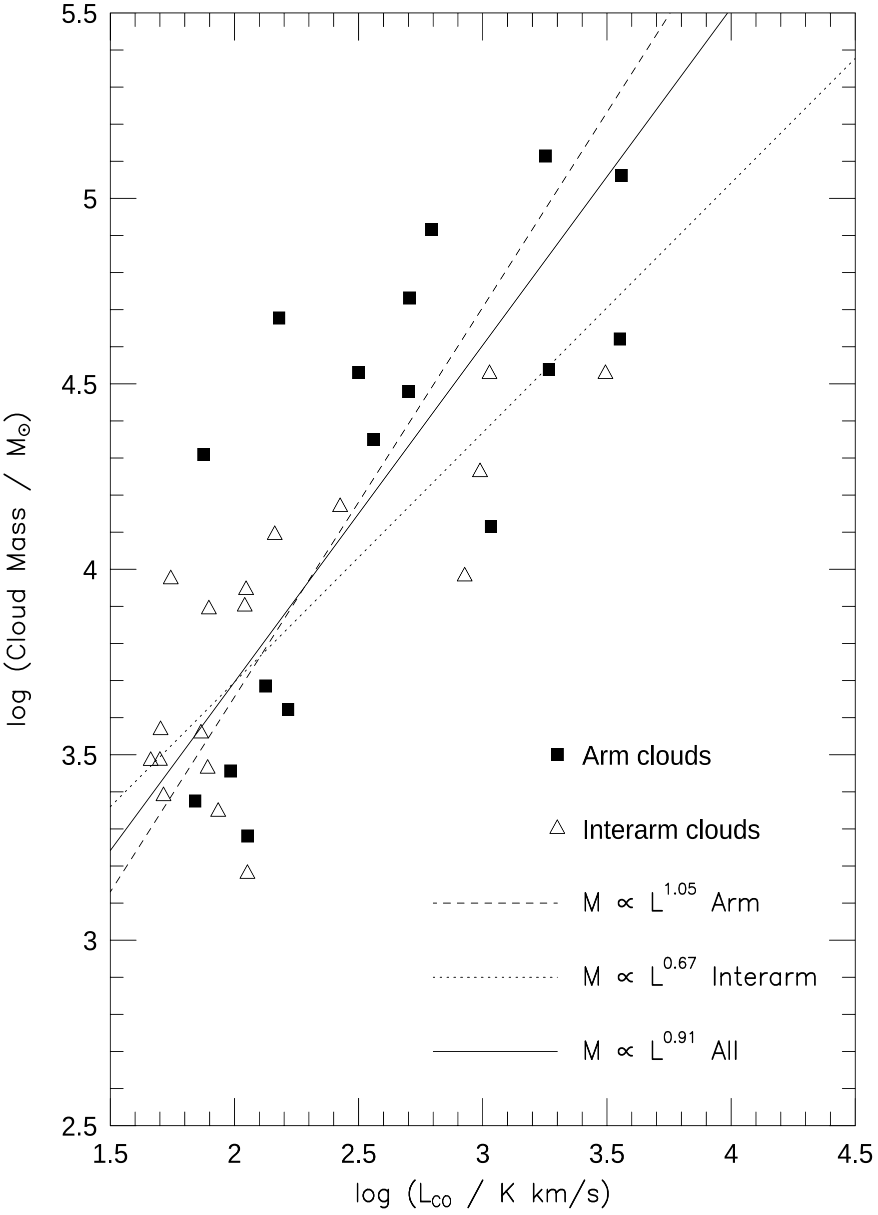

Figure 4.24: **Plot of log cloud mass versus log CO luminosity. The best power law fits are shown for the arm, interarm and total cloud populations.**

CHAPTER 5
TOTAL MOLECULAR MASS OF THE OUTER GALAXY

Determining the molecular mass content of the outer Galaxy is an extremely important problem. However, very little work has been done in estimating the molecular mass of the outer Galaxy. A full survey of the outer Galaxy in ^{12}CO ($J = 1 \rightarrow 0$) seems a straightforward solution to the question. However, a survey with sufficient sensitivity and resolution to detect potentially weak emission from outer Galaxy clouds, while having enough spatial coverage to sample a significant portion of the outer Galaxy, is currently impractical due to constraints on equipment sensitivity, observing time and the lifetime of a typical graduate student. Several mass estimates have been made of the total molecular mass of the outer Galaxy. In this chapter, I will examine these estimates and discuss how they should be modified based on the observations interpreted in this thesis. In particular, two major modifications will be suggested. The first modification is taking into account the mass of small clouds in the outer Galaxy. The second modification is using the virial theorem to calculate the masses of the clouds instead of the $N(\mathrm{H}_2)$ to I_{CO} conversion (X factor) mass estimate. Section 5.1 will describe in some detail the previous mass estimates. In Section 5.2, I will determine the modifications to the previous estimates.

As mentioned in Chapter 1, molecular material is not gravitationally significant on a Galactic scale. However, recent observations by Lequeux *et al.* (1993) have discovered CO in absorption along several lines of sight in the outer Galaxy. Their initial interpretation of the data suggested that small, very cold molecular clouds could contain up to five times the mass of HI in the outer Galaxy. They further suggested that cold molecular gas could be a component of dark matter. The authors have since modified their original interpretation and believe that cold molecular gas is not a significant mass component in the outer Galaxy [Lequeux (1995)]. Nonetheless, the amount of cold molecular in the outer Galaxy is a very interesting question. At the end of Section 5.2, I will determine a very liberal and quite speculative upper limit to the total mass contained in small, cold clouds. In my opinion, cold molecular clouds are not a gravitationally significant component of the total mass of the outer Galaxy.

5.1 Previous Estimates

Two widely-quoted estimates of the total molecular mass have been made. One estimate has been made by Digel *et al.* (1990) using the Columbia (CfA) 1m and Bell Labs 7m telescopes to survey a large region in the outer Galaxy. The second estimate is by Wouterloot *et al.* (1990) using data from the SEST 15m and IRAM 30m telescopes. Both groups estimate the total molecular mass of the outer Galaxy to be 6×10^8 $M_\odot$ (not accounting for the mass contribution due to helium) [Dame (1993)]. It is somewhat surprising that their estimates agree so well, considering the very different methods employed and the large inherent uncertainty involved in approximating the total molecular mass of the outer Galaxy using an incomplete data set. However, both groups are essentially looking at the same population of clouds; therefore, the agreement between the estimates is not as amazing as it first appears. Digel's estimate preferentially includes the contribution to the largest and brightest molecular clouds while Wouterloot's estimate is based on the distribution of star forming clouds.

Before determining if information from this thesis can be used to improve the current mass estimate, it is fruitful to discuss how previous estimates were determined. Wouterloot's group used the IRAS point source catalog to identify candidates for star forming regions based on the IRAS colors of the sources. Each candidate was observed in the ^{12}CO ($J = 1 \rightarrow 0$) transition. Using the kinematic distances of the observed CO lines, they determined the spatial distribution of their 1302 sources identified in the outer Galaxy. The detections were binned as a function of Galactocentric radius. The molecular surface density at R_0 was calculated using the results of Grabelsky *et al.* (1987) and Sanders *et al.* (1984). The surface density as a function of R, $\sigma(\mathrm{H}_2, R)$, was approximated by scaling $\sigma(\mathrm{H}_2, R_0)$ by the surface density of CO detections as a function of Galactocentric radius.

Digel's approach is more straightforward. The results of the CO survey by Digel *et al.* (1990) were converted to a mass density using the prescription of Grabelsky *et al.* (1987)

$$\rho(R, z) = 6.17 \frac{X}{2.8} T_R(l, b, v) \left| \frac{dR}{dv} \right|^{-1} \mathrm{M}_\odot \ \mathrm{pc}^{-3} \tag{5.1}$$

where $\rho(R, z)$ is the molecular mass density as a function of Galactocentric radius and height, z, above the Galactic plane, T_R is the CO brightness temperature, and $X/2.8$ is the X factor conversion ratio scaled to the inner Galaxy X factor of Grabelsky. Digel *et al.* used a conversion factor four times that of the inner Galaxy; this value is a factor of two greater than the X factor used by Mead & Kutner (1988). The calculated mass density was then used to determine the total molecular mass in the outer Galaxy. As I will also use the method of Grabelsky for a mass estimation, it will be further discussed in Section 5.2.1.

Both mass estimates neglect the contribution of the smallest and coldest clouds. Wouterloot's method is dependent on the distribution of star forming clouds in the outer Galaxy. If the number density of star forming clouds decreases as a function of R, then the Wouterloot *et al.* value will underestimate the total mass. It can be argued that their value is an underestimate, even if the distribution of star forming clouds is the same in the inner and outer Galaxy. If there exists a significant number of small clouds in the outer Galaxy, then the contribution due to these clouds will not be included in Wouterloot's estimate. The exclusion of the small cloud contribution is not due to the star forming characteristics of small clouds. Instead, it is the direct result of using previous CO surveys, which neglect the mass contribution of small clouds in the inner Galaxy to convert the number density of star forming clouds to a molecular surface density in the outer Galaxy, where the mass contributed by small clouds is significant.

In principle, Digel's estimate should include the small/cold cloud component. However, the small cloud contribution can be diminished as part of the data reduction process. If weak signals are included in the baseline regions, this will artifically raise the baseline and weaken the contribution of that signal to the CO intensity at that particular velocity and position, $T_R(l, b, v)$. It is difficult to determine the error introduced by baselining the data, as the distribution of weak signals (small/cold clouds) must be known. An example of how baselining the data affects mass estimates is discussed in Section 5.2.1.

A more important consideration is whether the mass contribution from small clouds can be reliably calculated using Grabelsky's method, which uses the X factor to convert CO luminosity to mass. As argued in Chapter 4, the masses of small clouds in my work are best estimated using the virial approximation. Using CO luminosities to calculate the mass of a small cloud seriously underestimates the mass of the cloud; that is, the small clouds are "under-luminous" by more than the factor of 4 that Digel *et al.* (1991) suggest (see Figure 4.21).

5.2 Modifications to Total Mass Estimates

The data set described in this work is the most sensitive, full beamwidth sampled survey (albeit small survey) of molecular material in the outer Galaxy at the current time. The observed cloud distribution in this thesis is an unbiased sample of molecular clouds above the completeness limit of the survey as described in Section 2.7. There are a significant number of small clouds in the survey volume. The contribution of these clouds to total mass estimates has been previously overlooked and will be examined in this section. Before using the results of this data set to make any conclusions about the total amount of molecular mass, it is important to determine how representative the data set is of the entire population of molecular clouds in the outer Galaxy.

If the current survey region is a representative slice of the outer Galaxy, then the mass measured in the survey region can be scaled by the ratio of the survey volume to the total volume in the outer Galaxy to determine the molecular mass in the outer Galaxy. It is unlikely that the survey region is truly representative of the entire outer Galaxy. The survey region contains a strong spiral arm feature, the 13 kpc arm. However, unlike the CO luminous clouds surveyed by Digel and Wouterloot, this survey also contains a significant population of underluminous clouds which may be prevalent in the outer Galaxy. My best guess is that the region surveyed fits somewhere between regions whose mass is dominated by large, actively star-forming clouds, and regions where most of the mass is contained in small clouds. Since no large scale survey sensitive enough to determine small clouds has been conducted, it is impossible to determine the fraction of mass contained in each type of region: massive star-forming, quiescent large cloud dominated and small cloud dominated.

With the caveat that the region surveyed is not truly indicative of the entire outer Galaxy, I will make mass estimates of the entire outer Galaxy. These estimates should be an improvement over previous estimates as the contribution of small clouds to the total mass is included. The next subsection will use the method of Grabelsky to estimate the total molecular mass in my survey. In addition, some cautions, about using the baselined spectra (as opposed to the clouds detected) to determine mass estimates, will be presented. I will show that the results of the mass estimate are very sensitive to the baselines fit.

5.2.1 Influence of Baseline on Results – A Case Study

In determining the molecular mass using the method of Grabelsky, the properties of individual clouds are not used. Instead, the spectra for each position are used to determine the mass density along that line of sight. The total mass is then determined by integrating the density for all Galactocentric radii (velocities) and positions in l and b observed. In terms of the molecular hydrogen column density, the mass is

$$M = \sum_{\text{All Positions}} \sum_{\text{All channels}} (2.76\, m_{\mathrm{H}_2}) \frac{dN_{\mathrm{H}_2}(v)}{dv} (\theta d(v))^2 \, \Delta v \tag{5.2}$$

Rewriting the equation in terms of observable quantities,

$$M = \sum_{\text{All Positions}} \sum_{\text{All channels}} 2.21\, X\, T_R^*(v)\, (\theta d(v))^2 \, \Delta v \tag{5.3}$$

where the sums are over all positions and all velocities, $2.76\, m_{\mathrm{H}_2}$ is the average mass per hydrogen molecule (accounting for the contribution due to helium), $\theta = 60$" is the angular spacing between positions, $d(v)$ is the heliocentric distance as a function of velocity, X is the X factor, and $N_{\mathrm{H}_2}(v)$ is H_2 column density as a function of velocity. To illustrate the effects of baselines on this method of mass determination, I describe an initial effort to reduce the data of this survey.

In the process of analyzing the data, I initially baselined the spectra by hand. I was interested in identifying weak emission and took special care to avoid potential signals that had low signal-to-noise. As a result, channels containing only noise were avoided in the process. The resultant baselines were artifically lowered by the exclusion of spectrum channels with positive values due to noise. This bias is further discussed in Section 2.3.1. The offset from the best baseline and the one fit (assuming the same order baseline is fit) is on average less than of a hundredth of a Kelvin for any one scan. If the same spectrum has two different order baselines fit, then the difference between resultant spectra will be larger. The cumulative effect of this bias to the composite spectrum or any quantity measured using the sum of all spectra is significant.

The bias introduced into the composite spectrum is obvious in Figure 5.1, which compares the composite spectrum of the data, baselined by hand, to the composite of the data, processed using the automated baseline algorithm. For both composites, all channels are greater than zero for the velocities studied. This indicates that emission is ubiquitous in the survey region. The composite of the by-hand baselined spectra has a positive DC offset of about .01 K when compared to the automated composite. If the by-hand composite is interpreted without considering the bias, it implies that there are a large number of small clouds in the outer Galaxy which could contribute a significant mass fraction.

Using the method of Grabelsky, the total mass of the region calculated from scans baselined by hand is 4.70×10^5 $M_\odot$. The unbiased (auto-baselined) mass estimate is 8.5×10^4 $M_\odot$. Scaling the mass results by the fraction of the outer Galaxy occupied by the survey, 1.5×10^{-3}, the total molecular mass of the outer Galaxy is 5.7×10^7 $M_\odot$ for the unbiased value and 3.1×10^8 $M_\odot$ for the biased estimate. Using the biased baselined data results in an overestimate of the total mass of the survey region. It is also possible to bias the data, so that the the mass is underestimated through biasing. If the regions used to fit baselines include real signals, then the baseline will be artifically raised. This will underestimate the peak temperatures of signals and reduce the mass estimated using the method of Grabelsky.

A better method to identify molecular mass is to measure the mass of individual clouds using the virial theorem. For objects above the detection limit, this method should be more accurate as it does not depend on the specifics of the data reduction. Also, the X factor estimate is strongly dependent on the properties (temperature, metallicity) of the clouds observed. Since there is a large scatter in the

$L_{\rm CO}$ to M_{VIR} ratios (see Figure 4.24), it is obvious that a single X factor does not apply to all clouds observed.

5.2.2 Corrections to the Total Molecular Mass

From Section 4.3, the total virial mass of the survey region is 1.0×10^6 $\mathrm{M}_\odot$, which is 2.2 times greater than the X factor mass estimate of Section 5.2.2 and is 6.2 times greater than the X factor mass estimate for individual clouds. If the survey region was a truly representative sample of the outer Galaxy, the obvious result is that the best estimate of the total molecular mass of the outer Galaxy is 6.7×10^8 $\mathrm{M}_\odot$, which is in good agreement with previous estimates. This agreement is slightly misleading as the previous estimates were of the molecular mass to R = 20 kpc, while I can only estimate the total mass within R = 16 kpc (the largest Galactocentric radius covered in the survey). Therefore, my mass estimate would be increased by the mass of material between R = 16 kpc and R = 20 kpc. It might seem appropriate to scale the mass that I have calculated by the distribution of CO detections as a function of R in Wouterloot group's work. From Wouterloot's distribution of sources as a function of R, it appears that the amount of mass between R = 16 and R = 20 kpc is a small fraction of the total mass. However, my data set is comprised of a different population of clouds whose distribution may or may not follow the distribution of star forming clouds.

Another possible tactic for improving the estimate of total molecular mass is to use my results for small and CO underluminous to modify the estimates of Digel and Wouterloot. The same two assumptions are implicit in this analysis: my survey region is a representative sample of the outer Galaxy, and the mass fraction of small, CO underluminous clouds is a significant portion of the total molecular mass. The last assumption has some justification; the virial mass estimate from my survey region indicates that small, underluminous clouds can make up a significant

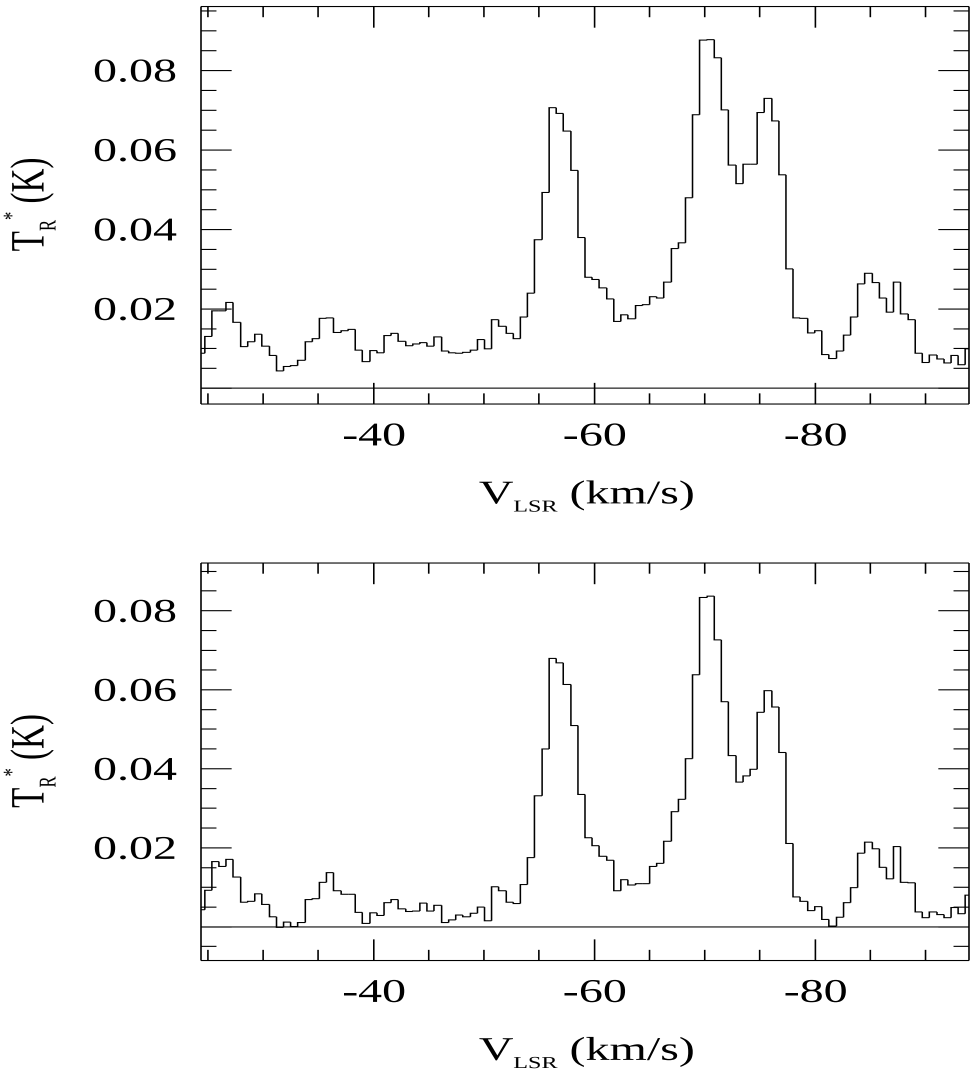

Figure 5.1: **Composite spectra of entire data set. The top spectrum is the data baselined by hand. The lower spectrum is the data baselined using the automated baseline algorithm described in Section 2.3.2.**

mass fraction. To include this contribution, it is necessary to make a guess about the fraction of mass not accounted for in the previous estimates.

Instead of a best guess, I'll list some possibilities for the total mass based on how much mass is accounted for by small and CO underluminous clouds. It is very unlikely that contribution of small, CO underluminous clouds is insignificant. If they occupy the same mass fraction as more luminous (star forming) clouds, then the mass estimate for the outer Galaxy should be approximately $1.2 \times 10^9\,\mathrm{M}_\odot$. It is possible that the fraction of mass contained in underluminous clouds increases as a function of R due to decreased cloud temperatures and metallicities.

If the mass distribution of the outer Galaxy is dominated by larger CO underluminous clouds similar to the large clouds described in this thesis, then previous mass estimates would be further increased. If most of the mass in the survey regions of Digel is contained in underluminous CO clouds, then the most appropriate mass estimate would be determined by scaling his estimate by the actual mass of the clouds using the virial theorem. Assuming the clouds are similar to the ones in my survey, Digel's mass estimate should be increased by a factor of three. The factor of three is determined from the ratio of the total virial mass in my region to the X factor mass estimate of the region, which is 6. Digel's X factor estimates should be a factor of two higher as he uses a larger X factor. In the limit of the majority of the molecular mass of the outer Galaxy being contained in CO underluminous clouds, the total molecular mass of the outer Galaxy would be $1.8 \times 10^9\,\mathrm{M}_\odot$, which is approaching the HI mass estimate of the outer Galaxy [see Henderson *et al.* (1982), Wouterloot *et al.* (1990) and the discussion in Dame (1993)].

If the small, CO underluminous clouds contain most of the molecular mass, then previous estimates have seriously underestimated the total molecular mass of the outer Galaxy. It is doubtful that most of the mass is contained in the small clouds, as the interarm regions in my survey only contain twice as much mass in small clouds as in large clouds. In addition, not all regions in the outer Galaxy are as devoid of molecular material as the interarm regions are. However, if small clouds comprise the majority of molecular mass in the outer Galaxy, then the general outer Galaxy mass distribution most closely resembles the interarm regions of my survey without the large clouds. The virial to X factor ratio for the small interarm clouds is approximately 20. An upper limit to the molecular mass contained in small clouds in the outer Galaxy would be $1.2 \times 10^{10}\,\mathrm{M}_{\odot}$. Remember that this estimate makes the assumption that there is a pervasive underlying small cloud population which follows the distribution of larger, warmer clouds. This estimate is a very liberal upper limit; the ratio of molecular to atomic gas would be about 10. It is highly unlikely that this much mass is contained in small cold clouds; therefore, cold molecular clouds are a poor dark matter candidate.

There is no evidence of a very cold ($T_K < 4\,\mathrm{K}$) cloud component. The lowest estimated temperature for a resolved cloud in this survey is 4.7 K. It is possible that the smaller clouds have low kinetic temperatures; however, it is more likely that the low line temperatures observed for these clouds are caused by beam dilution. The results of this work do not support the existence of a very cold molecular cloud population in the outer Galaxy for the physical conditions, arm and interarm, and Galactocentric radii covered. In Chapter 7, I will describe a method for finding cold molecular clouds if they exist.

CHAPTER 6
DISCUSSION OF RESULTS

Three main areas have been investigated in this work. In this chapter, I will analyze some of the results in more detail. The 13 kpc arm results are reasonably straightforward and will not be interpreted further. The remaining areas, the physical properties of individual molecular clouds as a function of environment and the total molecular mass of the outer Galaxy, merit further discussion.

6.1 Individual Cloud Properties

In this work, the properties of molecular clouds have been measured as a function of their environment. An interesting result is that the kinetic temperatures of molecular clouds do not vary significantly as a function of cloud environment. It might be expected that spiral arm clouds would be significantly warmer than their interarm counterparts, because the density of young bright stars (OB associations) is higher in spiral arms. If star formation is taking place inside the cloud, then the embedded objects will also heat the cloud. Star formation is enhanced for clouds in spiral arms, as the proposed triggers for massive star formation, cloud-cloud collisions, spiral density waves, and star formation and supernova in adjacent clouds, are more prevalent. Another major source of energy input is cosmic rays. It is not expected that the density of cosmic rays should be a function of environment; however, it may be a weak function of Galactocentric radius [Bloemen *et al.* (1986)].

As the cloud temperature does not vary with environment despite the chance for more heating in a spiral arm, some tentative conclusions can be made about heating of the clouds. The first is that cosmic rays play a significant role in most of the clouds observed. The second conclusion is that the general environment of a cloud does not affect the temperature of a cloud. It is possible that spiral arm clouds will have greater temperatures due to proximity of OB associations or other heating sources; however, heating of clouds is a very local effect and the variations between individual clouds are much greater than the trend in temperature due to cloud environment.

The cloud size spectra and size-linewidth relation, as a function of environment, calculated in this work are markedly different than the results of most inner Galaxy studies. Some of the difference can be attributed to the inherent difficulties in measuring properties of individual clouds in the inner Galaxy. In addition, the results are in much better agreement if the data is interpreted using the same method of determining cloud mass and definition of cloud size. In the study of Scutum Arm clouds by Chiar *et al.* (1994), individual clouds are identified and properties measured in a fashion very similar to this work. It is not surprising that the size-linewidth relation determined in their study is in good agreement with the arm population result of this work.

The distribution of cloud sizes indirectly provides information on how the clouds form, since the cloud size spectrum is determined by the physical processes that govern the life cycle of the clouds. The size distributions cannot be directly related to the cloud formation mechanisms in each environment, as the effects of cloud destruction and fragmentation must also be considered. The size spectra presented in this work could be used to check detailed models of cloud formation and destruction. This analysis is currently beyond my capabilities and will be deferred to the future.

From the arm and interarm size spectra, it is obvious that clouds have very different evolutions in the arm and interarm regions. The mass of the spiral arm population is dominated by the largest clouds, while all clouds contribute roughly equal fractions of mass in the interarm regions (see Figure 4.15). All current theories of cloud formation (see Section 1.4.4) use spiral arms to facilitate cloud formation.

However, cloud formation by aggregation and condensation can take place without a spiral arm feature. Aggregation will occur in interarm regions but at a much lower rate, since the number density of clouds is less in interarm regions. Condensation from HI super-clouds can also occur outside of spiral arms. There is plenty of HI in the interarm regions, and supernova and other energy sources can provide the necessary trigger to cause the super-cloud to become unstable, collapse and fragment. It is likely that both condensation and aggregation play some role in cloud formation. Currently, it is an open and much debated question which mechanism is dominant. Another possible way to explain the mass distribution is to have most of the clouds form in a spiral arm. Then, these clouds go through their life cycle, forming stars at some time. Star formation probably disrupts the cloud, but does not evaporate it. It is hard to imagine how an object with a mass of $10^4 - 10^5$ $\mathrm{M}_\odot$ would be obliterated. The remnants of the parent cloud would then persist as lower mass fragments; that is, smaller clouds. These fossil clouds would remain after the spiral arm density wave passes by and could live indefinitely.

Any of the scenarios described in the previous paragraphs can accurately describe the observed cloud distribution. At the current time, no model is sufficiently detailed to predict the observed distribution. I believe that the cloud destruction process needs to be investigated in further detail to determine what happens to the remnants of GMCs after a period of massive star formation.

6.2 Total Molecular Mass of the Outer Galaxy

The most exciting result of this work is that small ($r < 5\,\mathrm{pc}$) molecular clouds do comprise a significant fraction ($\sim 30\%$) of the total molecular mass of the outer Galaxy. In addition, a large portion of the molecular mass of the outer Galaxy is probably contained in CO underluminous clouds. The contribution due to small and underluminous clouds has been missed in previous mass estimates (see Section

5.1). The fraction of mass contained in small and underluminous clouds is currently unknown, but it is plausible that they increase the total mass by a factor of two or more. The actual increase depends on the fraction of the outer Galaxy which is more similar to the survey region in this work than regions where warmer, star forming clouds reside. My best estimate of the total molecular mass of the outer Galaxy is between 1 and 2×10^9 $M_\odot$.

While this is a large increase in the estimated molecular mass, molecular clouds still make up a small fraction of the total mass in the outer Galaxy. It is unlikely that molecular clouds in any form are a viable dark matter candidate. Unless there exists a significant population of very small and/or very cold clouds, molecular clouds are not a significant contributor to the gravitational potential of the outer Galaxy. In my work as well as the surveys of Mead (1988) and Digel (1990), there is no evidence of such a population. Four absorption lines have been detected by Lequeux *et al.* (1993) along two lines of sight in the outer Galaxy; this is clearly not enough information to make an estimate of the contribution of cold molecular material. More sensitive observations will be able to make a final definitive statement about the role of cold, molecular material.

Using my estimates for the total molecular mass, the masses of atomic and molecular gas in the outer Galaxy are comparable. In fact, the ratio of molecular to atomic gas for the outer Galaxy is 0.25-0.45 [Dame (1993)]. This is a similar situation to the inner Galaxy (mass fraction 0.75, [Dame (1993)]), assuming that the molecular mass of the inner Galaxy is correct. I must caution the reader that this result is very speculative. Not only are the corrections to total outer Galaxy molecular mass uncertain, but also the HI mass estimates for both the inner and outer Galaxy [Dame (1993)]. The next paragraph will examine the possible significance of this result.

Roughly equal mass fractions in each environment suggests that the process which creates molecular mass out of atomic gas, the formation of molecular clouds by self-shielding clumps in the atomic gas, has the same efficiency in the inner and outer Galaxy. This does not imply that the ratio of molecular to atomic gas is the same everywhere in the Galaxy. The molecular ring, centered on R = 5 kpc [Solomon *et al.* (1985)], is one region where the ratio of molecular to atomic gas is higher. In addition, it does not imply that the physical conditions (temperature, pressure, radiation field) are the same; it is obvious that they are not. However, the fraction of material that can be shielded from UV radiation, which will dissociate molecules, is roughly the same in the inner and outer Galaxy. A measure of the shielding of molecules as a function of environment is the ratio of the metallicity, Z, to the radiation field, ϕ [Elmegreen (1993b)]. The average value of this ratio for the inner (IG) and outer Galaxy (OG) must be roughly equal

$$\frac{Z_{IG}}{\phi_{IG}} \approx \frac{Z_{OG}}{\phi_{OG}} \tag{6.1}$$

for equal fractions of atomic and molecular gas to exist.

Another question to investigate is : should the molecular mass estimates of the inner Galaxy be revised? Much of the work done in the inner Galaxy has used the X factor to derive masses. However, the virial and X factor estimates are in much better agreement for inner Galaxy clouds. This better agreement can be attributed to the higher average cloud temperatures and the higher metallicity in the inner Galaxy. It is unlikely that the X factor mass estimates of inner Galaxy clouds need to be scaled in the same fashion as the outer Galaxy estimates.

A significant portion of the mass in the outer Galaxy is contained in small clouds. It can be argued that the contribution of small clouds to the inner Galaxy mass estimate has been underestimated, as it is virtually impossible to identify and isolate small clouds in the inner Galaxy data due to crowding and blending together of clouds in velocity space. Assuming that the volume density of small clouds in the inner and outer Galaxy is similar, it is unlikely that small clouds contribute a significant fraction of the molecular mass in the inner Galaxy, as most of the mass observed is in GMCs and the volume available in the inner Galaxy (about 50 kpc^3) is much smaller than the outer Galaxy.

CHAPTER 7
SUMMARY AND FUTURE WORK

7.1 Summary

The work described in this thesis can be divided into three main sections: 13 kpc arm results, results of the investigation of individual molecular cloud properties and revisions to the total molecular mass estimates. Each aspect of this work looks at a different size scale for the distribution of molecular material in the outer Galaxy. I started with the large-scale structure of the region I surveyed, then examined the properties of the molecular clouds on an individual basis. Using the results of the first two parts of the investigation, I have made an estimate of a reasonable correction to the total molecular mass of the outer Galaxy.

7.1.1 13 kpc Arm

The 13 kpc arm first identified by Mead (1986) is readily apparent in my data set. A local estimate of the centroid of the arm is R = 12.7 kpc and the FWHM width of the arm is 1.3 kpc. Two different populations of clouds are recognized: arm and interarm. The arm population consists of all clouds between R = 12.0 and R = 13.3 kpc and is characterized by an abundance of large ($M > 10^4$ $M_\odot$) molecular clouds. The interarm population is clouds at all other Galactocentric radii. The interarm population consists primarily of small clouds.

The width of the 13 kpc arm, as measured in this work, is larger than measurements of other spiral arms in the Milky Way and other galaxies by a factor of 2-6. The discrepancy between the 13 kpc arm measurement and other measurements is probably due to the small length of the arm surveyed and not the inclusion of the distribution of small clouds in the width estimate.

7.1.2 Properties of Individual Clouds

In the 0.8 square degrees surveyed, 137 individual clouds have been identified. Unfortunately, only 35 of the clouds have been observed with sufficient resolution and sampling to accurately calculate cloud radii. The estimates of the cloud sizes for the remaining clouds are good to within a factor of two. Cloud temperatures have been estimated using a two-level approximation for the ^{12}CO ($J = 1 \rightarrow 0$) excitation temperature. The kinetic temperatures of the clouds are between 4.7 and 12.3 K. These temperatures agree with the kinetic temperatures calculated for outer Galaxy GMCs by Mead (1986).

The size spectra of the arm and interarm populations are markedly different. The power-law index, ξ, for the size spectra of arm clouds is -0.7, while for interarm clouds the power-law index is -1.2. These results are not in agreement with the size spectrum estimate of Terebey *et al.* (1986) or any of the inner Galaxy results. This discrepancy is probably due to the small number of clouds in both the current and Terebey *et al.* data sets and the vastly different means of measuring cloud properties, that the inner Galaxy studies employed.

I have also examined the size-linewidth relation for the resolved clouds in the survey. The best-power law fits to the size-linewidth relation are 1.1 for the arm population and .3 for the interarm population. The arm fit agrees with a similar analysis of the Scutum Arm clouds by Chiar *et al.* (1994). However, the data can be modeled equally well with a random distribution of points, which casts serious doubt on the usefulness of the size-linewidth relation. As the mass-luminosity relation contains the same physical content as the size-linewidth relation, its utility is also in doubt.

The masses of the clouds are calculated using the virial approximation. This appears to be reasonable as the largest clouds are similar in size to GMCs, while the smaller clouds are more like dark globules than the high latitude (diffuse) clouds of Blitz *et al.*(1984). The virial masses of the clouds range between 2×10^2 and 1.3×10^5 $M_\odot$. The masses of the smallest clouds are very uncertain but should be good to within a factor of two or so. Most of the mass in the survey region is contained in large ($r > 5$ pc) clouds, but 32 % of the mass is contained in smaller clouds.

7.1.3 Corrections to the Total Molecular Mass of the Outer Galaxy

There have been two previous estimates of the total molecular mass of the outer Galaxy. The two estimates are in amazing agreement considering the different methods used. The total molecular mass is estimated to be $6 \times 10^8 \, M_\odot$. Each method has a bias towards large clouds and depends on the conversion factor (X factor) between H_2 column density and CO integrated intensity for the mass calculation. Using the results of the mass estimates of my survey region to account for the contribution due to small clouds and correcting for the difference between virial and X factor mass estimates for underluminous clouds, I estimate that previous mass estimates should be scaled upward by a factor of 2-3. My estimate for the total molecular mass estimate of the outer Galaxy is $1 - 2 \times 10^9 \, M_\odot$, which is comparable to the atomic gas mass in the outer Galaxy.

I find no evidence of an abundance of cold ($T < 5$ K) molecular material. It is doubtful that cold molecular clouds make up a gravitationally significant portion of the total mass of the outer Galaxy. It is less likely that cold molecular material is a viable dark matter candidate.

7.2 Future Work

In any quest for knowledge, asking a question and attempting to find an answer does not guarantee a solution, but it certainly guarantees that there will be more questions to answer. This is definitely the case with this work!

7.2.1 Applications of Data to Cloud Formation Theories

Hopefully, the cloud size distributions as a function of spiral arm and interarm environments described in this work can be used to test theories of cloud formation, evolution and destruction. The distribution of small clouds and the differences between the size spectra of the arm and interarm regions may be of use in deciding whether a 'top-down' or 'bottom-up' model is more appropriate for cloud formation.

As with most observational work, the sample set needs to be extended to obtain a more significant number of clouds. More importantly, different lines of sight must be observed to obtain a better understanding of the average distribution of small clouds in the outer Galaxy. It is very unlikely that the region surveyed in this work is representative of the entire outer Galaxy. In particular, I would like to observe/see observed a few regions in the 3rd and 4th quadrants, so that the star forming properties of these small clouds can be determined from corresponding infrared observations. In addition, the extent of the 13 kpc arm should be traced in molecular material.

7.2.2 Further Investigations of the Physical Properties of Individual Clouds

The kinetic temperatures in this work were calculated using very crude approximations. With more information about the internal structure of the clouds, better estimates of the kinetic temperatures can be made. This information is provided by additional molecular tracers, namely the ^{12}CO $(J = 2 \rightarrow 1)$, ^{13}CO $(J = 1 \rightarrow 0)$, CS $(J = 3 \rightarrow 2)$ and CS $(J = 5 \rightarrow 4)$ transitions. Using the line temperatures of these transitions, not only can the kinetic temperature of the cloud be modeled, but also the density variations in the cloud. Both Large Velocity Gradient and microturbulent radiative transfer models can be used, provided that the cloud is sampled at high enough resolution to make the micro-turbulent calculation worthwhile. Observations of a subset of the clouds described in this thesis have been made in the ^{12}CO (J $= 2 \rightarrow 1$), ^{13}CO (J $= 1 \rightarrow 0$), and CS (J $= 3 \rightarrow 2$) transitions. Analysis of these observations is ongoing [Gellert (1995)].

7.2.3 Distribution of Cold Molecular Material in Outer Galaxy

While the results of this thesis strongly suggest that there exists very little cold molecular material in the outer Galaxy, it is still an interesting proposal. Unfortunately, it will be challenging to unambiguously rule out cold molecular material, because it is extremely difficult to observe except in absorption.

To facilitate the investigation of cold molecular material, I propose creating a finder chart of probable positions. These more-likely positions could then be observed to an arbitrarily low noise level, depending on the patience of the observers and telescope time granted. The idea of using a finder chart is not new; Wouterloot's group has successfully used the IRAS point source catalog as a tracer of molecular material throughout the outer Galaxy.

The finder chart for these observations would be a set of reddened stars for which the previously observed atomic and molecular gas along the line of sight cannot account for the observed extinction. These lines of sight would then be the targets of a sensitive set of observations. If enough lines of sight exist and can be observed, then it is possible that the distribution of cold molecular gas can be determined.

LITERATURE CITED

[Barnard (1919)] Barnard, E. E. 1919, ApJ, 49, 1

[Bevington (1969)] Bevington, P. R. 1969, Data Reduction and Error Analysis for the Physical Sciences (New York : Mc-Graw Hill)

[Binney & Tremaine (1987)] Binney, J., & Tremaine, S. 1987, Galactic Dynamics, (Princeton : Princeton University Press)

[Blitz *et al.* (1984)] Blitz, L., Magnani, L., & Mundy, L. 1984, ApJ, 282, L9

[Blitz *et al.* (1980)] Blitz, L., Fich, M., & Stark, A. A. 1980, IAU Symposium 87, ed. B. H. Andrew, (Dordrecht : Reidel), 213

[Blitz (1979)] Blitz, L. 1979, ApJ, 231, L115

[Bloemen *et al.* (1986)] Bloemen, J. B. G. M., Strong, A. W., Blitz, L., Cohen, R. S., Dame, T. M., Grabelsky, D. A., Hermsen, W., Lebrun, F., Mayer-Hasselwander, H. A., & Thaddeus, P. 1986, A&A, 154, 25

[Brand & Wouterloot] Brand, J., & Wouterloot, J. G. A., 1994, A&AS, 103, 503

[Brand & Blitz (1993)] Brand, J., & Blitz, L. 1993, A&A, 275, 67

[Brand & Wouterloot (1988)] Brand, J., & Wouterloot, J. G. A. 1988, A&AS, 75, 117

[Carpenter *et al.* (1993)] Carpenter, J. M., Snell, R. L., Schloerb, P. F. 1993, ApJ, 362, 147

[Casoli *et al.* (1984)] Casoli, F., Combes, F., & Gerin, M. 1984, A&A, 133, 99

[Chiar *et al.* (1994)] Chiar, J. E., Kutner, M. L., Verter, F., & Leous, J. 1994, ApJ, 431, 658

[Cohen *et al.* (1988)] Cohen, R. S., Dame, T. M., Garay, G., Rubio, M., & Montani, J. 1988, ApJ, 331, L95

[Cohen *et al.* (1980)] Cohen, R. S., Cong, H., Dame, T. M., & Thaddeus, P. 1980, ApJ, 239, L53

[Combes (1991)] Combes, F. 1991, ARA&A, 29, 195

[Dame (1993)] Dame, T. M. 1993, in Back to The Galaxy, ed. S. Holt, & F. Verter, (New York : American Institute of Physics), 267

[Dame *et al.* (1986)] Dame, T. M., Elmegreen, B. G., Cohen, R. S., & Thaddeus, P. 1986, ApJ, 305, 892

[Dame (1983)] ame, T. M. 1983, Ph.D. thesis, Columbia University

[de Geus *et al.* (1993)] de Geus, E. J., Vogel, S., Digel, S. W., & Gruendl, R. A. 1993, ApJ, L97

[Dickman (1978)] Dickman, R. L. 1978, ApJS, 37, 407

[Digel *et al.* (1994)] Digel, S., de Geus, E., & Thaddeus, P. 1994, ApJ, 422, 92

[Digel (1991)] Digel, S. 1991, Ph.D. thesis, Harvard University

[Digel *et al.* (1990)] Digel, S., Bally, J., & Thaddeus, P. 1990, ApJ, 357, 29

[Elmegreen (1993a)] Elmegreen, B. 1993, in Protostars and Planets III, ed. E. H. Levy, & J. I. Lunine, (Tucson : University of Arizona Press), 97

[Elmegreen (1993b)] Elmegreen, B. 1993, ApJ, 411, 170

[Fasano & Vio (1988)] Fasano, G., & Vio, R., Newsletter of Working Group for Modern Astronomical Methodology, ed. F. Murtagh, & A. Heck, 7, 2

[Fich *et al.* (1989)] Fich, M., Blitz, L., & Stark, A. A. 1989, ApJ, 342, 272

[Gellert (1995)] Gellert, F. 1995, Master's thesis, Rensselaer Polytechnic Institute

[Goldreich & Kwan (1974)] Goldreich, P., & Kwan, J. 1974, ApJ, 189, 441

[Grabelsky *et al.* (1987)] Grabelsky, D. A., Cohen, R. S., Bronfman, L., Thaddeus, P., & May, J. 1987 ApJ, 315, 122

[Henderson *et al.* (1982)] Henderson, A. P., Jackson, P. D., & Kerr, F. J. 1982, ApJ, 263, 116

[Jura (1987)] Jura, M. 1987 in Interstellar Processes, ed. D. J. Hollenbach, & H. A. Thronson, (Dordrecht : Reidel), 3

[Kutner (1987)] Kutner, M. L. 1987, Astronomy: A Physical Perspective, John Wiley & Sons, New York

[Kutner & Leung (1985)] Kutner, M. L., & Leung, C. M. 1985, ApJ, 291, 188

[Kutner & Mead (1981a)] Kutner, M. L., & Mead, K. N. 1981, ApJ, 249, L15

[Kutner & Mead (1981b)] Kutner, M. L., & Mead, K. N. 1981, in The Milky Way Galaxy, ed. H. van Woerden, W. B. Burton, & K. J. Allen, (Dordrecht : Reidel), 209

[Kutner & Ulich (1981)] Kutner, M. L., & Ulich B. L. 1981, ApJ, 250, 341

[Kwan & Valdes (1987)] Kwan, J., & Valdes, F. 1987, ApJ, 315, 92

[Lang (1986)] Lang, K. R. 1986, Astrophysical Formulae, Springer-Verlag, Berlin

[Larson (1981)] Larson, R. B. 1981, MNRAS, 194, 809

[Lebrun *et al.* (1983)] Lebrun, F., Bennett, K., Bignami, G. F., Bloemen, J. B. G. M., Buccheri, R., Caraveo, P. A., Gottwald, M., Hermsen, W., Kanbach, G., Mayer-Hasselwander, H. A., Montmerle, T., Paul, J. A., Sacco, B., Strong, A. W., Wills, R. D., Dame, T., Cohen, R. S., & Thaddeus, P. 1983, ApJ, 274, 231

[Lequeux (1995)] Lequeux, J. private communication

[Lequeux *et al.* (1993)] Lequeux, J., Allen, R. J., & Guilloteau, S. 1993, A&A, 280, L23

[Leisawitz (1990)] Leisawitz, D. 1990, ApJ, 359, 319

[Leisawitz (1985)] Leisawitz, D. 1985, Technical Report 85-2, Millimeter Wave Observatory, University of Texas at Austin

[Leung (1985)] Leung, C. M. 1985, in Protostars and Planets II, ed. D. C. Black, & M. S. Matthews, (Tucson : University of Arizona), 104

[Leung (1975)] Leung, C. M. 1975, Ph. D. Thesis, University of California, Berkeley

[Leung & Thaddeus (1992)] Leung, H. O., & Thaddeus, P. 1992, ApJS, 81, 267

[Liszt *et al.* (1981)] Liszt, H. S., Xiang, D., & Burton, W. B. 1981, ApJ, 249, 532

[Lynds (1962)] Lynds, B. T. 1962, ApJS, 7, 1

[Maloney (1990)] Maloney, P. 1990, ApJ, 348, L9

[May *et al.* (1988)] May, J., Murphy, D. C., & Thaddeus, P., 1988, A&AS, 73, 51

[Mead *et al.* (1990)] Mead, K. N., Kutner, M. L., & Evans, N. J. 1990, ApJ, 354, 492

[Mead (1988)] Mead, K. N. 1988, ApJS, 67, 149

[Mead & Kutner (1988)] Mead, K. N., & Kutner, M. L. 1988, ApJ, 330, 399

[Mead *et al.* (1987)] Mead, K. N., Kutner, M. L., Evans, N. J. II, Harvey, P. M., & Wilking, B. A., 1987, ApJ, 312, 321

[Mead (1986)] Mead, K. N. 1986, PhD Thesis, Rensselaer Polytechnic Institute

[Mizuno (1995)] Mizuno, D. 1995, PhD Thesis, Rensselaer Polytechnic Institute

[Mizuno (1994)] Mizuno, D. 1994, REDUCE data reduction package

[NRAO 12m User's Manual (1990)] NRAO staff 1990, NRAO User's Manual

[Peters & Bash (1987)] Peters, W. L., & Bash, F. N. 1987, ApJ, 317, 646

[Press *et al.* (1988)] Press, W. H., Flannery, B. P., Teukolsky, S. A., & Vetterling, W. T. 1988, Numerical Recipes, (Cambridge : Cambridge University Press)

[Rubio *et al.* (1991)] Rubio, M., Garay, G., Montani, J., & Thaddeus, P. 1991 ApJ, 368, 173

[Ryden & Stark (1986)] Ryden, B. S., & Stark, A. A. 1986, ApJ, 308, 823

[Sanders *et al.* (1986)] Sanders, D. B., Clemens, D. P., Scoville, N. Z., & Solomon, P. M. 1985, ApJS, 60, 1

[Sanders *et al.* (1985)] Sanders, D. B., Scoville, N. Z., & Solomon, P. M. 1985, ApJ, 289, 373

[Scalo (1985)] Scalo, J. M. 1985, in Protostars and Planets II, ed. D. C. Black, & M. S. Matthews, (Tucson : University of Arizona), 201

[Scoville *et al.* (1987)] Scoville, N. Z., Yun, M.-S., Clemens, D. P., Sanders, D. B., & Waller, W. H. 1987, ApJ, 63, 821

[Scoville & Sanders (1987)] Scoville, N. Z., & Sanders, D. B. 1987, in Interstellar Processes, ed. D. J. Hollenbach, & H. A. Thronson, (Dordrecht : Reidel), 21

[Solomon *et al.* (1979)] Solomon, P. M., Sanders, D. B., & Scoville, N. Z. 1979, IAU Symposium 84, ed. W. B. Burton, (Dordrecht : Reidel), 35

[Solomon *et al.* (1987)] Solomon, P. M., Rivolo, A. R., Barrett, J., & Yahil, A. 1987, ApJ, 319, 730

[Solomon *et al.* (1985)] Solomon, P. M., Sanders, D. B., & Rivolo, A. R. 1985, ApJ, L19

[Solomon & Sanders (1985)] Solomon, P. M., & Sanders, D. B. 1985, in Protostars and Planets II, ed. D. C. Black, & M. S. Matthews, (Tucson : University of Arizona), 59

[Solomon *et al.* (1983)] Solomon, P. M., Stark, A. A., & Sanders, D. B. 1983, ApJ, L29

[Terebey *et al.* (1986)] Terebey, S., Fich, M., Blitz., L., & Henkel, C. 1986, ApJ, 308, 357 [van Dishoeck & Black (1988)] van Dishoeck, E. F., & Black, J. H. 1988 ApJ, 334, 771

[Vogel *et al.* (1990)] Vogel, S., Kulkarni, S. R., & Scoville, N. Z. 1990, Nature, 334, 402

[Vio *et al.* (1994)] Vio, R., Fasano, G., Lazzarin, M., & Lessi, O. 1994 A&A, 289, 640

[Weaver & Williams (1973)] Weaver, H., & Williams, D. R. W. 1973, A&AS, 8, 1

[Williams *et al.* (1994)] Williams, J. P., de Geus, E. J., & Blitz, L. 1994, ApJ, 428, 693

[Wilson *et al.* (1970)] Wilson, R. W., Jefferts, K. B., & Penzias, A. A. 1970, ApJ, 161, L43

[Wouterloot *et al.* (1993)] Wouterloot, J. G. A., Brand, J., Fiegle, K. 1993, A&A, 98, 589

[Wouterloot *et al.* (1990)] Wouterloot, J. G. A., Brand, J., Burton, W. B., & Kwee K. K. 1990, A&A, 230, 21

[Wouterloot & Brand (1989)] Wouterloot, J. G. A., & Brand, J. 1989, A&AS, 80, 149